The structure of monodisperse foam

A thesis submitted for the degree of
Doctor of Philosophy
2012
Aaron J. Meagher

Declaration

I declare that this thesis has not been submitted as an exercise for a degree at this or any other university and it is entirely my own work.

I agree to deposit this thesis in the University's open access institutional repository or allow the library to do so on my behalf, subject to Irish Copyright Legislation and Trinity College Library conditions of use and acknowledgement.

Signed:
Aaron Meagher

Acknowledgements

I met my significant other due to foam. As I sat for dinner with strangers one day, the conversation turned to occupation. Soon lawyers and dentists and economists raised their heads, and as the waves of acceptable professions rose to the tsunami height of "Doctor, well cardiologist...", I trundled out my little offering and sat on the beach expectantly - there was no time to run.

"*I am a foam physicist.*"

Apparently, it was a growth industry. Apparently, it was receiving huge investment. Apparently, I was safe. The wave rolled on, as did the conversation with the delightful French scholar which, happily, evolved into coffee, then cinema and eventually back to dinner again a few weeks later. "So what exactly do you do, day to day?". "Well" I said, "Basically, I make a foam and I look at it using a microscope". "Oh. Do you then ring them?""

Never has such a simple statement made me go cold as I realised, for the first time, the similarities of the word "foams" and "phones". Love, however, sustained.

I realise that 'sustained love' for physics is exactly what the study of foam has yielded onto me - has rekindled within me. Today, the continuous erosion of progress reports and funding applications and public outreach initiatives and publication goals has placed the emphasis more on what things can can 'do', rather than what things 'are'. Why study foam? Because they are here,

because they are beautiful, because we do not understand them completely yet.

Firstly, I would like to than my supervisor, Prof. Stefan Hutzler for his advice, guidance and direction through the last 4 years. I would particularly like to thank him for taking me on all those years ago. I would also like to thank Prof. Denis Weaire for his incredible insights, and particularly for his organisation of the scientific retreats to his cottage - physics and fishing are a perfect combination. Thanks, also to Dr. Matthias Möbius for his technical advice over the years - we will overlook his introduction of IDL into the group!

One of the great joys of my PhD has been working with so many interesting and diverse people - Mohammed and Joe (Mo-Joe), Roman and Lina, Daniel, Stephen and Steven, Michael Brendan (good morning) Sexton, Cathal, Rob, Ruggero, Ho-Kei, Tuomo, David and Gavin. I would also like to thank my international colleagues, particularly Dr. Francisco Garcia-Moreno, Dr. Manas Mukherjee and Prof. John Banhart of the metallics foam group in TU, Berlin - thank you for all your help and direction over the years, and also for making me feel so welcome during my visits. Thanks to Dr. Adil Mughal for our many thoughtful discussions, his humor and his friendship. My students over the years have also been a joy to work with, demonstrating the very best that the Irish, the French and the Americans have to offer.

I would also like to thank the group of Prof. Martin Hegner, in particular Jason Jensen and Michael Walther for their expertise in 3D fabrication and the use of their 3D printer. In addition, the members of the mechanical workshop, David, Patrick and David, for their help and advice in the manufacture of various components over the years. I would also like to thank John Kelly for his humor over the years - you could always make me laugh.

I want to thank to my Mam and Dad, Claire and David, who encouraged my early desires to become a scientist - I love you both very much. And

my little sister Aoife, who will be the greatest of us all. Also, my brother Eoin and his new wife Sinead who helped me relax at the most stressful time of my PhD. Also, hello to Jason Issacs, Mark Kermode, Simon Mayo, Dick Valentine and Paul Bettany!

Finally, and most importantly, thank you Sarah for all you help, your love and for your ability to overlook my lackluster telecommunications career. We will have Oscar one day. I love you.

Abstract

Equal-sized bubbles of average diameter less than one millimetre are found to spontaneously crystallise upon formation. While previously employed by Sir Laurence Bragg as an ideal system with which to study crystalline systems, this work has been so far limited to two-dimensions due to the problems associated with imaging foams in three-dimensions. Here we demonstrate that advances in μCT X-ray tomography have now produced a technique which will allow for the successful three-dimensional imaging of these foams.

Using this technique, we investigated the structure of monodisperse microfoams of different system sizes. The crystal nature of the samples was determined through a visual inspection of the stacking of the individual bubbles, the calculation of the coordination number and radial distribution function (RDF) of the bubble center positions. It was found that small samples ($\approx$5000 bubbles), spontaneously order into fcc crystals. Larger samples ($\approx$ 20,000 bubbles), which form foams approximately 20 layers deep, are seen to have a different internal structure . Near the boundaries of such sample, hexagonal ordering is still observed. Within the foam bulk, however, the coordination number and RDF indicate that no crystalline order is present. Instead, the wide distribution of the coordination number and the split second peak of the RDF indicate that the sample has formed a Bernal packing - a disordered packing of spheres.

We also investigate the temporal evolution of a sample composed of approximately 15,000 bubbles which was imaged every day over seven days.

The sample was stabilised against coarsening such that the sample remained monodisperse throughout its lifetime. During the experiment, the internal structure of the sample was seen to evolve from a disordered state on the first day of the experiment, to a more ordered state on the seventh day of the experiment. We characterised the order of this sample through the use of the coordination number and RDF function as well as the the bond orientational order parameter (BOOP) and the Voronoi tessellation. The Voronoi tessellation was also used to calculate the local packing fraction ϕ of the sample. It was found that as the sample ordered, no corresponding change in the packing fraction ϕ occurred. Packing fraction is therefore not a useful metric of order within these foam samples.

Following this characterisation of the morphology of these monodisperse foam samples, we investigated several methods by which their structure may be controlled and directed. Firstly, through the use of a cubic container the internal surface of which was templated with the geometry of the Weaire-Phelan (WP) structure, several experimental examples of the WP structure were produced. Following this, we developed a method by which foam structure may be directed through the use of planar boundary conditions. In this endeavour, we developed several pyramids the faces of which were parallel to the closed-packed directions of the simple cubic (sc), body centred cubic (bcc) and face centred cubic (fcc) crystals. Using this method, we successfully generated perfect fcc crystals of bubble diameter between 0.5 and 4.7 *mm*. Bcc foams could be produced successfully for bubbles between 1 and 5 *mm*. We also examined the formation of the unstable sc lattice. To demonstrate the flexibility of this method, we produced a coherent grain boundary between two regions of distinct fcc crystallisation, as well as several examples of a sheared fcc lattice. Finally, the ordering of bubbles within cylindrical confinements was also studied. The resulting structures were compared to simulations focusing on the optimum packing of hard spheres within similar confinement. It was found that the morphology of the cylindrical foam

structures closely resembled their hard-sphere counterparts. Packing fraction measurements of our foam samples were seen to correspond well to computational results of hard spheres.

List of publications

1. A. J. Meagher, M. Mukherjee, D. Weaire, S. Hutzler, J. Banhart, and F. Garcia-Moreno. Analysis of the internal structure of monodisperse liquid foams by x-ray tomography. *Soft Matter*, 7:9881–9885, 2011.

2. A. J. Meagher, D. McAteer, S. Hutzler, and D. Weaire. Building the pyramids: perfect bubble crystals. Submitted to *Soft Matter*.

3. R. Gabbrielli, A. J. Meagher, D Weaire, K. A. Brakke, and S Hutzler. An experimental realization of the Weaire–Phelan structure in monodisperse liquid foam. *Philosophical Magazine Letters*, 92(1):1–6, 2012.

4. S. T. Tobin, A. J. Meagher, B. Bulfin, M. Moöbius, and S. Hutzler. A public study of the lifetime distribution of soap films. *American Journal of Physics*, 79:819, 2011

5. S. T. Tobin, J. D. Barry, A. J. Meagher, B. Bulfin, C. E. O'Rathaille, and S. Hutzler. Ordered polyhedral foams in tubes with circular, triangular and square cross-section. *Colloids and Surfaces A: Physicochemical and Engineering Aspects*, 382(1-3):24–31, 2011. A collection of papers from the 8th EUFOAM Conference and the Meetings of COST Actions D43 and P21

6. P. Stevenson. *Foam Engineering: Fundamentals and Applications.* John Wiley and Sons, 2012 - listed contributing author

7. D. Fernóndez, M. Martine, A. J. Meagher, M. E. Möbius, and J.M.D. Coey. Stabilizing effect of a magnetic field on a gas bubble produced at a microelectrode. *Electrochemistry Communications*, 18(0):28 – 32, 2012

Contents

List of Figures

Chapter 1

Introduction

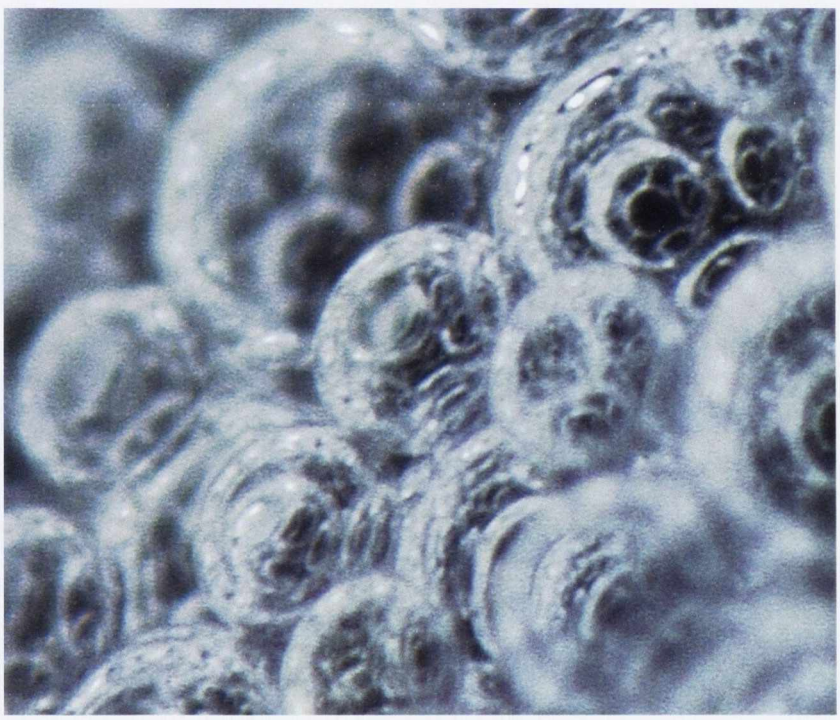

Figure 1.1: A photograph demonstrating the beauty and complexity inherent within foams.

An *aqueous foam* (see Fig.1.1) may be defined as a a two phase system composed of a continuous liquid phase and a dispersed gas phase [1]. However, there also exist foams in which the continuous phase is a solid, such as for a metallic foam, or a biofoam in which the continuous phase is ceramic in nature[2, 3]. A dispersion of liquid within a continuous liquid phase, known as an *emulsion*, may also be considered. All these exhibit many similar characteristics associated with foams [4].

1.1 Some foam characteristics

Figure 1.2: An image of a single bubble floating in free space. Minimisation of surface area results in a spherical shape.

A single isolated bubble will take on a familiar spherical shape (see Fig.1.2) as a result of foam's tendency to minimise its total energy, resulting in a shape of minimum surface area [1]. Bringing many bubbles together produces a bubble cluster. If the number of bubbles is increased again, a foam is

formed. The structure of a foam is far more complex that that of the humble isolated bubble. While many factors determine foam morphology, there exist three main qualities, in the form of the *dispersity*, the *liquid fraction* and the *average bubble size*, which broadly determine foam structure.

The dispersity of a sample is the ratio of the standard-deviation to the mean of the bubble diameter distribution. A sample whose dispersity is less than 5 % is generally described as *monodisperse* whilst a sample whose dispersity is larger than 5 % is described as *polydisperse* [5].

Once produced, it is found that a foam evolves in time. This is a result of the internal pressure associated with each bubble. The pressure difference between the interior and the exterior of a bubble is given as

$$\Delta P = \frac{4\gamma}{r} \tag{1.1}$$

where γ is the surface tension of the liquid phase and r is the bubble diameter [1]. This equation implies that smaller bubbles have a higher internal pressure than larger bubbles. The resulting gradient in pressure between small and large bubbles causes a diffusion of gas, through the films and liquid phase of the foam, from small bubbles to large bubbles. This *coarsening* of a foam leads to the dispersity of the foam increasing with time, as well an increase in the average bubble diameter as $r \propto t^{1/2}$ [6].

The liquid fraction ϕ_l of a foam is the ratio of the volume of the continuous liquid phase of the foam V_l to the total foam volume V_f[1]. Liquid fraction may be used as method of broadly classifying foams into two groups: for low liquid fractions, with $\phi_l \leq 0.2$ a foam is described as being *dry* while, conversely, for $\phi_l \geq 0.2$ a foam is described as being *wet* [1]. The liquid fraction may be expressed in terms of the fraction of the disperse gas phase ϕ_g of the foam as $\phi_l = 1 - \phi_a$. If we consider a foam as a granular packing of bubbles, ϕ_g is equivalent to the packing fraction ϕ of granular media.

For many purposes, controlling the liquid fraction of a foam is a desirable, but difficult, process. The difficulty arises from the tendenacy of most foams

to dry out due to gravitational drainage [7]. This may be counteracted, resulting in a stable wet foam, in several ways. Most simply, a continuous supply of liquid may be added to the topmost section of the foam, replacing the liquid lost through drainage. This process, known as *forced drainage*, will result in a wet foam, however the throughflow of liquid is not suitable for many static experiments. A static wet foam may be produced in microgravity, where gravitational drainage is essentially turned off. Such microgravity experiments are generally conducted using a drop-tower, sounding-rocket or during parabolic flights. This results in microgravity experiments being both expensive and time-limited due to the short intervals of microgravity produced in these experiments [8, 9].

The alternative to the above methods is through exploitation of the capillary effect associated with liquids. The capillary effect, which draws liquid along objects placed into the surface of a liquid, will also result in liquid rising into a foam in contact with a liquid surface. This counteracts gravitational drainage, resulting in a section of wet foam adjacent to the foam-liquid interface. It may be shown that the height of this wet section H_w is given by

$$H_w = \frac{l_0^2}{d} \tag{1.2}$$

where l_0 is the capillary length of the liquid phase and d is the average bubble diameter [1]. $l_0 = \sqrt{\frac{\gamma}{\rho g}}$ where γ is the surface tension of the liquid phase of the foam, ρ is the liquid density and g is acceleration due to gravity. For typical surfactant solution, $l_0 \approx 1.6mm$. For bubbles of 1 cm in diameter, the wet region is 0.0001 m in height above the foam-liquid interface, thus extending less than one layer into the foam structure. However, if the average bubble diameter is significantly reduced, say into the regime of 100 μm, the corresponding wet region extends 1 cm into the foam, resulting in several wet foam layers. This effect can be used to produce a static, stable wet foam suitable for experimental investigation.

We may now investigate the structure of foam in the two extremes of

liquid fraction. We will also investigate how this structure depends on the dispersity of the sample.

1.1.1 Dry foam

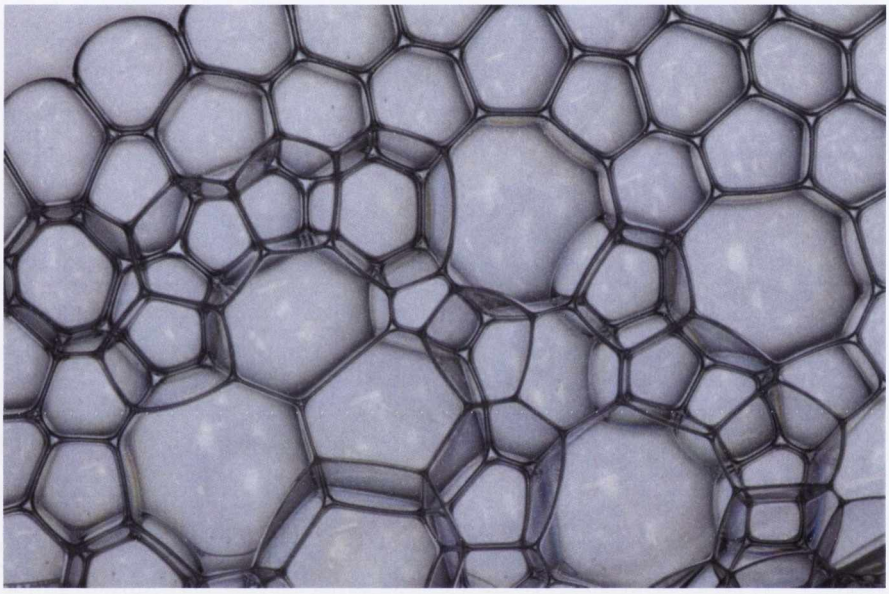

Figure 1.3: A dry foam demonstrating the various rules of Plateau.

A dry foam is composed of a series of interconnected polyhedral cells (as seen in Fig.1.3), the underlying geometry of which is dictated by Plateau's rules [10]. Joseph Plateau, a 19th Century Belgian physicist, conducted the first experimental study of dry aqueous foams, leading to four empirical rules regarding their local structure [1]. These rules are :

1. Foams are composed of smooth interfaces.
2. Each soap film has constant mean curvature across its surface.
3. Three soap films meet at $\frac{2\pi}{3} = 120°$ to form a *Plateau border*.

4. Four Plateau borders meet at $\cos^{-1}(-1/3) \approx 109^\circ$ to form a *vertex*.

These rules are a result of foam's tendency to minimise surface area [1]. While Plateau's rules accurately describe the local geometry of a dry foam, the foam's global properties may not be deduced from them. The analysis of these global properties was first performed by Matzke, a biologist, in 1939 when he determined the distribution of the number of faces and edges of a dry monodisperse foam composed of 5000 bubbles [11]. This analysis showed a wide distribution of edges and faces for the foam, indicating that a bulk dry foam is disordered in nature, with the average number of faces $\langle f \rangle \approx 14$. This random nature of dry monodisperse foam was concisely demonstrated by Kraynik *et. al.* who recovered the same distribution of edges and faces in computer simulations of monodisperse foams [12]. To produce the foam structure, a disordered packing of spheres was first generated. The Voronoi tessellation of this packing was then calculated, and used to produce a realistic foam structure through its energy minimisation using Surface Evolver.

While this random structure of foams is seen to dominate in experiment, the question may be asked what is the most efficient foam structure? The most efficient dry monodisperse foam structure is the one which partitions space into equal-units while minimising its surface area. In two dimensions, it is found that such a condition is fulfilled by the honeycomb lattice [1]. In three dimensions, however, this is a non-trivial question, first addressed by Lord Kelvin in 1887 in his pursuit of the ideal structure of the ether - the medium which was believed to permeate all space. Now known as the *Kelvin conjecture*, he stated that the ideal structure was that of the *truncated octahedron* (see Fig.1.4) which fulfilled this minimum partition problem of space [13].

In 1993, however, Weaire *et al.* discovered a new structure - the Weaire-Phelan (WP) structure - which was found to be a more efficient partition of space by 0.18% when compared with the Kelvin structure [14]. The WP structure is based on the energy-minimised Voronoi tesselation of the A15

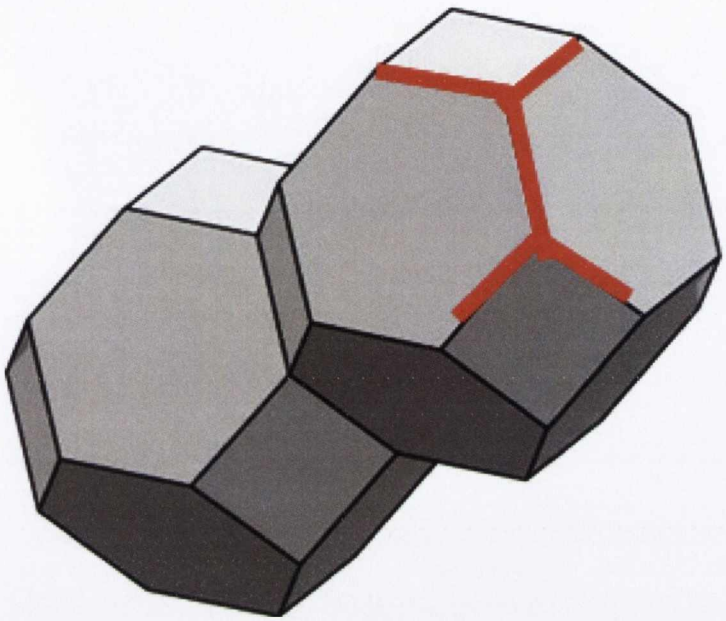

Figure 1.4: A simulation of two Kelvin cells produced using Surface Evolver. The Kelvin cells are a space-filling polyhedron based upon a bcc lattice [6].

crystal structure constrained such that each cell of the resulting structure has the same volume (see Fig.1.5).The resulting structure is composed of two distinct types of polyhedra - one is the irregular dodecahedron composed of pentagonal faces while the second is a regular tetrakaidecahedron composed of two hexagonal and twelve pentagonal faces. The unit cell of the WP structures is composed of an arrangement of 2 dodecahedrons and 6 tetrakaidecahedra.

From its discovery in 1993, however, an unresolved question has troubled the WP solution to the Kelvin problem. After the theoretical discovery of the WP structure, several examples of Kelvin cells within monodisperse foams were found [16, 5]. In these experiments, monodisperse bubbles of average diameter approximately 1 mm were introduced into a Hele-Shaw cell. As the bubbles filled up the cell, the liquid fraction of the top most layer of bubbles

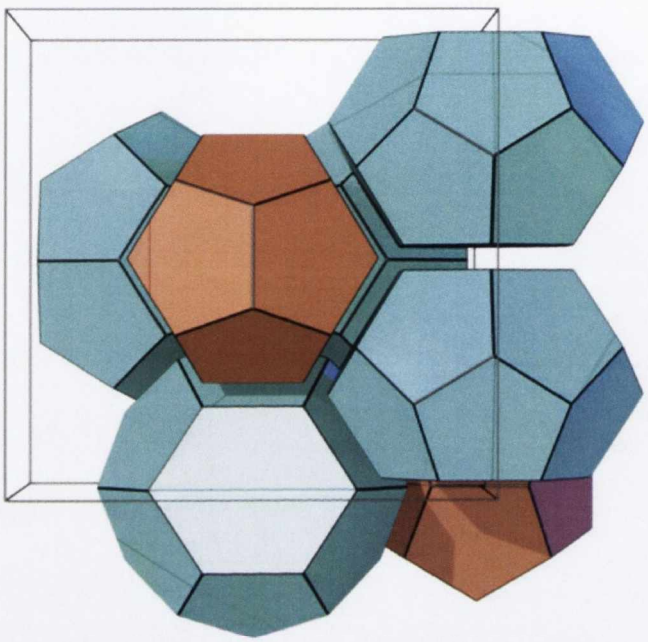

Figure 1.5: A simulation image of the WP structure. The tetrakaidecahedra are shown in blue while the dodecahedrons are shown in brown. Image reproduced with permission from Ruggero Gabrelli using 3dt [15].

was reduced by gravitational drainage. Once the foam had become dry, the resulting configuration of bubbles was identified as a series of Kelvin cells by visual inspection. During all such experiments, however, no example of the WP structure was found.

It was believed that experimental verification of WP structure might not be possible due to the small difference in surface energy of the two structures and the complexity of the WP structure. In Chapter 4 we will examine a method by which the WP structure may be formed in experiment.

1.1.2 The structure of wet foam

As the liquid fraction of a dry foam is increased, through one of the various methods described in section 1.1, the foam structure begins to change. The vertices and Plateau borders of the foam swell, diminishing the angular nature of the original dry foam. Eventually, for high liquid fractions, the foam may be considered as a packing of spheres rather than a partition of space, as demonstrated in Fig. 1.6 for two-dimensional foams. As the liquid fraction of the foam is increased, the question of the foam's ideal structure changes from one concerned with the minimum partitioning of space to a related question; which is the ideal packing of spheres?

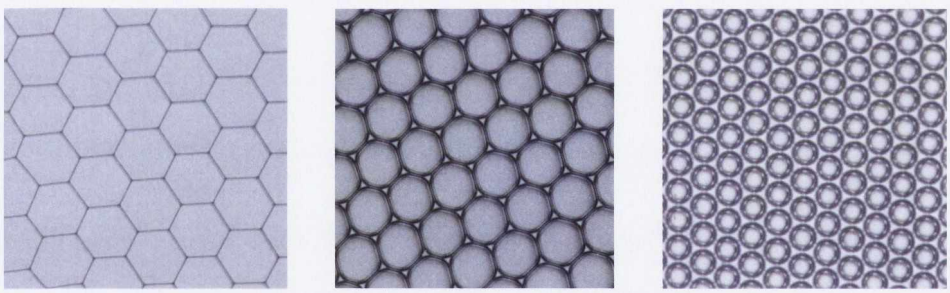

Figure 1.6: Experimental packing of bubbles into the honeycomb configuration for the case of a dry foam, an intermediate foam and the wet case (the dry foam is confined between two glass plates, while the intermediate and wet cases are free-floating Bragg rafts). Note that in the wet (c) case the bubble appear separated due to an optical effect.

In two dimensions, the same efficient hexagonal partitioning of space produces the most efficient packing of discs (as seen in Fig.1.6). In three dimensions, however, this simple relationship between the two problems is no longer valid. Both the A15 lattice and the BCC structure which form the basis of the WP and Kelvin structure for dry foams are found to be unstable for wet

foams [7, 17, 18]. Instead, it is the well-known fcc structure, first envisaged by Kepler in his pursuit of the structure of snowflakes, which is the most efficient packing in three-dimensions, although such a statement has only recently been proven [19, 20].

While ordered foams are difficult to produce in dry foam, it is found that wet monodisperse foams spontaneously order into their minimum energy configuration of the fcc lattice. Such spontaneous ordering is shown in Fig.1.8 in which a photograph shows the surface ordering of a monodisperse foam sample of average diameter 800 μm. The regular hexagonal arrangement of the topmost layer of this foam indicates the ordered nature of the underlying foam. The crystalline nature of these systems was first studied by Bragg and Nye in 1947 [21]. They found that a two dimensional raft of monodisperse microbubbles formed an ideal model system with which to study crystalline structure [22, 23]. This was due to the ability to form grain boundaries, interstices and vacancies through the removal and addition of bubbles, and control of the boundary conditions of the sample [24]. In addition, it has been found that the inter-bubble potential in such a 2D raft closely resembles the Lennard-Jones potential[25]. In fact, for bubbles of the right diameter, the resulting potential may be scaled with bubble diameter accurately to the inter-atomic potential of copper atoms [23]. Indeed, the accuracy and efficiency of this bubble model for the study of crystalline structure has continued to the present day, with the Bragg bubble raft forming the basis for many experiments investigating the nanoindentation process [26, 27].

Although primarily interested in the two dimensional ordering of such samples, Bragg *et al.* demonstrated that when three dimensional samples of monodisperse microbubbles were formed, surface details indicated the presence of crystalline ordering [21]. Within such samples, they also found surface evidence for the formation of grain boundaries (see Fig.1.7). More recently, van der Net *et. al.* investigated the ordering nature of these three-

Figure 1.7: Photograph of the top layer of a 3D monodispese aqueous foam of average bubble diameter 400 μm . The bubbles are seen to spontaneously form distinct crystal domains which are separated by disordered grain boundaries.

dimensional bubble crystals using *ray tracing* techniques [28]. By comparing computer simulations of crystalline arrangements of glass spheres with experimental photographs of monodisperse microfoams, the ordering nature of the surface of such bubble crystals may be determined (see Fig.1.8). They found that regions of fcc and hcp ordering existed at the surface of these samples. They also found evidence for interstices, vacancies and grain boundaries directly underneath the surface layers of these three-dimensional foams (see Fig.1.7) [29]. Optical limitations, however, prohibited the study of these foams beyond the first three foam-layers adjacent to the sample surface.

The spontaneous crystallisation of these foam systems has produced particular interest due to the lack of such analogous behaviour in similar systems

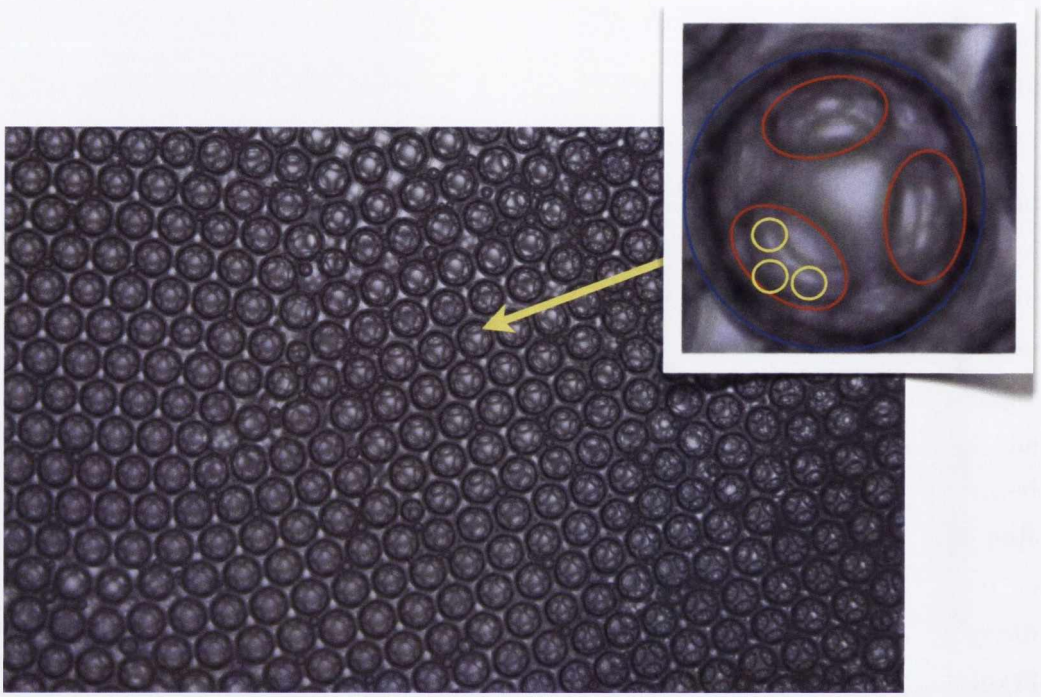

Figure 1.8: Photograph of the surface of a monodisperse microfoam (average diameter 800 μm). The fcc $\langle 111 \rangle$ nature of the crystallisation can be determined through examination of the refracted image of the second (red) and third (yellow) layers in the first (blue) layer of the foam.

of spherical particles. For example, in D.G. Scott's first investigation of large packing of hard spheres [30] in 1960, it was found that the packing fraction ϕ - the total volume of spheres divided by the total volume of the system - of large quantities of spheres did not exceed 0.64, far below the packing fraction of 0.74 associated with hexagonally closed-packed structures [13]. Such a random packing state is known as a *random packing* or *maximally random jammed* (MRJ) state [31].

The internal structure of these random packings of spheres was first studied by the Irish physicist Bernal in his investigation of liquids [32]. He showed

that in disordered packings of spheres, in which no long-range order is observed, there still exists local, short-range translational order [33]. Due to his influence on the study of these disordered packings, such packings are now referred to as *Bernal packings*.

In spite of the many applications of these monodisperse microfoams, full three-dimensional study of monodisperse foam crystals has been somewhat limited. This has been due to the problems associated with an optical characterisation of the ordering behaviour of these foam samples due to the multiple scatterings of light which occur within these samples. Such scattering, which produces the characteristic white hue of foams, also limits detailed optical analysis of their internal structure. In 1992 Durian *et al.*, however, developed a method of using these multiple scatterings of light to determine the average bubble diameter of wet foams by modeling this light propagation by scattering as a diffusion process [34]. However, this methodology is limited to samples of small average bubble diameter ($\approx 100\ \mu m$) and provides no information about internal foam structure.

Full three dimensional characterisation of these foam structures requires advanced imaging techniques. Using MRI technology, Gonatas *et al.* successfully studied the coarsening dynamics of a three dimensional foam [35]. However, due to limited computational power at the time of the experiment, bubble radii were determined from the apparent radii seen on two-dimensional sections taken through the foam sample. This results in a systematic shift in the bubble size distribution. In addition, the relative high cost of MRI machines ($\approx$ \$1 million) excludes these machines from standard foam laboratories.

A more low-cost alternative to this imaging technique is offered by optical tomography, which has been successfully used to image a dry foam [36]. Due to the relative simplicity of the experimental components required (optical camera, rotation stage, planar backlight), optical tomography is a quick and cost-effective method of characterising the three-dimensional qualities of a

foam. However, as with most optical techniques, three-dimensional characterisation is limited to dry foams of a thickness such that all parts of the foam are at one-time visible. The possibility of observing truly "bulk" qualities of a foam is therefore lost.

X-ray tomography has proven to be a useful tool for studying the internal structure of both wet and dry foam. In Chapter 2 we will investigate how X-ray tomography has been applied to aqueous foams, and demonstrate that advances in μCT now provide us with a cheap and convenient method by which the internal structure of wet foams may be investigated. Such analysis will produce fully-resolved three-dimensional positional data of our foams, allowing, to date, the most compete characterisation of these useful foam systems.

1.2 Order parameters

When investigating three dimensional positional data, it is desirable to employ quantifiable measures of structure to distinguish between disordered and ordered systems. There exists several metrics of order which are positively correlated [31]. Each order metric investigates a different aspect of the ordering of the sample. For our purposes, we will use the coordination number, the radial distribution function, the bond orientational order parameter and the Voronoi tessellation to quantify the ordering of our foam samples. These metrics are calculated using the bubble center positions produced using the commercially available software MAVI [37].

1.2.1 Coordination number

The coordination number n is the number of nearest neighbours for a given particle within a packing [31]. It is found that the coordination number may be used as a crude measure of order for granular packings. Experimentally, it has been used to characterise ordering within sphere packings [32]. Hexag-

onally closed packed structures will generally have a coordination number of $n = 12$, excluding boundary cells. For random packings of hard spheres, while locally n may vary significantly, globally n will average to 6, as is given by the isostatic argument [38].

There exists several methods by which the neighbourhood of a particle may be defined, e.g. through the use of the Voronoi tessellation to define a local neighbourhood for each particle within the packing. The average contact number is then defined by the number of faces of the corresponding Voronoi cell. However, such definitions have associated with them complications which make their physical interpretation difficult e.g. a Voronoi tessellation for an fcc lattice produces a coordination number of $n = 14$ when, physically, a sphere within an fcc lattice has $n = 12$.For present purposes, it was found that a simple definition of contact based on the distance between particles was the most efficient to implement, analyse and interpret. We define two particles, i and j, as neighbours if

$$|\vec{r}_i - \vec{r}_j| \leq R_i + R_j \tag{1.3}$$

where $\vec{r}_i$ and $\vec{r}_j$ are the positions of the i^{th} and j^{th} particles within the packing, and R_i and R_j are the corresponding particle radii. The probability distribution $P(n)$ of particles with n neighbours can give valuable information about the local structure of a particular packing. A wide distribution of $P(n)$ indicates disorder within the sample, while sharp maxima indicate the presence of local ordering. However, detailed information about the structure being examined is not provided by this order measure.

1.2.2 Radial distribution function

The Radial Distribution Function (RDF), also known as the pair correlation function, $g(r)$ is a mathematical representation of translational order within a sample [39]. It is a correlation function of particle center positions which

examines the distribution of nearest neighbours within a sample. The RDF may be given as:

$$g(r) = \frac{V}{4\pi r^2 N^2} \sum_{i=0}^{N} \sum_{j \neq i}^{N} \delta(\vec{r_i} - \vec{r_j}) \tag{1.4}$$

where r is the radial distance from a given particle, N is the number of particles and V is the enclosing volume of the particles being examined. For the case of completely periodic systems - such as a perfect crystal lattice - the corresponding RDF function will be composed of a series of δ-peaks. The location of these peaks corresponds to the radial positions of neighbours within the crystalline lattice. For the case of a finite packing, however, care must be taken that the border of the sample does not influence the resulting RDF. So as to avoid this complication, when computed, only those points which are a distance r_{max} from the boundary of the sample are considered. Increasing r_{max} increases the range investigated by the RDF, but reduces the number of experimental points being averaged, resulting in in an increase in data noise. Typically, the radial distances r of the RDF are normalised by the position of the first peak of the radial distribution function r_0. This, generally, corresponds to the diameter of the particles being examined.

Due to the uniqueness of the lattice positions associated with each crystal structure, the RDF acts as a signature by which the exact structure of a crystal lattice may be examined. In this respect, it is related in function to the structure factor $S(\vec{k})$ of X-ray scattering data. In fact, $g(r)$ may be related to spatial Fourier transformation of the structure factor $S(\vec{k})$ [40].

The radial distribution function may also be used to calculate an additional order metric, the *translational order parameter* G, for the packing. This single, scalar number, is a convenient measure which may be used to directly compare differences in translational symmetry between two structures [39]. The translational order parameter G is defined as

$$G = \frac{g(r_{min})}{g(r_{max})} \tag{1.5}$$

where $g(r_{min})$ is the value of the sample's RDF at the first minimum while $g(r_{max})$ is the value at the first maximum (see Fig. 1.9) [39]. As the RDF of a perfectly crystalline sample is composed of a series of discrete delta functions, $g(r_{min}) = 0$, resulting in $G = 0$. As the sample becomes more disordered, the discrete delta functions widen into a continuous distribution of points, resulting in an increase in $g(r_{min})$. This leads to a non-zero value of G for disordered systems, the value of G increasing as the translational disorder of the system increases. The values of $g(r_{min})$ and $g(r_{max})$ are calculated from fourth order polynomial fits to the experimental data.

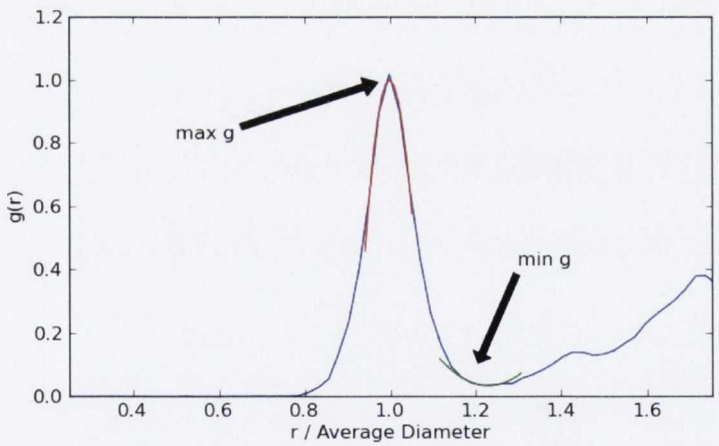

Figure 1.9: Plot showing the first maximum and minimum of the RDF function used to calculate the translational order parameter. The ratio between these two values is used as a metric of translational order G within the sample. 4^{th} order polynomials are fitted to the data to find the accurate values of the maximum and minimum values of the RDF.

1.3 Thesis outline

Using μCT X-ray tomography, which is described in Chapter 2, we will investigate the structure of monodisperse microfoams. In Chapter 3, we will investigate the variation of the ordering of such foams with sample size, as well as with sample age. Following this characterisation, we will investigate methods by which their structure may be controlled. Chapter 4 will look at the use of templates to control these samples, while Chapter 5 will investigate the use of carefully selected planar boundary conditions of the sample. Finally, in Chapter 6, the study of the ordered structures produced when such monodisperse microfoams are confined within cylinders will be described.

Chapter 2

X-ray tomography of liquid foams

2.1 Introduction

X-ray tomography is a non-destructive method of obtaining full, three dimensional data about the structure of an object [41]. First developed by Godfrey N. Hounsfield in the 1970s [42], tomography has had most successful applications in the medical area where *Computer Tomography* or *CT* has been used for the diagnosis of disease and the imaging of complex injuries. In the area of physics, it has had many applications. In particular, over the last twenty years, X-ray tomography has been applied to the area of granular media with much success [43, 44].

Before the development of X-ray tomography, the methods employed in determining statistics from granular media, such as object location, size and neighbourhood distribution was a difficult, and time consuming, process. This is best illustrated in the pioneering work of J.D. Bernal on the random packing of hard spheres which aimed to describe the structure of liquids using a hard sphere model [32]. Although such a description of liquid failed to fulfil the early promise of the work, Bernal successfully pioneered the study

of the structure of hard sphere packings. In particular, Bernal and Finney conducted the first study of the coordination number and radial distributions associated with these packings [33]. To conduct these measurements, up to 4000 spheres were placed into a burlap sack and annealed by hand. Ink was then introduced into the sack, and allowed to dry. Individual ink-coated spheres were then broken from the conglomerate. From the ink pattern on each sphere, the number of nearest neighbours (those neighbours in contact with an individual sphere) and close neighbours (spheres directly beside but not in contact with a particular sphere) could be determined. To calculate the radial distribution function, a packing of 5000 spheres was sintered to produce a solid conglomeration. The resulting conglomeration of spheres was mounted on a free-standing milling machine. Successive 1 *mm* thick sections were removed along the z axis of the structure. The centre position of each sphere, identified as the centre of the disk of maximal area associated with the milling of each sphere, could be measured in three dimensional space through the use of a plum-line attached to an xy grid mounted above the conglomeration. The resulting data set of sphere center positions was then used to calculate the radial distribution function for the packing. Obviously, this was an incredibly time-consuming and hardly reproducible experimental process.

The development of X-ray tomography has allowed this same experiment to be repeated, with greater ease, on a larger scale, to a higher precision. For example, in 2005, Aste *et al.* conducted a tomographic investigation of the packing of 150,000 monodisperse beads of 1 *mm* in diameter [45]. Their increased accuracy allowed them to completely characterise the structure through the use of many order parameters, including the RDF(see section 1.2).

X-ray tomography has also been successfully applied to image the internal structure of aqueous foams of various liquid fractions. Lambert *et al.* have used this high-energy X-ray tomography to examine the coarsening dynamics

associated with three-dimensional foams [46, 47]. Using the high-resolution data provided by these images (resolution $\approx 10\ \mu m$), and advanced segmentation techniques, Lamber *et. al.* were able to determine the average bubble diameter for each bubble within the sample. The evolution of the average bubble radius $\bar{r}$ with time, the coordination number of each bubble, and the characteristics of the growth-rate constant G could be determined.[1]

Stocco *et. al.* used phase-contrast X-ray tomography to study the evolution of particle stabilised foams. Image resolution of 1 μm was available at the BAMline (Bessy, HZB, Germany). This permitted the bubble-size distribution of the foam sample to be accurately measured over time, allowing the coarsening dynamics of such a foam to be investigated which showed that the addition of the silica nanospheres to the liquid phase halted the coarsening of small bubbles (diameter $< 30\ \mu m$).

To date, however, X-ray tomography of aqueous foams has been confined to high energy X-ray facilities e.g. European Synchrotron Radiation Facility (ESRF). These facilities provide the high sensitivity and rapid acquisition rate required to produce usable reconstruction of aqueous foams. However, due to the large expense and limited time available for individual studies at such facilities, the range of experiments that may be conducted is limited.

We believe that we may image monodisperse wet foams, however, using convenient low-energy μCT X-ray tomography. Due to the relatively high X-ray absorption from the thick Plateau borders and vertices of such a wet foam, successful X-ray imaging is possible. Such μCT imaging, however, is a slow process, requiring acquisition times of several hours rather than seconds when using high-energy X-ray tomography. This long acquisition time is therefore not suitable for imaging a typical dry aqueous foam due to its relatively rapid coarsening rate. The coarsening rate of monodispese microbubbles, however, is significantly reduced when compared to these foams. Firstly,

[1] It may be shown that the growth rate of a bubble of volume, V, in a three dimensional foam is of the form $\frac{dV}{dt} = V^{1/3}G$ [48]

due to the low initial dispersity of our samples, the differences in pressures between neighboring bubbles is reduced when compared to a polydisperse foam, resulting in a slower initial coarsening rate. In addition, the high liquid fractions of these monodisperse microfoams result in thick Plateau borders, vertices and soap films. As the coarsening rate of a foam is inversely proportional to the film thickness of the foam, this results in the coarsening rate of our monodisperse microfoam decreasing significantly when compared to a dry foam [6]. The coarsening rate of our monodisperse microfoams may be further reduced through the use of the concept of a *frustrated froth* [49]. Weaire *et. al.* showed that the evolution of a foam composed of two gasses is determined by the gas of the lowest permeability. It was found that the addition of even a small quantity of slow-diffusing gas produces a dramatic reduction in the coarsening rate of the foam, producing foams stable against coarsening for several hours [6].

2.2 Basic X-ray tomography theory

Tomography is based upon Lambert-Beer law; namely there exists a logarithmic relationship between the intensity of light transmitted through an object and the absorption coefficient of the object itself, or, stated concisely

$$A = log\left(\frac{I_d}{I_0}\right) \tag{2.1}$$

where A is the absorption coefficient of the body, I_0 is the initial intensity of the radiation and I_d is the transmitted radiation [50]. This coefficient can be expressed in terms of the *linear attenuation coefficient* μ, a local measure of the absorption characteristics of the body, as $A = \int \mu(x, y)\, \mathrm{d}x\mathrm{d}y$, for absorption in the xy plane of radiation travelling in the z direction. This linear attenuation coefficient is the product of the object density and the mass-absorption coefficient of the material in question. It contains all the

structural information required to obtain a complete three-dimensional reconstruction of the objects in question.

For the purposes of illustrating the principle of tomography, however, we will examine the case of a two-dimensional object O, illuminated by a planar X-ray source, the radiation from which is measured at a planar detector D (see Fig. 2.1).

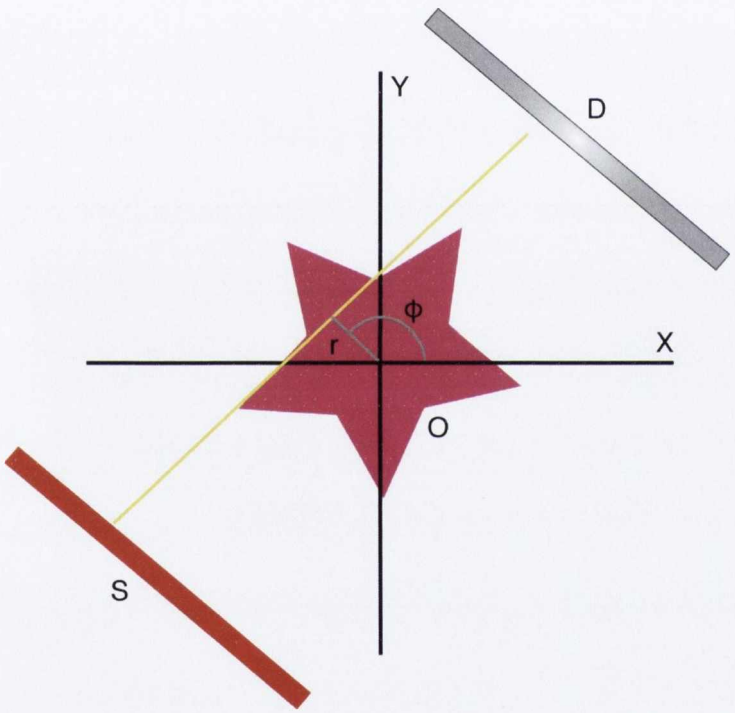

Figure 2.1: Illustration showing the experimental setup used in X-ray tomography experiments, composed of an X-ray source S, the test object O, and the planar detector D. During the experiment the object O is rotated through an angle ϕ and a two-dimensional intensity profile $p(r, \phi)$ is recorded at the detector D.

During tomography the object is rotated around its central axis. For

each rotation angle ϕ, a one-dimensional intensity profile $p(r, \phi)$ dependent on the distance from the centre of the object r is recorded. The Radon transformation states that each of these profiles, $p(r, \phi)$, is simply a one-dimensional projection of the two-dimensional object being imaged:

$$p(r, \phi) = \int \mu(x, y)\delta(xcos\phi + ysin\phi - r)\,\mathrm{d}x\mathrm{d}y. \tag{2.2}$$

The Cental Slice Theorem provides a method by which the form of μ may be calculated when p is known [50]. It states that the 1 dimensional Fourier transformation of the measured profiles is equal to the two-dimensional Fourier transformation of the linear attenuation coefficient:

$$\int p(r, \phi)e^{-2\pi irz}\mathrm{d}r = \int\int \mu(x, y)e^{-2\pi z(xcos\phi + ysin\phi)}\mathrm{d}x\mathrm{d}y, \tag{2.3}$$

Once p has been measured, its Fast Fourrier Transform (FFT) may be calculated, which is then related to the 2D FFT of μ. By then calculating the inverse FFT, the original μ may be calculated.

2.3 Experimental procedure

Our X-ray tomographic experiments were broken down into 4 stages. These stages were:

1. Sample preparation
2. Image acquisition
3. Image reconstruction
4. Image processing

Following the image processing step, the analysis of the experimental data was conducted.

2.3.1 Sample preparation

The foam samples were produced using a *microfluidic flow-focusing* device which allows for the production of monodisperse foams of average bubble size between 100 μm and 1500 μm. The rapid production rate of foam from such a device means that large foam samples (consisting of about 1000 bubbles) can be generated before the sample has coarsened significantly [51]. A flow focuser consists of a closed chamber into which there are two input channels and one outlet channel. Through the inlets is supplied a constant flow of surfactant solution, as well as gas at constant pressure. At the confluence of surfactant and gas supply at the outlet nozzle, it is found that an instability between the two supplies arises. This instability produces a foam of small bubble diameter [52]. For particular combinations of flow rates of surfactant solution, pressure of gas and nozzle size, the foam produced is monodisperse. The size of the resulting bubbles is a function of both flow-rate of the surfactant solution and the output nozzle size. By increasing the surfactant flow rate and decreasing the output nozzle size, the average bubble diameter may be decreased.

For our X-ray tomographic experiments, the surfactant solution used to produce our foams was composed of 5% by volume aqueous solution of the commercially available detergent *Fairy Liquid*. This is found to produce stable foams suitable for a wide variety of experiments. The gas-phase of our foams was composed of a mixture of Oxygen-Free Nitrogen gas and Perfuorohexane (PFH). PFH, with a very low solubility, results in a significant reduction of the coarsening rate of a foam when added to a sample (see section 1.1). This was particularly important during our X-ray tomography experiments as any movement produced by coarsening during image acquisition will result in a blurring of the reconstructed images.

It was found that foams containing PFH exhibit a rapid expansion of the average bubble size when directly exposed to air. This is due to the diffusion of Nitrogen gas into the foam from the atmosphere in an attempt to equalise

the partial pressure gradient produced by the presence of the PFH. This results in a increase in the average bubble size, as well as an increase in the polydispersity of the sample. Even once the sample has been sealed from the atmosphere, the resulting bubble size gradient will continue to increase the coarsening rate of the foam, again causing rearrangements within the sample, and thus image blurring during the tomographic process.

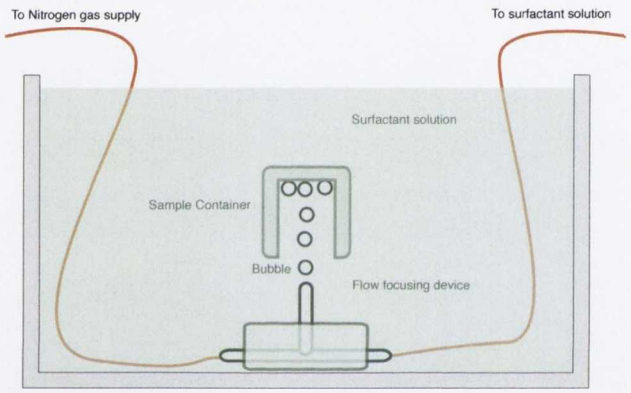

Figure 2.2: Illustration of the surfactant-bath used to generate foams for X-ray tomographic experiments. The flow focusing device, attached to the bottom of the surfactant bath, produces monodisperse bubbles which are then captured in a surfactant-filled sample container. In this way, the bubbles are never exposed to atmosphere, resulting in a stable foam.

To avoid this effect, we fixed our flow-focusing device to the bottom of a surfactant bath, as shown in Fig.2.2. The sample containers were placed into the same bath, rotated and shaken so that all trapped air within the container was released. The flow focusing device was then engaged. Once a stable stream of bubbles, of the desired bubble diameter, was produced the surfactant-filled container was positioned above the opening of the flow-focusing device. This allowed the monodisperse bubbles to be produced and captured without exposing the foam to the atmosphere. Once filled, the container was sealed by sliding a glass plate over the open face of the

container, which was then removed from the solution.

It was found that a slight expansion of the foam with time still occurred. This, we believe, was due to evolution of dissolved nitrogen gas from the solution into the bubbles. To combat this effect, a rest-time of two hours was established between foam production and foam imaging. This was found to produce a foam sufficiently stable for imaging purposes. Following the rest time, each sample was affixed onto a polyurethane mounting stage through the use of a hot glue resin. The stage was then fixed within the X-ray tomographic device.

2.3.2 Image Acquisition

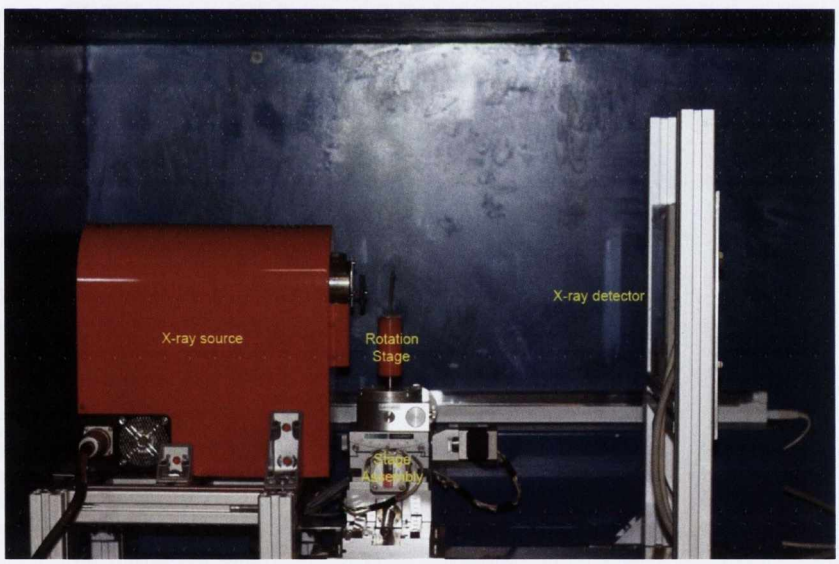

Figure 2.3: A photograph of the X-ray tomographic apparatus used to image our foam samples. Showing X-ray source, rotation stage upon which the samples are mounted, and the X-ray detector. The entire device is enclosed in a blue steel box to contain the X-ray radiation during sample imaging.

X-ray tomography was conducted in the Metallic foams group at the Helmholtz-Zentrum Berlin institute. The X-ray tomographic device that was used is shown in Fig.2.3. The device is composed of three main parts; the X-ray source, the rotation stage and a flat panel detector. The source is a micro-focus 150 kV Hamamatsu X-ray source with a tungsten target. By varying the filament voltage and current, a 100 kV filament voltage and a 100 μA was found to provide the best contrast and lowest noise in the reconstructed foam images at high spatial resolution. The image magnification was determined by the source-detector distance (SDD) and the source-object distance (SOD). The magnification M is then given by $M = \frac{\text{SDD}}{\text{SOD}}$. In the majority of experiments, SDD was set at 130 mm and SDD at 390 mm resulting in a three-fold magnification factor. This maps a 17 μm^2 sample area onto a detector pixel of size 0.05 mm^2. By varying SDD and SOD, magnification values between 2 and 6 were achievable. Larger magnification requiring a large SDD, resulted in increased image noise due to the additional air through which the X-ray beam must pass.

The sample was mounted on a precision rotation stage from Huber Germany, which rotated the sample through 360^o during the imaging process. A 360^o sample rotation was required due to the cone-beam geometry of the X-ray beam produced from our source. As the sample is rotated, several images or projections of the sample were recorded. The more projections which were recorded, the greater the image quality of the resulting reconstructed image. However, due to the limited lifetimes of the foam samples that we were examining, the number of projections had to be significantly reduced to lower the imaging time. Our samples were formed from 500 image projections. Due to the presence of several defects within the detector itself, normalising images were first taken before imaging. In particular a set of 'open' and 'closed' beam images, corresponding to direct imaging of the X-ray source while activated and deactivated, were captured. These images were later used during the image reconstruction phase.

2.3.3 Image reconstruction

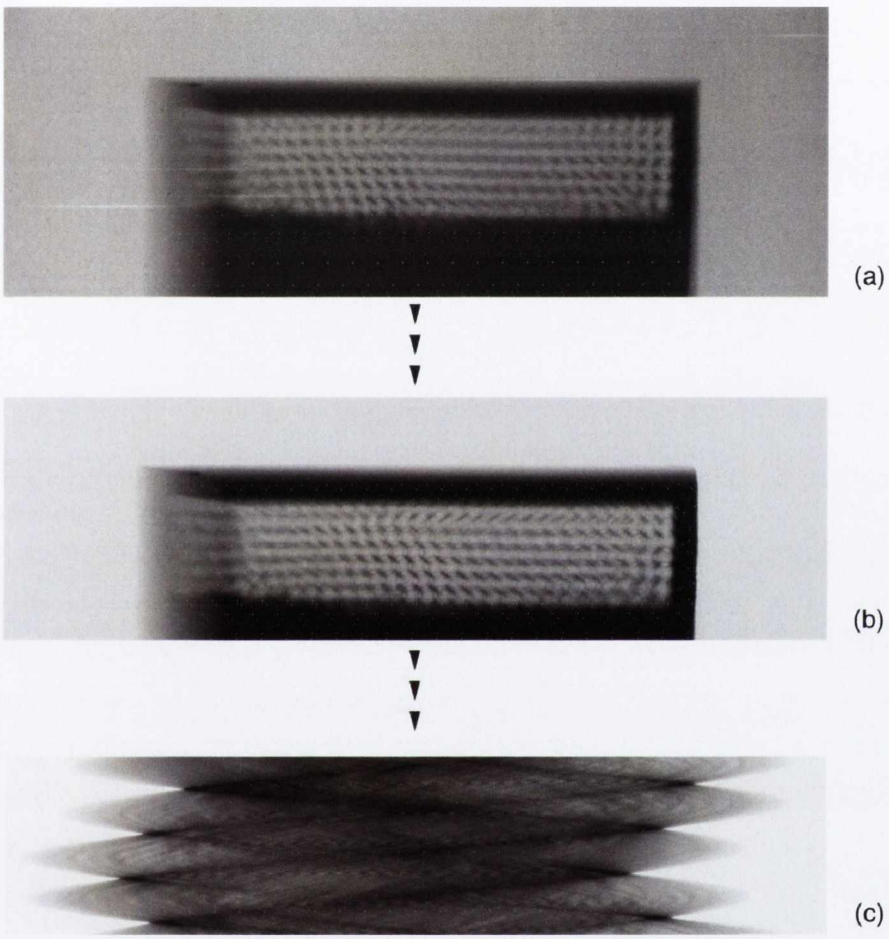

Figure 2.4: Composite images illustrating the image processing steps required to progress from a series of vertical projections of the imaging object to a series of horizontal slices through the object. (a) shows an example of the initial images captured during the acquisition process. 500 such images are recorded at 0.72^o increments of rotation of the sample. Several horizontal white lines across the image are observable. These defects are caused by dead pixels in the detector array. (b) shows the same image after defect correction and normalisation. The intensity gradient across the image has been equalised and the dead pixel defects have been removed. (c) The generation of the sinogram from the corrected images.

The image reconstruction process - the transformation from the image projections into two-dimensional image slices - was conducted using the commercially available software *Octopus* V8.2 [53]. This software is based upon a back-projection algorithm with convolution and correction for the cone beam geometry. The 500 sample projections, combined with the 10 open and 10 closed beam images, were selected for processing. The original images were cropped to the areas of interest so as to reduce processing time. A region outside the bounds of the object was chosen for normalisation purposes. The 500 images were then re-normalised such that this section has constant intensity over all 500 projections. This is necessary to compensate for the variation of the X-ray intensity produced by the source over time. This variation in beam intensity leads to non-isotropic image contrast in the final images if uncorrected. A ring filter value of 3 was chosen for historical purposes to remove the effect of dead detector pixels (see Fig.2.4) [54]. Such dead pixels, of constant intensity, would produce rings in the final reconstructed images if left uncorrected. After the image-stack normalisation procedure, the sinograms – a visual represenation of the Radon transformation – were produced [50]. The sinograms were then combined to form horizontal slices through the image through the application of the central slice theorem. To do so, however, requires setting the three dimensional object centre so that the resulting image reconstruction was clear throughout the sample. A Gaussian filter was also applied to the image data at this point to reduce image noise.

The reconstructed data is composed of a series of *8-bit greyscale* images measuring 1500 x 1500 pixels (see Fig.2.5). This means that each pixel of the reconstructed image has a value in the range [0:256]. A pixel value of 0 corresponds to pure black while a value of 256 corresponds to pure white. Each image represents a horizontal slice, 15 μm thick, taken through the sample (for a magnification factor of 3). These images may be combined to form an *image stack*, a sequential series of images that may be used by rendering software such as *3DstudioMAX* to produce three-dimensional renders of our

foam samples [55].

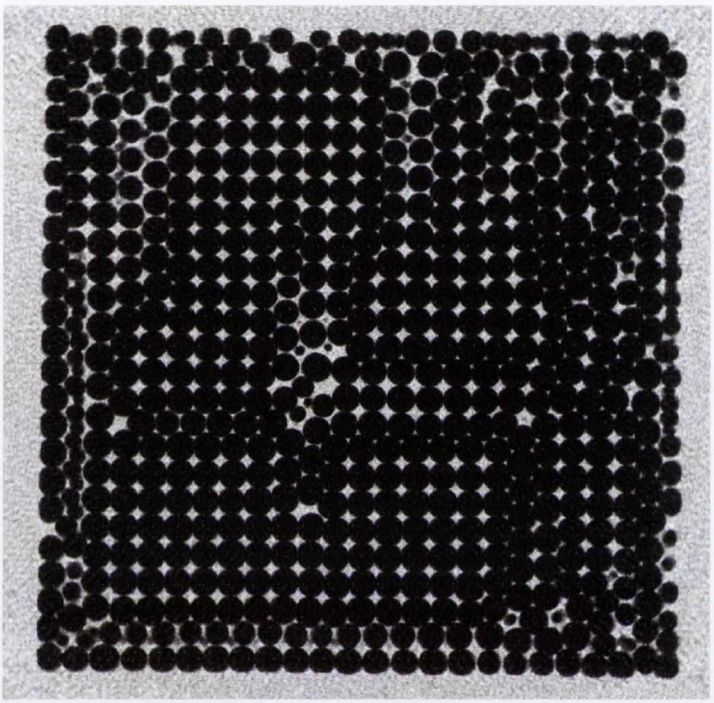

Figure 2.5: A two-dimensional image slice taken through an ordered foam showing the image data produced following successful image reconstruction. Dark segments of the image correspond to the gas phase of the foam, while brighter areas of the image correspond to the liquid phase. Due to the similarity between the linear attenuation coefficient associated with the surfactant solution and the container of the experiment, these two phases cannot be separated in the resulting reconstructed images.

2.4 Image processing

Following the successful imaging, reconstruction and visualisation of a foam using X-ray tomography, we now wish to obtain information, such as bubble

size, position, shape etc. from our data. Due to the thinness of the films of a foam (in the regime of 50 *nm* [6]) being below our current imaging resolution, such features are not present on the reconstructed images and thus individual bubbles do not appear as separated objects (Fig.2.6). If a simple segmentation was applied to the image data at this point, only one particle composed of the bubble-conglomerate would be identifiable.

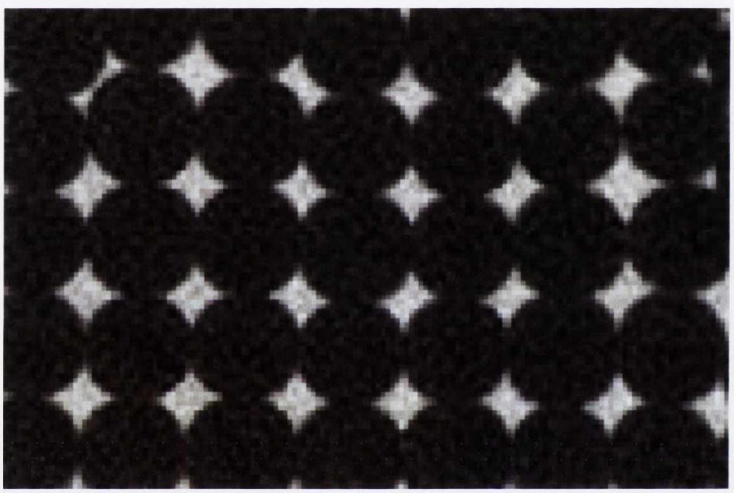

Figure 2.6: Magnified section of Fig.2.5. The Plateau borders and vertices of the foam are clearly visible. However the thin films separating neighbouring bubbles are not present within the image.

It is the function of image processing to reproduce the missing thin films and thus separate the individual bubbles from the position of the imaged vertices. Following this, image segmentation can be performed, resulting eventually in full statistical information about the foam packing. This image processing was conducted using the commercially available software *MAVI*, following a similar procedure as to that employed in the reconstruction of a zinc metallic foam [37]. These steps were:

Filtering

A median filter was applied to the image data. A median filter replaces each pixel with the mean value of its nine neighbours. This reduces image noise associated with digital photographs.

Binarisation

Binarisation is the process by which each greyscale image with pixel values between [0:256] is converted to a binary image for which each pixel has a value of either 0 or 1. This process begins by examining the histogram of pixel values associated with each image slice. An example of such a histogram is shown in Fig. 2.7.

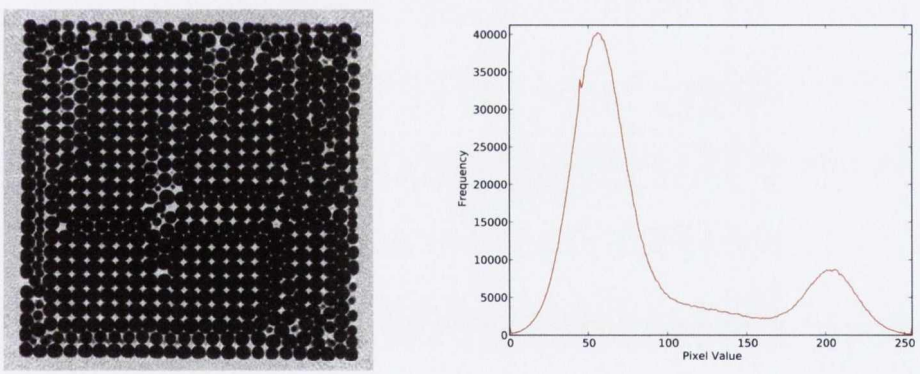

Figure 2.7: (left) Greyscale image slice of foam. (right) Histogram of pixel values shown in the image. Peaks associated with bubbles (dark image area, centred around 60) and liquid (light image areas, centred 210) are clearly seen.

Two peaks are observed in this histogram - one peak is associated with the darker image regions corresponding to the gas phase of the foam, while the second peak refers to the lighter pixels associated with the liquid phase.

Based on this histogram, a threshold value of 98 can be chosen to binarize the image - any pixel with a value less then 98 is set to zero, while any pixel with a value greater than 98 are set to one. The threshold value must be chosen such that the vertices are completely resolved while image noise is limited. If the threshold value is set too high, image-noise will result in over-segmentation of the resulting image. The results of this binarisation process are shown in Fig.2.8.

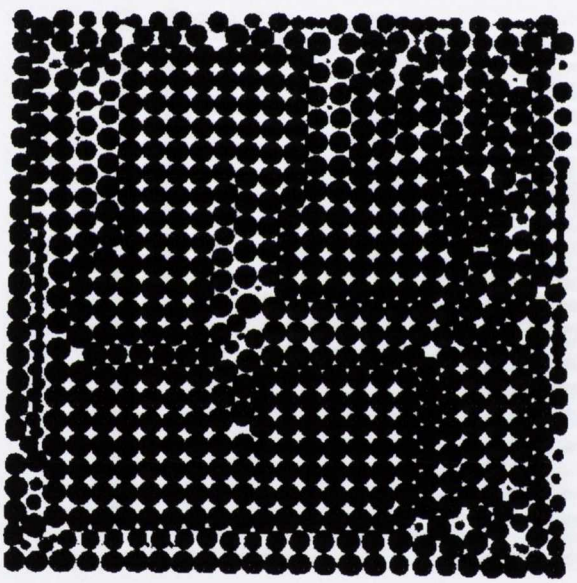

Figure 2.8: Binary image of foam slice. Black regions correspond to the gas-phase and white regions to the liquid phase of the foam.

Distance measure

A *distance measure* is a method by which a greyscale image may be formed from a binary image by assigning each pixel of the background (black regions) a value equal to the minimum distance to the nearest foreground (white

regions) pixel [56]. Fig.2.9 demonstrates this process applied to a single-pixel image.

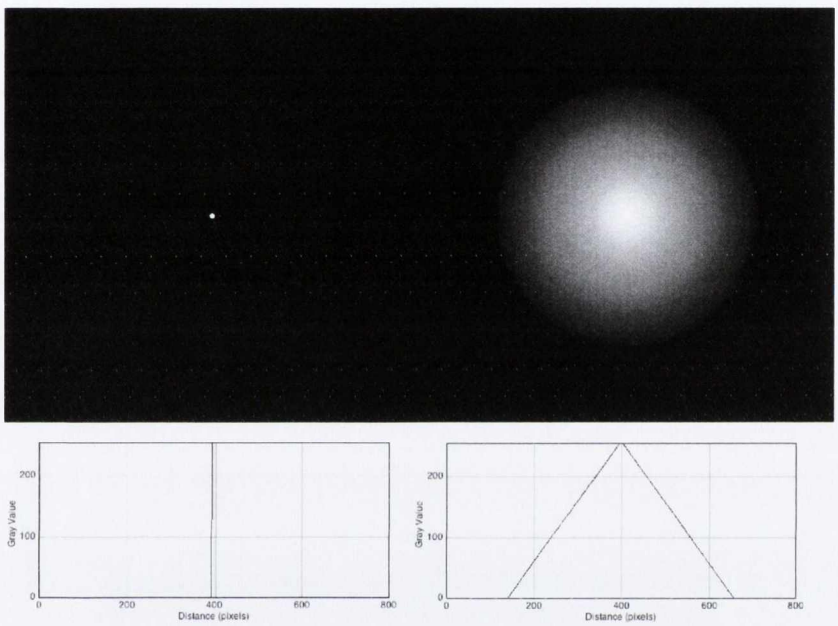

Figure 2.9: Example of the application of the Euclidean distance measure applied to a binary image composed of a single foreground pixel (top left). The distribution of image values is shown below. After applying the distance measure to the image, the resulting pixel values across the image show a linear increase

For this process, distance may be measured using either the *Chebyshev* measure, the *Manhattan* measure, or the *Euclidean* measure [56]. Both Chebyshev and Manhattan distance measures take advantage of the discrete nature of the image data. The Chebyshev considers distance only along the 8 nearest neighbour directions of a particular pixel, while the Manhattan Measure assumes that the distance is measured along the di-

rection of the 4 nearest neighbours, i.e. along the coordinate lines. The Euclidean distance is calculated by embedding the image in a two-dimensional space. The distance between two pixels is calculated using the normal definition of the euclidean metric and rounded to the nearest whole number i.e. the distance between two pixels $p(x_1, y_1)$ and $q(x_2, y_2) = d(p, q)_E = ROUND(\sqrt{(x_2 - x_1)^2 + (y_2 - y_1)^2})$.

Since this measure does not take advantage of the discrete nature of the image data, the Euclidean distance measure is the most computationally inefficient distance measure. However, due to the accuracy and ease of interpretation of this measure, it was used in our calculations. For each background pixel, the distance to the nearest foreground pixel is calculated. The background pixel value is then changed to this distance value. Fig.2.10 shows the euclidean distance measure applied to the binary image slice shown in Fig.2.8.

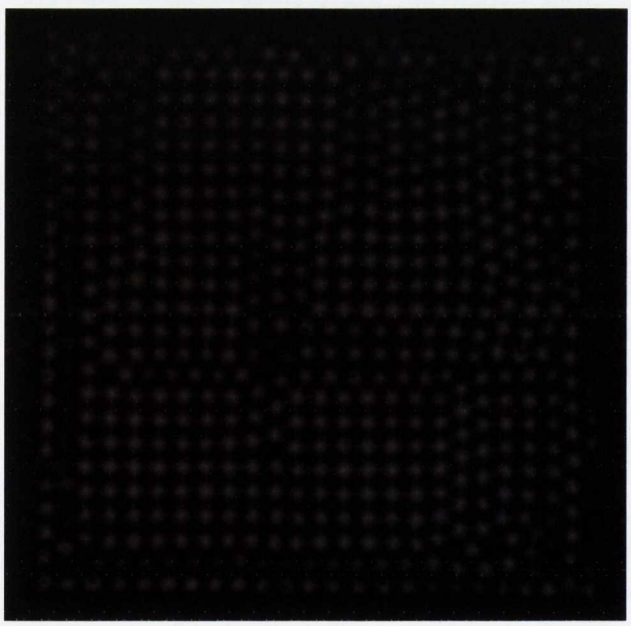

Figure 2.10: Euclidean distance measure applied to binary image slice.

Geodesic Transformation

The euclidean distance transformation results in the formation of a distinct maximum at the centre of each separated bubble. This process, however, produces unwanted maxima associated with signal noise and defects produced during the imaging process. To reduce their effects in the segmentation process, a *Geodesic transformation* is applied to the image.

Geodesic transformations are a set of morphological operators based upon the ideas of a *marker image* f and a *mask image* g [56]. The basic operators of this transformation class are *Geodesic Dilation* and *Geodesic Erosion*. For our purposes - determining the position of *local maxima* within the image data - we need only examine geodesic dilation defined as

$$\delta_g^{(1)}(f) = \delta^1 f \wedge g \tag{2.4}$$

where δ^1 is elementary dilation - the process by which an image foreground object feature is expanded outwards by a pixel value of 1 - and $\wedge$ is the pointwise minimum operator defined as $f \wedge g : X \to \mathbb{R} : (f \wedge g)x = min(f(x), g(x))$. Using δ we may define the morphological operation reconstruction by dilation:

$$R_g^{\delta}(f) = \delta_g^i(f) \tag{2.5}$$

where i is such that $\delta_g^i(f) = \delta_g^{i+1}(f)$ i.e. unitary geodesic dilation is successively applied to the image until the image converges to a steady state. A special case of this reconstruction by dilation operator may be used to suppress unwanted maxima within our image. If f is reconstructed by dilation using the masking image $f - h$, for a user defined f, the so-called adaptive H-Extrema operator is formed, defined as

$$HMAX_h(f) = R_f^{\delta}(f - h). \tag{2.6}$$

When applied to an image, H-extrema operator suppresses all maxima within the image whose maximum image value is less than the user-defined

variable h. When applied to the image, maxima associated with image noise are significantly reduced. The results of the application of the adaptive h-extrema to the experimental images is shown in Fig.2.11.

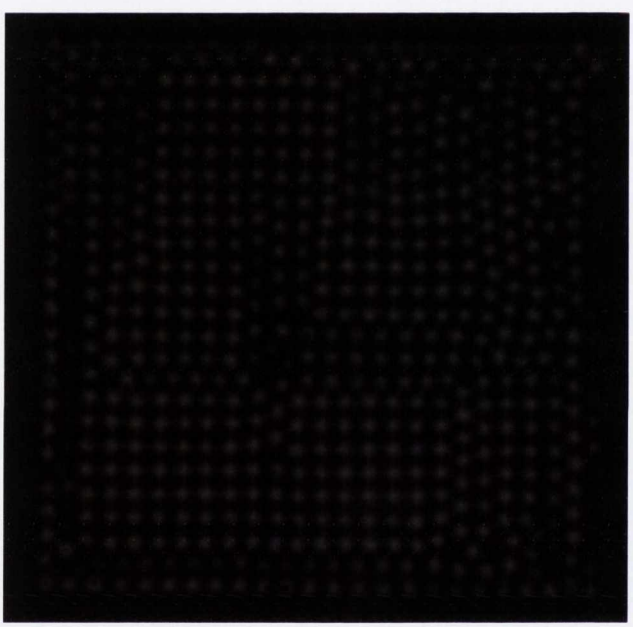

Figure 2.11: Application of the geodesic transformation to the image slice.

Unitary addition

Each pixel value of the image is increased by a value of 1 (see Fig.2.12). This maintains image detail in the following processing steps when images are subtracted.

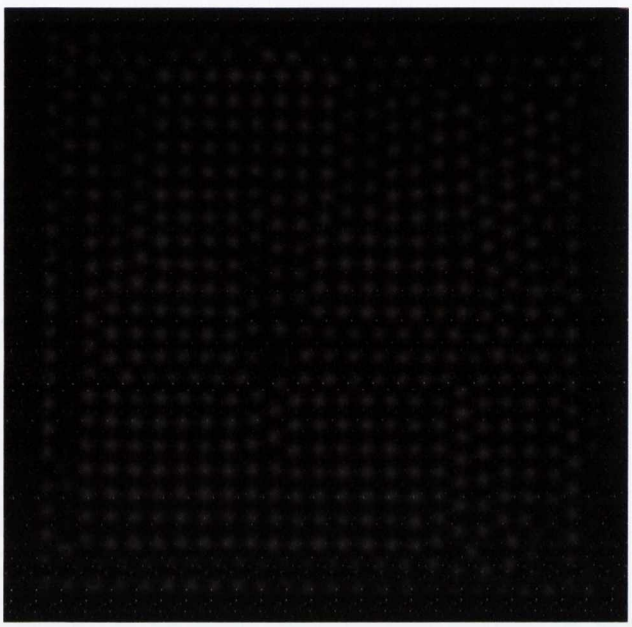

Figure 2.12: Application of unitary addition to the image slice.

Inversion masking

The original binary image shown in Fig. 2.8 is inverted and used as a mask, see Fig. 2.13. The image is inverted using the simple procedure $f(i) = |256 - f(i)|$ for each pixel i of the image. This process replaces each 0 value pixel with a 256 value pixel and a 256 value pixel with a 0 value pixel. The resulting image was used to *mask* Fig. 2.12. The process of masking involves the multiplication of the two images i.e. for two images f and g, the product of the image multiplication $h(x, y) = f(x, y) * g(x, y)$. The multiplication by the binary image - where each pixel has a value 1 or 0 - means that only those highlighted features are kept in the final image.

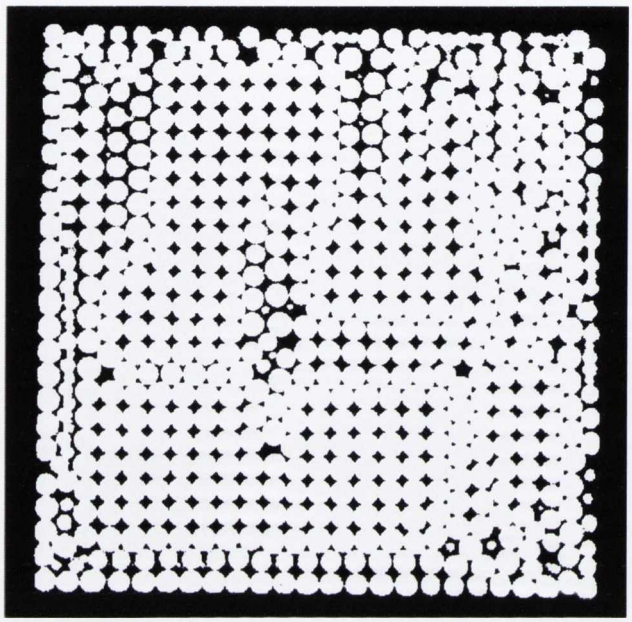

Figure 2.13: The inverse binary image used as a mask to reinstate feature borders.

2.4.1 Inversion

The image is inverted again. Following this inversion process, the image now contains a series of minima located at the centre of the original bubbles. With each separate bubble now marked, the segmentation of the image can be completed using the *watershed transformation.*

2.4.2 Watershed Transformation

The watershed transformation is a method by which an image may be subdivided into a series of connected regions sharing particular characteristics [56]. In this case, the criterion used for segmentation is that the final regions of the image should correspond to separate bubbles.

The watershed transformation is based upon visualising the greyscale image as a topological surface, the height of each point being equal to the value of the corresponding pixel value. The watershed transformation succeeds in calculating the location of the various catchment areas associated with this surface - i.e. the various separated areas in which fluid would collect if water was poured onto the surface. These catchment areas are calculated by simulating a flooding of the image, the sources of liquid located at the regional minima of the image. As more liquid is added to the image, the height reached by liquid in the image is increased. This leads to the water table of a given minimum increasing in extent. Where two adjacent water tables meet, a border region is created to separate the connected regions.

The watershed transformation is an efficient method used to segment an image. It is typically used for the separation of overlapping objects within an image. The process begins by determining the local pixel minima within the image. In this case, these local pixel minima correspond to the bubble centres. Each of these minima is assigned a pixel number and becomes a *basin* for the following flooding step. Each basin is expanded outwards from the central basin until contact is made with the surrounding expanding basins. When this occurs, a boundary region - set with pixel value 0 - is established. When each pixel of the image has been assigned a new value - either a basin label or a boundary value of 0 - the watershed process has finished. The resulting image can no-longer be considered as a greyscale value. Rather than image intensity or distance, each pixel value now refers to a *connected region* within the image.

Figure 2.14: Application of the watershed transformation. Each connected domain is given a unique numeric identifier, corresponding to a unique colour.

2.4.3 Masking

During the watershed transformation step, information regarding the original image geometry has been lost. In particular, the positions of the Plateau borders and vertices of the foam are no longer present. Using the binary image shown in Fig.2.13, the watershed image in Fig. 2.14 was masked to take into account the presence of these lost image features (see Fig. 2.15). At this stage, the image data is saved as a ".RAW" image format type. This Raw data type allows the image data to be successfully imaged as individual bubbles using visualisation software such as 3DStudioMax [55]. Examples of such visualisations are shown in figures 2.15 and 2.16.

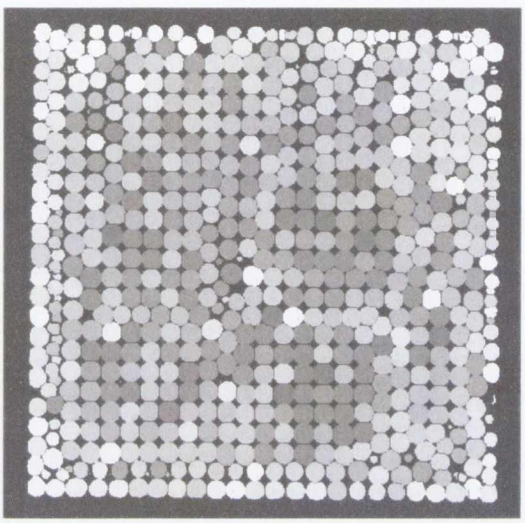

Figure 2.15: The masked watershed image. The connected domains within this image correspond to individual bubbles.

2.4.4 Object details

Statistics regarding the connected domains shown in Fig.2.16 may now be calculated. Important statistics including object position, volume, surface area, Euler number and shape factor are easily obtainable. The centre position of each connected domain is determined by calculating the cube of minimum volume in which the image feature may be inscribed. The resulting image data is outputted in the form of a text file the data of which may be easily analysed using a variety of computer programmes. The majority of data analysis is conducted using the programming language Python, with the installed extensions Numpy and Scipy [57, 58].

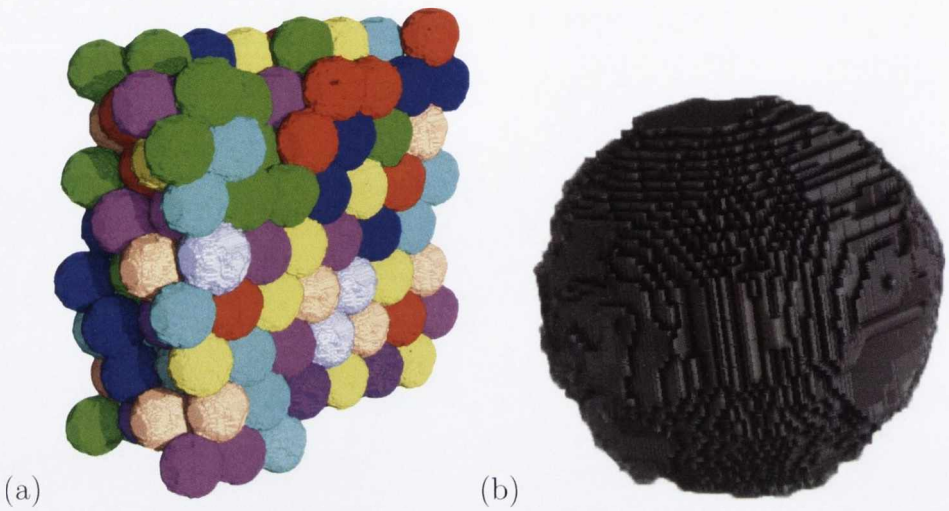

(a) (b)

Figure 2.16: Visualisation of the segmented tomographic data using 3DStudioMax. (a) Conglomerate of bubbles individually coloured to demonstrate the successful segmentation of the image data (b) Visualisation of an individual bubble produced during image segmentation. The individual voxels of the object can be seen.

2.4.4.1 Data filtering

Following successful segmentation of the image data, a statistical analysis of the bubble sizes and positions was then conducted. During this analysis, several anomalous readings were observed in the object data. This was most obviously demonstrated through a calculation of the sphericity of the particles.

The sphericity S of a particle is a measure of the divergence of the shape of a three-dimensional particle from a sphere of the same volume [50]. In mathematical terms, the sphericity of a particle S is given as

$$S = \frac{\pi^{\frac{1}{3}}(6V_p)^{\frac{2}{3}}}{A_p}, \tag{2.7}$$

where V_p and A_p correspond to the volume and surface area of the particle in

question. For continuous three-dimensional objects the maximum sphericity $S = 1$ corresponds to a perfect sphere. A divergence from this spherical shape will lead to an increase in the surface-to-volume ratio resulting in a decrease in the sphericity measure e.g. the sphericity of a cube is $\left(\frac{\pi}{6}\right) \approx 0.8$. The sphericity of the particles identified for a typical sample sample is shown in Fig.2.17.

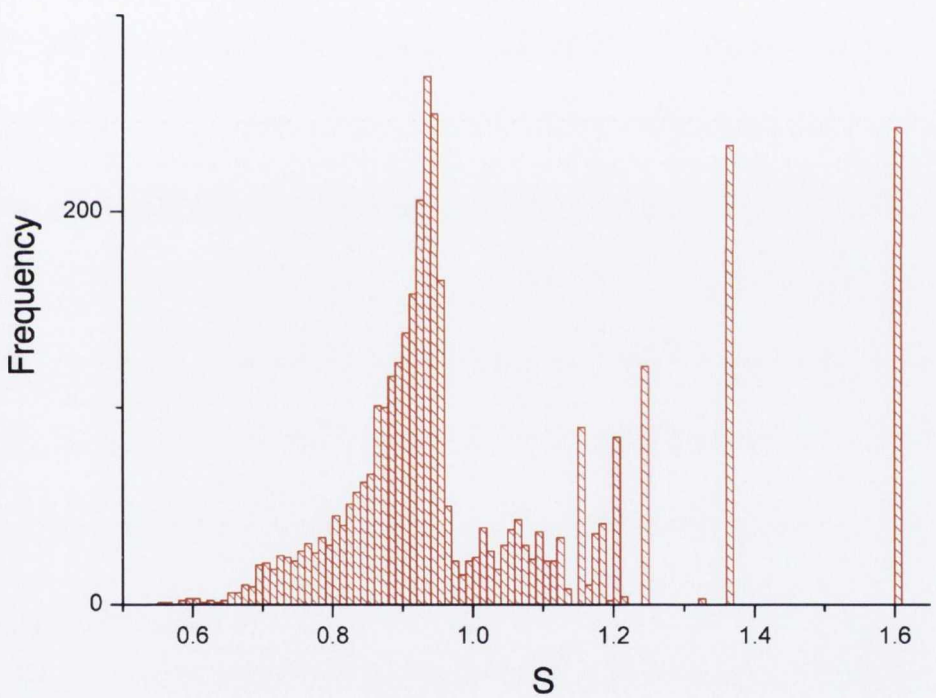

Figure 2.17: Histogram of the sphericity S for the particles within a typical foam sample. Note that there is a large peak centred at approximately 0.9, corresponding to the bubbles of the sample. However, there are many particles for which the sphericity is above the physical maximum value of 1.

Although there is a peak in sphericity at $S \approx 0.9$ corresponding to the bubbles of the experiment, it is also apparent that the sphericity of some of the particles within the system exceeds 1. This result is non-physical for continuous three-dimensional shapes.

We believe that this non-physical result is due to over-segmentation of the original image data. This may result in objects not topologically-equivalent to spheres within the object data. For such objects within *discrete* three dimensional data, it may be possible for the associated sphericity to be greater than 1 due to the difficulties associated with defining the surface area of individual voxels. Such problems may be overcome by examining the *Euler number* of each particle identified within the object data

The Euler characterisation is a method of identifying an object as a member of a particular topological class [56]. The *Euler number* or *Euler Characteristic*, χ, is defined as

$$\chi = V - E + F \tag{2.8}$$

where V, E and F are the number of vertices, edges and faces of the shape. For a continuous object, the Euler characterisation is determined from a triangulation of that object. It can be shown that the Euler characterisation of an object is independent of the chosen triangulation[56]. For the case of a sphere, or any object topologically equivalent to a sphere, $\chi = 2$. Other objects, e.g. tori, have associated with them a different Euler number (0). We filtered our data such that only those objects with $\chi = 2$ were allowed. The new distribution of sphericity, filtered against Euler number, is shown in Fig.2.18.

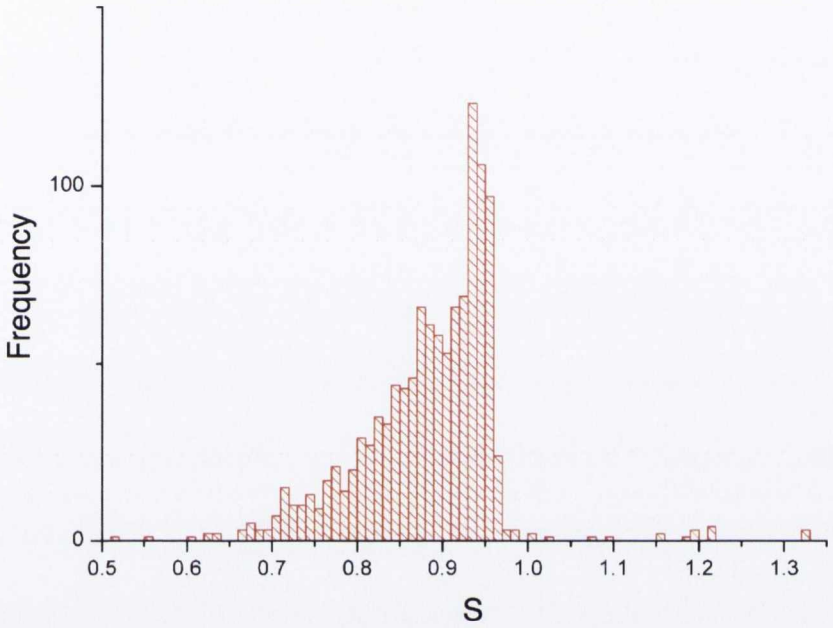

Figure 2.18: Sphericity of the foam sample as filtered using Euler number χ. By excluding all objects which are not topologically equivalent to a sphere, it is seen that the majority of those particles with $S > 1$ have been significantly reduced.

This filtering process removes the majority of those objects with the non-physical sphericity $S > 1$. When an analysis of our filtered data was then conducted, it was found that the majority of segmentation noise had been eliminated which had been previously causing difficulty had been removed.

Chapter 3

The bulk ordering of monodisperse foam

In this chapter the three dimensional structure of monodisperse aqueous microfoam will be discussed. The structure of monodisperse foam samples will be first studied through a visual inspection of images reconstructed from the tomographic data, the acquisition process of which was described in Chapter 2. Following this, a statistical analysis of the foam positional data will be conducted. This statistical analysis will focus on various order parameters previously employed in the study of a variety of granular systems. In particular we will examine the coordination number, the radial distribution function, the Steinhardt order parameter and the packing-fraction associated with each foam packing. Using these analytic techniques, we will investigate how foam structure depends upon sample size and age.

3.1 Experimental method

Monodisperse microfoams are produced using the apparatus shown in Fig. 2.2. The surfactant solution used was a 5 % by volume aqueous solution of the commercially available detergent *Fairy liquid*. This is found to produce

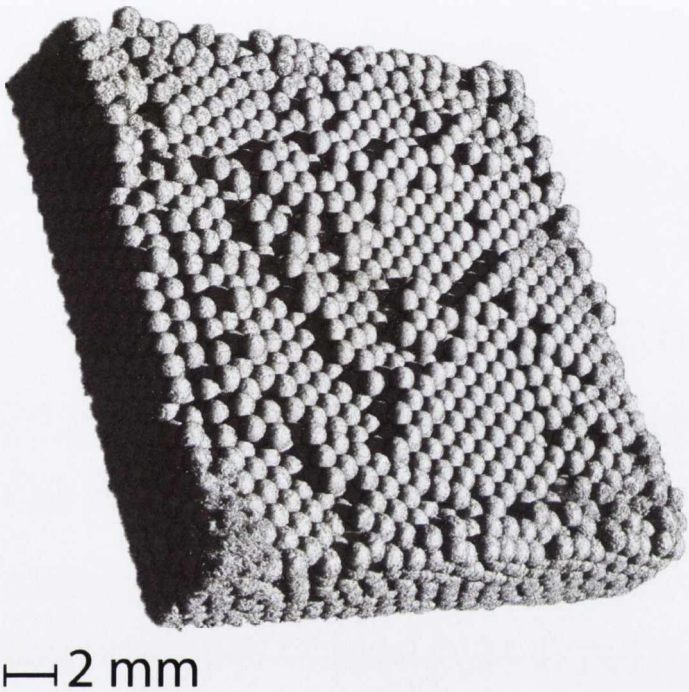

Figure 3.1: X-ray tomographic image of an ordered monodisperse foam composed of 5000 bubbles of average diameter 780 $\pm$ 40 μm. The bubbles are seen to arrange into a sample approximately 5 bubbles deep.

stable foams suitable for a wide range of experiments [59]. The gas phase was a combination of Nitrogen and Perfluorohexane (PFH).

Bubble samples were periodically taken from the output of the flow focusing device and analyzed to determine the bubble diameter distribution. Once a stable foam of desired bubble size and dispersity was produced, a sample was collected into the container shown Fig. B.1. By varying the collection time the number of bubbles captured could be changed, thus changing the container filling depth. The container, now filled with a mixture of bubbles and liquid, was closed within the solution by sliding a glass plate over the

opening of the container. The filled container was then removed from the solution and mounted on a plastic plinth, after which it was imaged using our μCT X-ray tomographic device. The resulting tomographic data was processed using *Octopus* and segmented using *MAVI* as detailed in Chapter 2.

3.2 Variation of sample crystallisation with filling depth

The structure of the foam samples was analysed as a function of their filling depth. It was found that the foam samples could be divided into two distinct groups - *thin* samples and *thick* samples. For our purposes, a sample will be considered "thin" if the number of foam layers is less than or equal to 10 and thick if the number of foam layers exceeds this number. It is found that the ordering behaviour of the foam systems is well described by this divide.

3.2.1 Thin samples

The first samples investigated using X-ray tomography were composed of a few thousand bubbles, forming foam samples which extended only a few mm above the foam-liquid interface. In this manner it could be guaranteed that the foam sample had a high liquid fraction, providing the best chance of obtaining images suitable for successful image reconstruction. Fig.3.1 shows the holotype[1] for these thin foam samples. It is composed of roughly 5000 bubbles, of average bubble diameter 780 $\mu m \pm 20$. These bubbles have arranged into a foam sample 8 bubble layers thick.

The ordering behaviour of this foam sample is immediately apparent on investigating the first reconstructed images. These images are formed by

[1] A holotype is a term I have procured from biology which I feel fits quite well here - a holotype is a single physical specimen used for the description of a species.

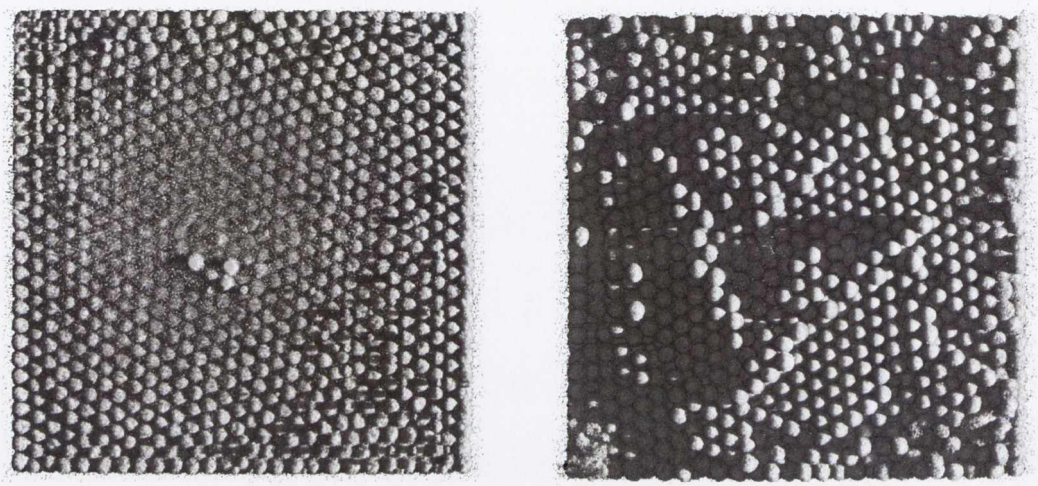

Figure 3.2: Image of a monodisperse microfoam of average diameter 780 ± 20 μm. (A) the top of the foam and (B) the bottom of the foam are separately visualised. On both the top and bottom of the foam, the bubbles are seen to order into hexagonal arrangements of bubbles.

showing only the gas phase of the foam sample. The resultant images show the foam as a packing of spheres. On examination of the top and bottom of the foam (see Fig.3.2), referring to the section of the foam in contact with the liquid and that in contact with the container respectively, it is seen that the bubbles of the foam are arranged into a two-dimensional hexagonally closed packed structure.

By examining the liquid phase of the foam, the Plateau borders and vertices of the foam sample may be shown instead. As previously discussed, the films separating neighbouring bubbles can not be captured by the particular tomographic method employed here due to their thinness [6]. This results in an examination of the liquid phase only resolving the Plateau borders and vertices of the foam sample.

However, our imaging shows the Plateau borders and junctions of the foam sample allow the internals of the foam sample to be examined more closely than possible when viewing the gas phase alone. Fig.3.3 shows a reconstruction focusing on the liquid phase of the 4^{th} layer of the foam sample. The regular, ordered nature of the Plateau borders and lattices indicated that the previously observed surface ordering extends into the bulk of the foam sample.

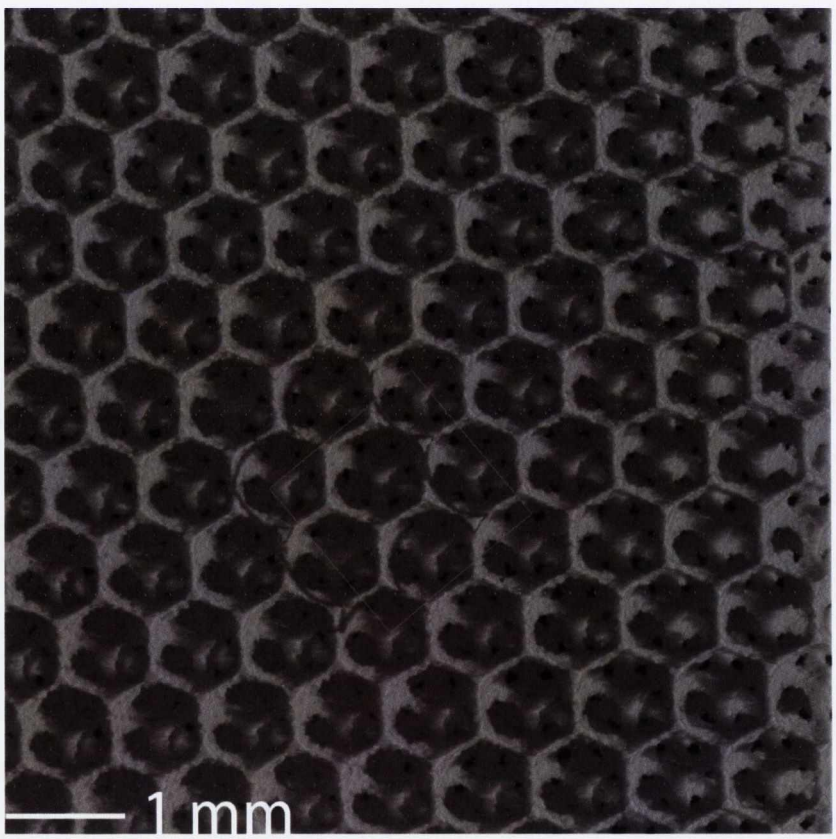

Figure 3.3: Reconstruction image of the thin foam sample, 5 layers deep, highlighting the liquid phase of the foam sample. The Plateau border and vertices of the foam are clearly visible, their regular, repeating structure indicating the presence of order within the center of this sample.

Following these general observations of order within these foam samples, closer inspection of the reconstructed data can yield much greater information about the foam structure. By examining the stacking pattern of successive layers within the foam crystal, the nature of the ordering of the system can be determined. Fig.3.4 shows a selection of the topmost three layers of the thin foam sample. The bubbles within the selection have been coloured blue, green and red as they correspond to the A,B and C layers generally associated with closed-packed structures [60]. We can extend this method of identifying the crystallisation of the sample throughout all foam layers. The results of such an analysis are shown in Fig. 3.5.

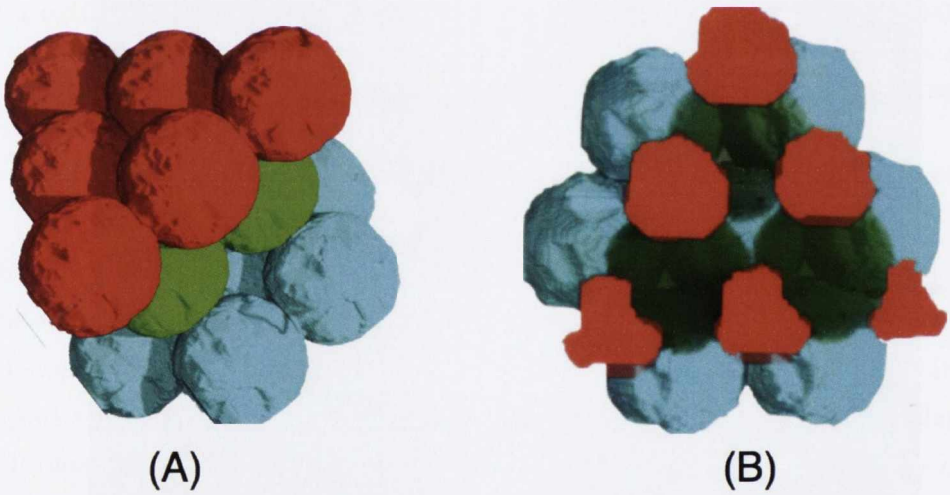

Figure 3.4: A selection of bubbles from the top of the thin foam sample colored red,blue and green to correspond to the A,B and C packing layers of spheres. These sets of bubble are therefore seen to order into an fcc arrangement. (A) shows the selection of bubbles from a profile angle, while (B) shows the bubbles from above. Transparencies have been employed to make the lower layers of the selection more visible.

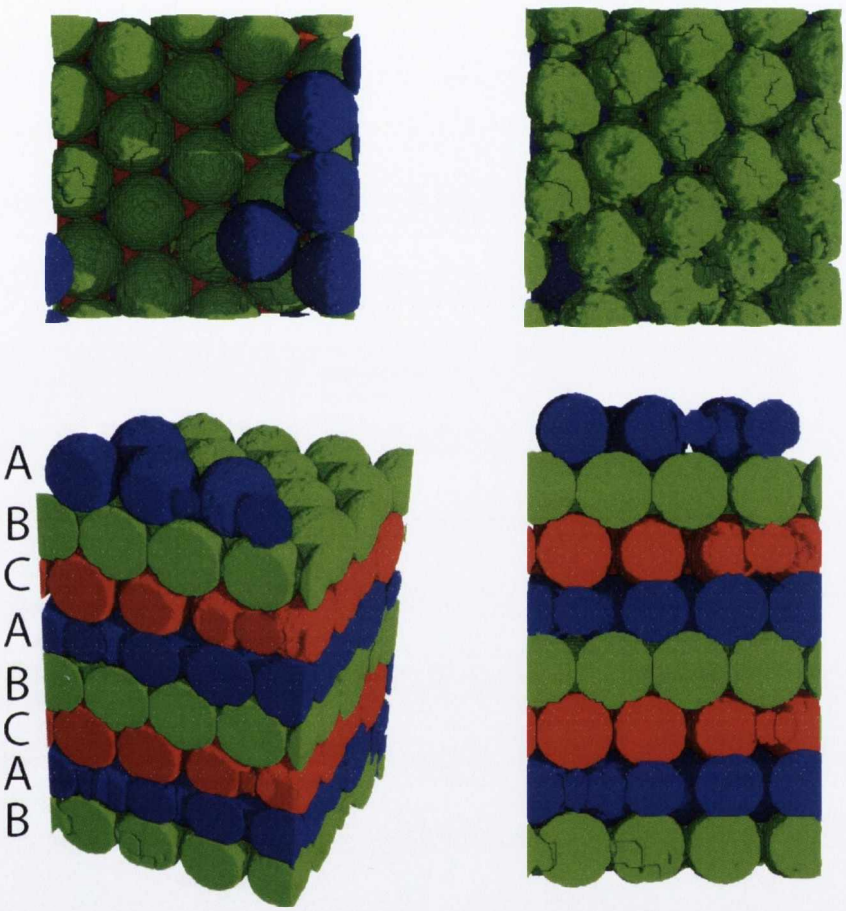

Figure 3.5: A cuboid extracted from the center of the foam sample. The layers of the foam have been coloured red,blue and green to correspond to the A, B and C packing layers of spheres. It is seen that the foam sample is composed of an ABC packing of spheres throughout its width, indicating that the observed surface crystallisation extends into the "bulk" of this thin sample. (i) shows the sample as viewed at the foam-liquid interface, while (ii) shows the top of the foam far from this interface. (iii) and (iv) show different side aspects of the same foam.

It is seen that the ABC packing of bubbles extends through all layers of the foam structure. This indicates that the observed surface fcc crystallisation of the sample extends into the "bulk" of these thin foam samples, although it must be recognised that no part of this foam sample is more than 8 bubble diameters away from the boundary of the sample.

On viewing the individual layers of the foam sample, many interesting defects within the crystal structure were observed. Fig.3.6 shows several sequential layers of the thin foam sample. On each layer the defects present are highlighted. In particular, there exists a grain boundary between two regions of distinct fcc crystallisation (Fig.3.6 A and B). It is also seen that there is a deformation of the crystal lattice around a larger bubble which was accidentally introduced into the foam (see in Fig.3.6 C and D).

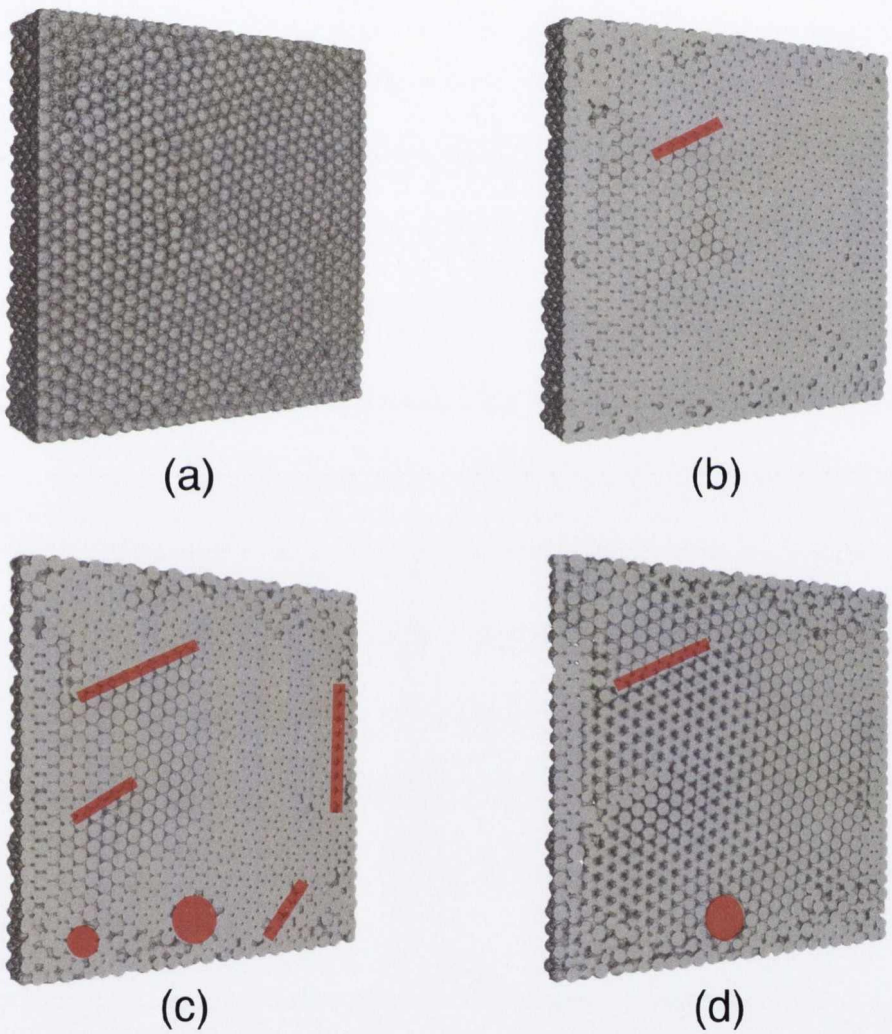

Figure 3.6: Several sequential layers of the thin foam sample. Grain boundaries are highlighted are highlighted using lines, while vacancies are shown with circles. (a),(b),(c) and (d) show successive foam layers from the top of the foam sample.

After this visual inspection of the foam sample, we processed the image data using MAVI as described in Chapter 2. We first fitted several distributions, including log-normal, Lorentzian etc. to the bubble diameter distribution. It was found that the distribution was best described by a Gaussian distribution, although slight deviations were found to occur (see Fig.3.7). However, for our purposes, such deviations are not significant. The sample was found to have a mean diameter of 730 $\pm$ 20 μm. This results in a dispersity less than 5%, classifying the sample as monodisperse.

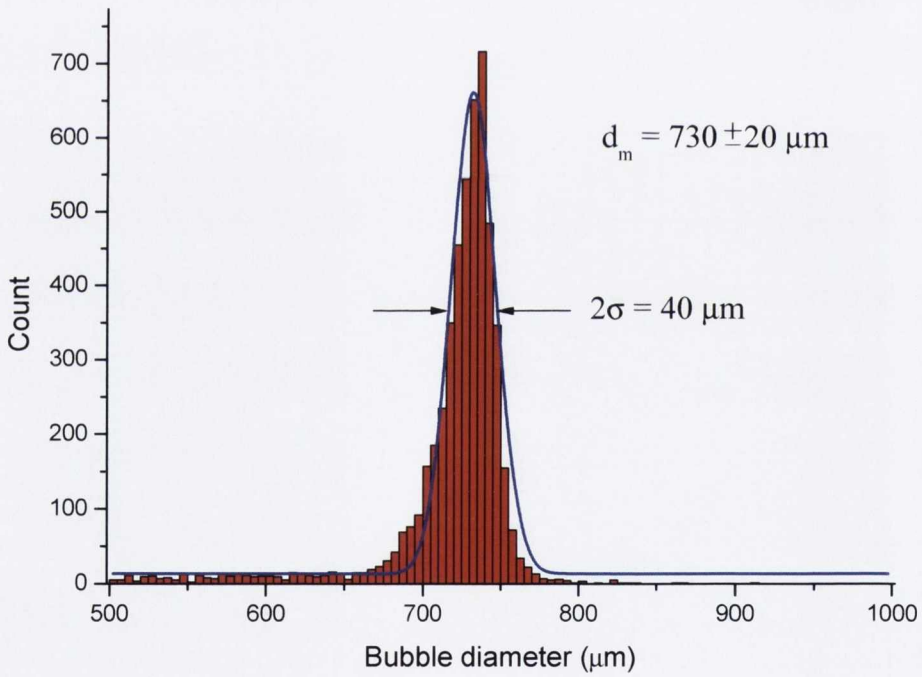

Figure 3.7: Distribution of bubble size following filtering by sphericity and Euler number. The distribution was fitted using to a Gaussian distribution with a mean of 730 $\pm$ 20 μm.

The coordination number as calculated for the thin sample shown in Fig.3.1 is plotted in Fig.3.8. The distribution shows two separate peaks located at $n = 9$ and $n = 12$. Both of these peaks correspond to the presence of hexagonally closed packed ordering within the sample. The $n = 12$ peak corresponds to hexagonally closed packed ordering within the foam bulk, while $n = 9$ corresponds to the same ordering, truncated by the limits imposed upon the sample by the boundary.

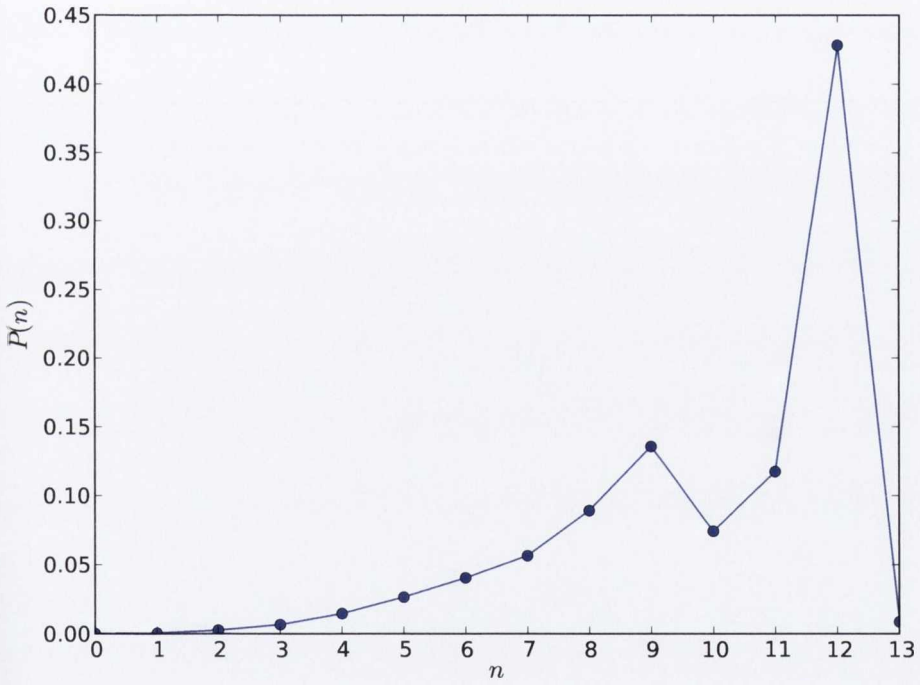

Figure 3.8: Plot of the probability distribution $P(n)$ of the coordination number n for the thin foam example shown in Fig.3.1.

The radial distribution function of the first thin sample is shown in Fig.3.9. The experimental plot (black line) shows the RDF function as cal-

culated for a cubic section of 800 bubbles within the center of the foam bulk. This is a necessary requirement of the RDF function, as a calculation of the experimental curve would be skewed by particles along the foam boundary for which the symmetry of the system has been broken. When compared to the theoretical RDF of an ideal lattice (Red delta functions), it is seen that there is a good agreement between theoretical and experimental peak position up to a distance of $\frac{r}{r_0} = 4$. It is seen that the amplitude of the experimental curve decreases more rapidly than the theoretical prediction suggests. This is due, in part, to the imperfections in the fcc lattice, mainly due to the dispersity of the foam sample.

3.2.2 Thick foam sample

A typical example of a thick foam sample is shown in Fig.3.10. The foam is composed of 20,000 bubbles of average diameter $800 \pm 40\ \mu m$, arranged into a sample 20 bubble layers thick. Unlike in the case of the thin foam samples, in which the ordered nature of the foam sample is identifiable from the surface ordering of the bubbles, such an analysis is not possible on these thick foam samples. Fig.3.10 show the (a) top, (b) side and (c) bottom of the foam sample. While hexagonal ordering is observed along the top and sides of the foam sample, the same ordering is not present along the bottom of these thick foam samples, at the foam-liquid interface. Instead, an apparent random positional arrangement of spheres is seen to occur.

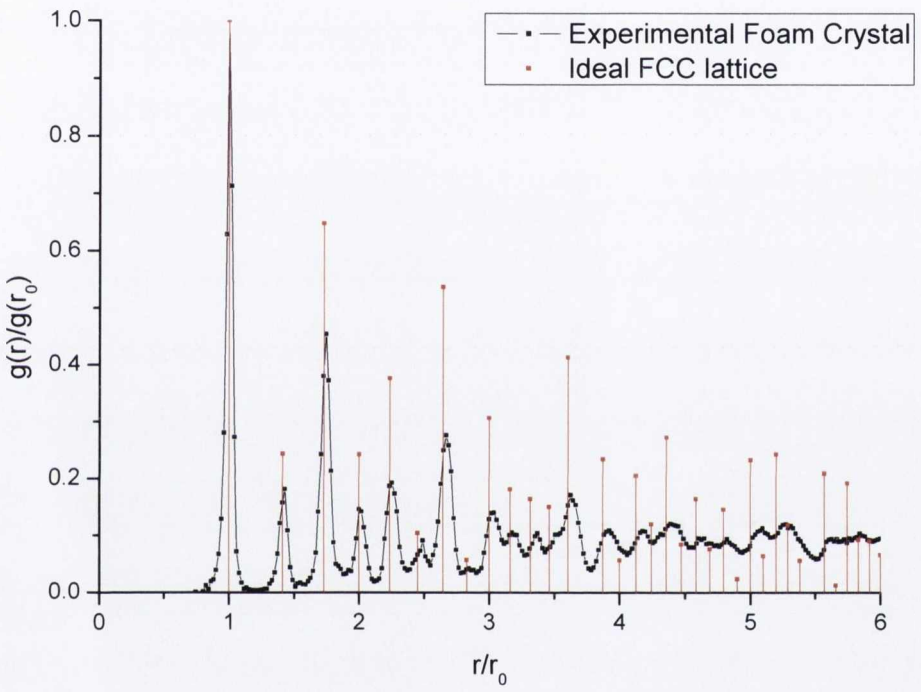

Figure 3.9: Calculation of the radial distribution function g(r) for the thin foam sample. The experimental radial distribution function calculated for the bubble crystal (black) is compared to g(r) calculated for an ideal fcc lattice (red). The radial positions, r, of each peak is normalised by the radial position of the first peak of each distribution r_0. This corresponds to the minimum particle separation in both the fcc lattice and the bubble crystal. The coincidence of the experimental and theoretical peaks at the same position indicate that the foam has formed an fcc lattice.

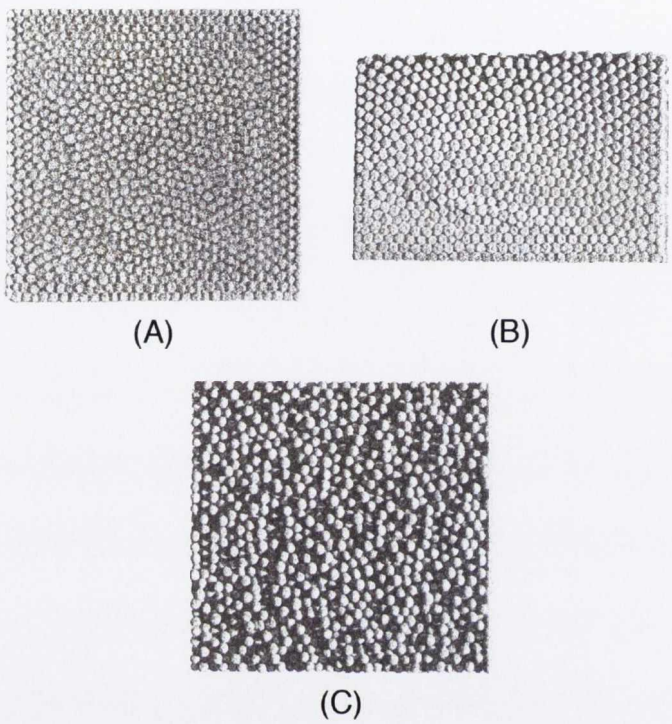

Figure 3.10: A reconstruction of the thick foam sample showing (A) the top of the foam and (B) the side of the foam and (C) the foam bottom. The top and side surface layers of the foam sample exhibit hexagonally closed-packed structures similar to those seen with the thin foam sample shown in Fig.3.2

The internal structure of the foam may be examined by investigating a two-dimensional horizontal section taken through the foam bulk. Such a section is shown in Fig. 3.11. It is seen that bubbles form regular arrangements when in proximity to the boundaries of the sample. However, far from the boundaries of the sample, in the foam bulk, the bubbles show no apparent order. This is again seen if we excise this central region and conduct a visual inspection of the bubble center positions (see Fig.3.12). Again, no apparent order is seen.

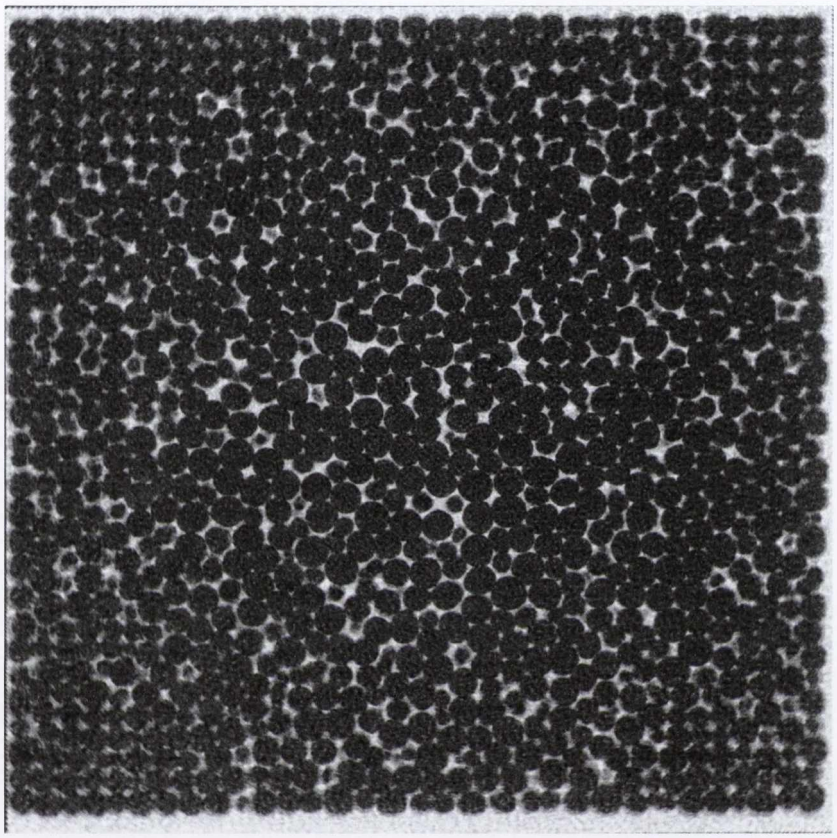

Figure 3.11: A horizontal slice taken through the 11^{th} layer of the thick foam sample showing the distribution of the liquid phase. Darker regions shown the position of the gas associated with each bubble. The bubbles appear to be regularly arranged when in proximity to the boundaries of the sample, however on extending

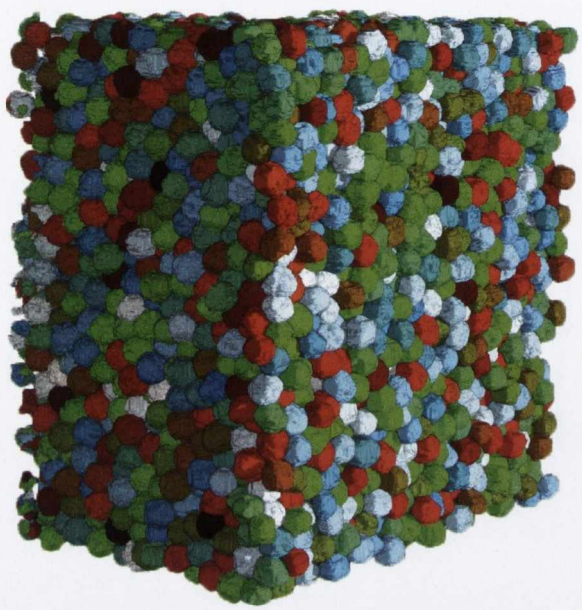

Figure 3.12: The internal structure of the thick foam sample. No apparent order may be seen within the bubbles. The sample is coloured so as to enable neighbouring bubbles to be easily distinguished.

To determine the exact nature of this thick foam sample, we conducted the same analysis as was performed on the thin foam sample. The coordination number and radial distribution functions were again calculated.

The coordination number of the thick foam sample is shown in Fig.3.13. When compared to the distribution associated with the thin foams sample, (Fig. 3.2), it is seen that the distribution is composed of a single peak. Several other differences are observed:

- The $n = 9$ peak which corresponds to the ordering of particles at the surface of the sample, is less obvious when compared to the thin foam sample. This is due to the loss of order seen along the bottom face of the sample.

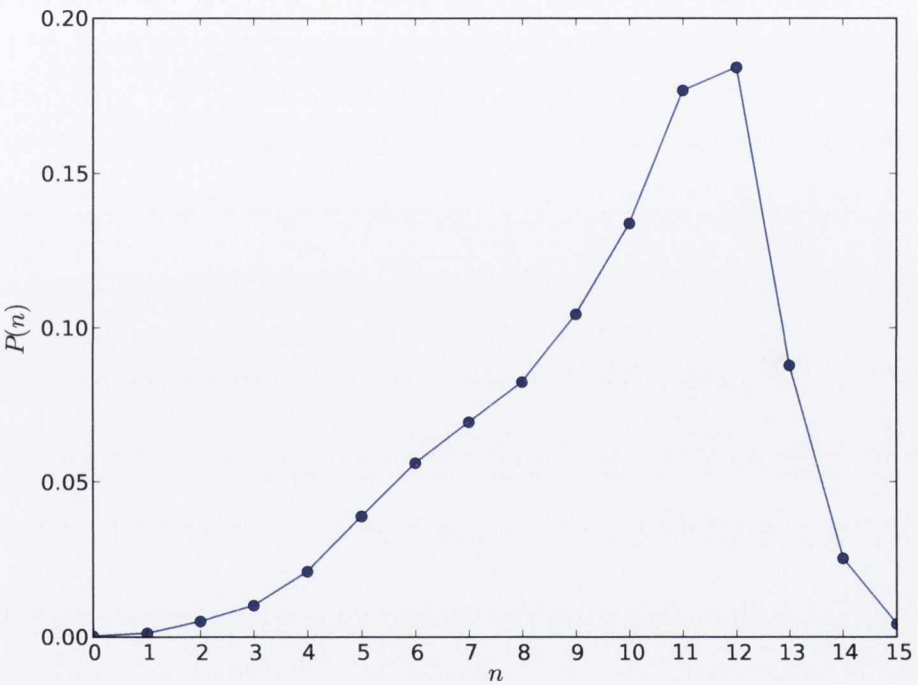

Figure 3.13: Plot of the probability distribution of contacts $P(n)$ versus n for the thick foam example shown in Fig.3.10.

- $P(n)$ still displays a peak at $n = 12$, but now there is a smooth increase of $P(n)$.

Following the calculation of the coordination number, we then calculated the RDF of the thick foam sample, the results of which are Fig. 3.14. It is seen that the functional form of the RDF distribution is significantly different to that shown for the thin foam sample (see Fig.3.9). The sharp peaks indicative of a crystal structure are now are now replaced with two broad peaks, with the second peak exhibiting two sub peaks located at $\frac{r}{r_0} \approx 1.65$ and 1.9. Following this split double peak, the oscillations of the RDF quickly approaches 1.

The presence and form of the split second peak gives valuable information about the structure of these foam packings. Bernal *et al.*, in the study of the structure of liquids using a hard sphere model, determined that a random packing of spheres has associated with it a unique RDF [32, 33]. In particular, it was found that the random sphere packing RDF has a split second peak, with two sub-peaks located at $\frac{r}{r_0} = \sqrt{3}$ and 2. This splitting of the second peak is a result of local arrangements of the first, second and third nearest neighbours within the sphere packings. It is found that the first nearest neighbour will reside at a position of $\frac{r}{r_0} = 1$ corresponding to particles directly in contact with the central sphere being examined. The next two peaks, at $\frac{r}{r_0} = \sqrt{3}$ and 2 correspond to second and third nearest neighbours within the packing, as shown in Fig.3.15. Following these local arrangements, the radial distribution quickly approaches 1, indicating uncorrelated sphere positions. Since the original work of Bernal, this particular functional form of the RDF for disordered sphere packings has been verified in various experimental systems, particularly the large hard-sphere systems examined by Aste *et. al.*. Through the use of X-ray tomography, they examined several packing of 150,000 hard-sphere beads of diameter 1.00 ± 0.05 *mm*. Such RDF have also been found in the study of the structure of glasses [61].

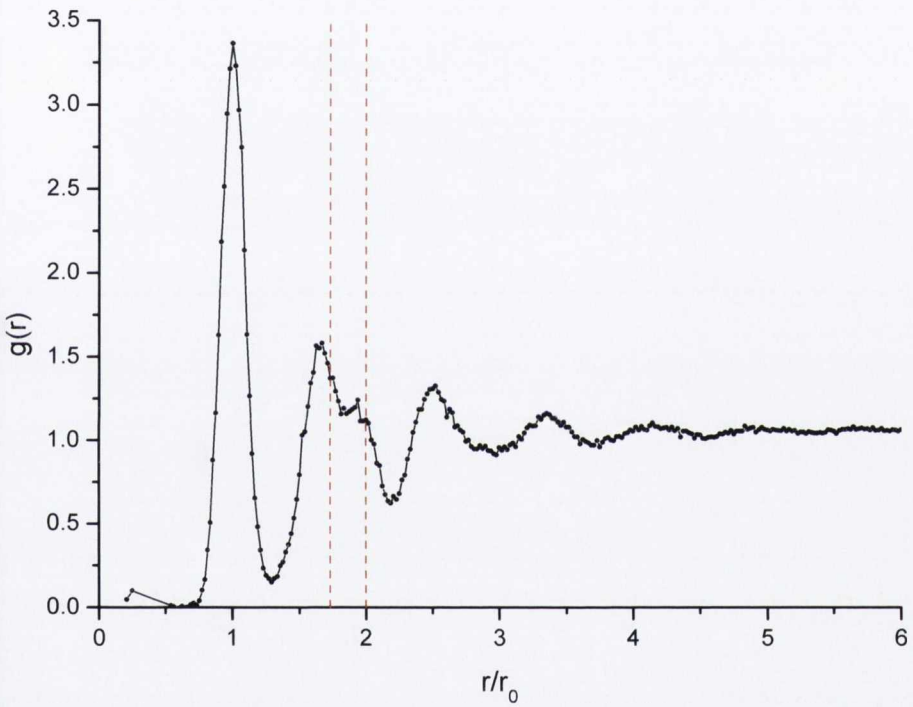

Figure 3.14: Plot of the radial distribution function for the thick foam sample shown in Fig. 3.10. The experimental curve is shown as a continuous black line, while the positions of the local arrangements associated with a Bernal packing of spheres is shown in red. Note the splitting of the second peak of the distribution at 1.65 and 2.

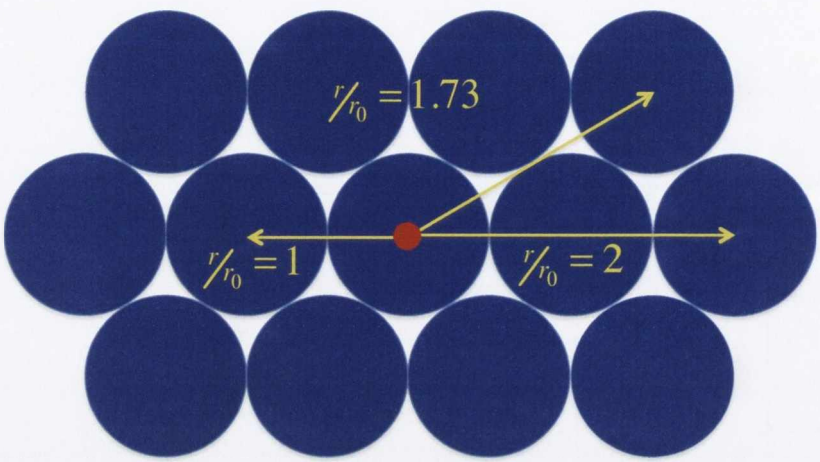

Figure 3.15: A two-dimensional illustration of the local arrangements which lead to the split second peak in the RDF of a random packing of hard spheres. It is seen that the three closest spheres to any sphere closest are located at distances $\frac{r}{r_0} = 1,1.73$ and 2.0

The positions of the split-second peaks associated with hard sphere packings are overplotted using red-dashed lines on the foam experimental data in Fig.3.14. It is seen that the foam peaks reside near to their hard-sphere counterparts. Several differences are seen to occur between the hard-sphere and foam experiments. Firstly, it is seen the experimental peaks of the foam experiments are not as sharp as those expected for hard spheres. The form of the RDF is also seen to differ slightly. In the hard-sphere experiments, the slope of $g(r)$ gradually increase to a local maximum at $g(r) = \sqrt{3}$, before progressing smoothly to the next local maximum at $r = 2$, after which a shard decrease in $g(r)$ is seen [45]. In our foam experiments such a sharp decrease in $g(r)$ is not observed. In addition, it is found that the relative heights of the two split-peaks of the RDF have been inverted with respect to the hard sphere case i.e, for the hard sphere case $g(\sqrt{3}) < g(2)$ while the bubble experiments show $g(\sqrt{3}) > g(2)$.

It has also been previously reported that a power law relationship of the form $g(r) = c_0|r - r_0|^\alpha$ exists in the range $1 < \frac{r}{r_0} < 1.3$ [45]. Aste et al. reported values of α between 0.25 and 0.45, depending on the packing fraction of the system being examined. Fig. 3.16 shows that our data is not well described by such a power law relationship. The same power law to the experimental data for our disordered bubble packing.

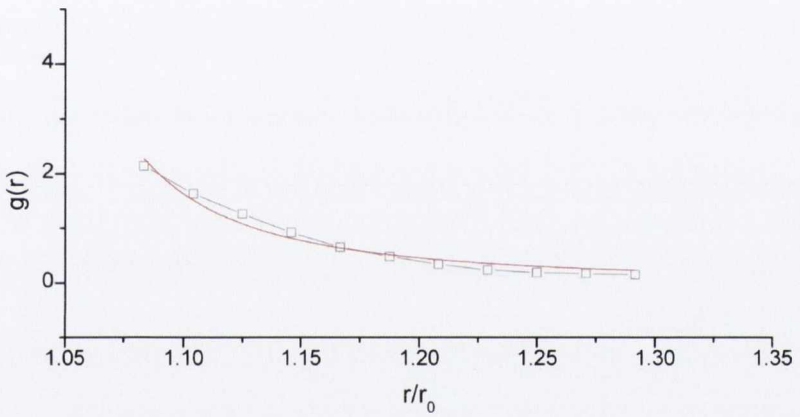

Figure 3.16: A power law of the form $g(r) = c_0|r - r_0|^\alpha$ fitted to the RDF of the thick foam sample. The best fit produced a power law exponent c = 1.8, however it is clearly seen that this is a poor fit to the data.

The discrepancy between the hard sphere and foam RDF are a result of two main differences between the two systems. The relative small sample size of the bubble experiment (20,000 bubbles vs 150,000 hard spheres of Aste *et al*) it is likely to result in the broadening of the radial distribution function of the foam data. Also, the finite compressibility of the bubbles of the foam sample will lead to a lack of a sharp changes in $g(r)$ and the inversion of the relative heights of the two peaks of the split second peak.

In spite of these differences, we believe this split second peak is the most convincing experimental evidence that a foam may be well described as a

random packing of spheres. This assumption has been the basis of many simulations of foams, where the energy-minimised Voronoi tessellation of a random packing of spheres is taken as the initial system configuration.

3.3 Temporal evolution of monodisperse foam sample

In order to determine the effect of coarsening on the foam samples that we were investigating using X-ray tomography, a test sample composed of roughly 16,000 bubbles was produced and imaged once per day over seven days, so that the evolution of the bubble size distribution could be determined. This was a requirement, as we were unable to find sufficient information regarding the effect of perfluorohexane on the coarsening of a monodisperse foam.

During the evolution of the foam sample, it was found that the bubble diameter distribution of the sample did not change dramatically. On each day of the experiment, the dispersity of the sample remained below the threshold of 5% which, in experiment, defines the distribution as monodisperse [5]. However, it was found that the internal structure of the foam sample changed significantly over the seven day of the experiment.

3.3.1 Experimental Method

A monodisperse foam was produced as described in section 2.3.1 and placed into a cubic container as shown in Fig.B.1. The container was filled with roughly 15000 bubbles.

The filled container was sealed with a glass plate and affixed to a cylindrical plinth for the duration of the experiment. The foam was imaged using X-ray tomography as described in section 2.3.2. The sample was imaged at the same time each day. Between images, the sample was removed from the

tomographic device and stored in a secure location.

Following the successful imaging of the sample over the seven days of the experiment, the image data was processed and segmented as described in section 2.3.3. The data was then analysed as described below.

3.3.2 Results

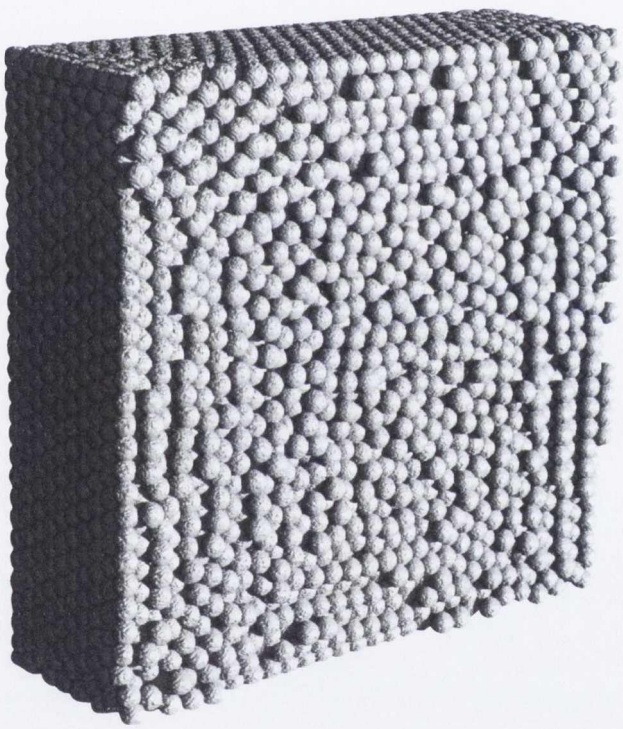

Figure 3.17: Visualisation of the foam used to examine the temporal evolution of such samples on the first day of the experiment. The image shows the foam-liquid interface of the sample. The foam, composed of 15,000 bubbles of average diameter $795 \pm 40\ \mu m$ is seen to have regions of hexagonal order near the sample boundary, while the central region is lacking such a structure.

Fig.3.17 shows a 3D representation of the foam sample on the first day of the experiment. The sample has ordered into a structure 10 layers deep. Around the borders and near the corners of the sample, the structure is seen to be hexagonally arranged, while no such ordering is seen near the center of the foam sample.

The distribution of bubble sizes were calculated for each of the seven days of the experiment and is shown in Fig.3.18. These distributions were fitted to a Gaussian distributions, the resulting average bubble diameter distribution and second moment of which are plotted in Fig.3.19.

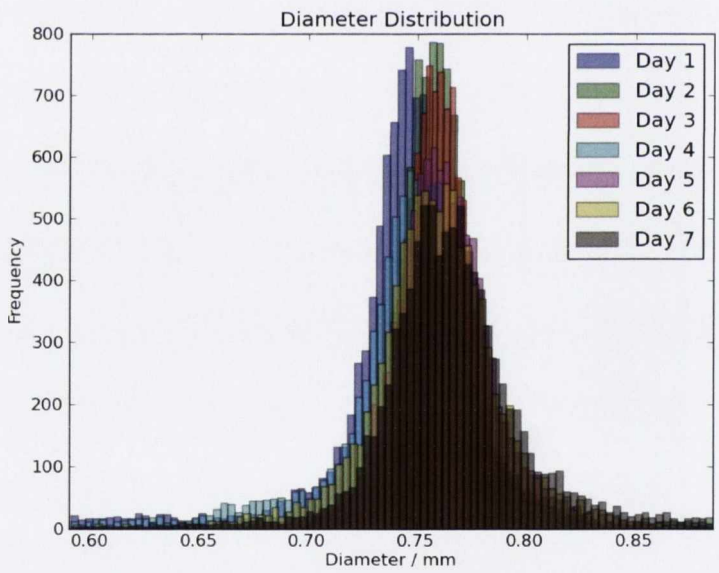

Figure 3.18: Overplot of the histogram data for the seven days of the experiment. It is seen that the histograms broaden slightly over the course of the experiment, corresponding to a slight coarsening of the foam. Due to the use of PFH gas, however, such coarsening was limited and the sample could be considered monodisperse throughout its lifetime.

It is seen that the average bubble diameter increases during the lifetime of the experiments, rising from 795 μm to 810 μm. This is due to the unavoidable coarsening within the sample [49]. However, due to the addition of Perfluorohexane to the Nitrogen gas, the coarsening rate of the foam is significantly reduced when compared to that of a pure nitrogen foam [6]. In particular, it is noted that the dispersity of the foam remains less than 5% over the seven days of the experiment. This means that the foam may be considered as monodisperse throughout its lifetime.

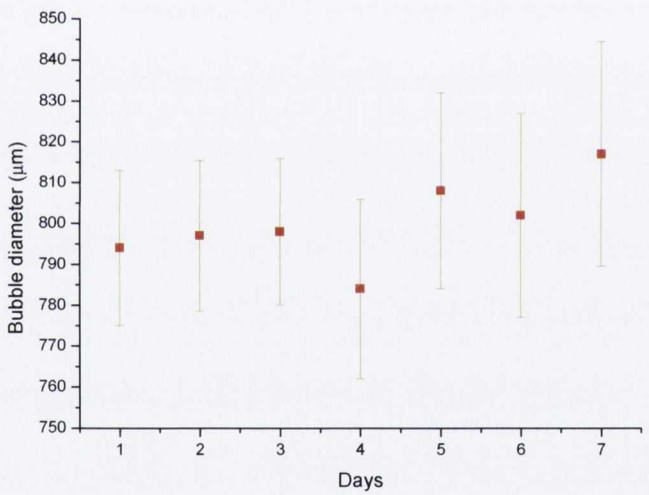

Figure 3.19: The average bubble diameter, with standard deviation of the bubble diameter shown as error bars, plotted over the lifetime of the experiment. It is seen that, although the average bubble diameter is increasing over the lifetime of the experiment, the ratio of the standard deviation to average bubble diameter remains less than 5%, indicating that the foam remains monodisperse throughout its lifetime.

However, we found that several interesting structural changes occurred

within the sample during the seven days of the experiment. Such changes are best illustrated by two-dimensional plots of the XY center positions of the bubbles over the seven days. This corresponds to a collapse of the z-axis of a three-dimensional plot of the bubble centre positions. Such a plot of center positions is seen in Fig.3.20.

The sample was imaged three hours after production on the first day of the experiment. The first day of the experiment shows the bubble centres are arranged into regular lines close to the boundary of the sample. Such regular arrangement of bubbles are seen to extend up to 6 bubble diameters away from the boundary of the sample. In the center of the sample, however, no such ordering is observed. This indicated that crystalline ordering is present close to the boundary walls, while the center of the sample is possibly disordered. On the second day of the experiment, this boundary ordering is seen to extend more prominently into the central region of the foam sample.

On the third day of the experiment, the ordering of the central region has been significantly diminished. In addition, the extent of the boundary region has been reduced when compared to the first day, the order regions extending to a maximum 3 bubble diameters from the container wall. We believe this is due to a "bumping" of the sample on the third day of the experiment. This disturbance, we believe, disordered the ordered sections of the foam sample.

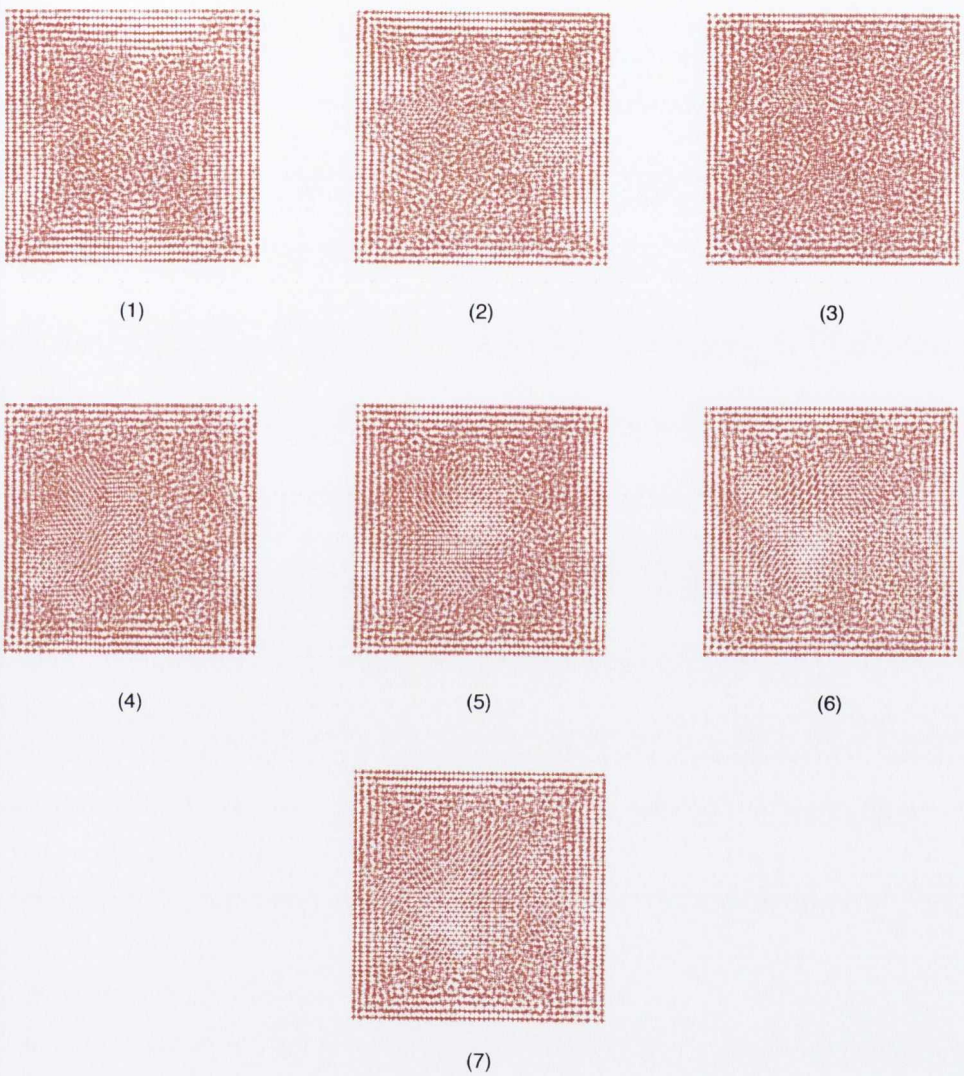

Figure 3.20: Plot of the XY coordinates of the sample over the seven days of the experiment, labelled by the day number. On the first day of the experiment, the bubble are seen to form regular rows of particles close to the container walls. The bulk of the sample shows no such ordering. Over the seven days of the experiment is seen that this central region of the foam sample becomes ordered. This is demonstrated through the onset of a regular pattern in the center of the sample.

For the next four days of the experiment, the sample was not again disturbed. The ordering behaviour that was observed to occur during the first two days of the experiment was seen to progress during the remaining days of the experiment. In addition to the extension of the boundary ordered regions into the bulk, it is seen that separate regions of order spontaneously occur within the foam bulk on the fifth, sixth and seventh days of the experiment. No additional imaging time was available to continue the experiment past the seventh day of the experiment.

In order to more accurately examine the ordering behaviour, we calculated several metrics of order for the sample, including the contact number, the translational order parameter, the bond orientational order parameter and the packing fraction of the sample.

3.3.2.1 Coordination number

To quantify the ordering within the sample, the coordination number distribution over the seven days of the experiment were calculated and overplotted. The results of such a calculation are shown in Fig.3.21.

On the first day of the experiment, shown in red, a wide distribution of contacts is seen to occur within the sample. On the second day of the experiment, shown in green, this wide distribution begins to show a peak at n=12. On the third day of the experiment, the initial broad distribution of contacts within the sample is seen to re-occur. This corresponds to the disturbance of the experiment which occurred on the third day of the experiment, as has been previously discussed. From the third day of the experiment onwards, no further disturbance of the sample occurred. During this time, the contact number distribution is seen to evolve into a two-peaked distribution centred around n=9 and n=12. As we have previously discussed for the thin foam sample, this corresponds to hexagonal ordering along the boundary of the sample and within the foam bulk. While the height of the $n = 12$ peak is seen to increase steadily over the last 4 days of the experiment, the n=9

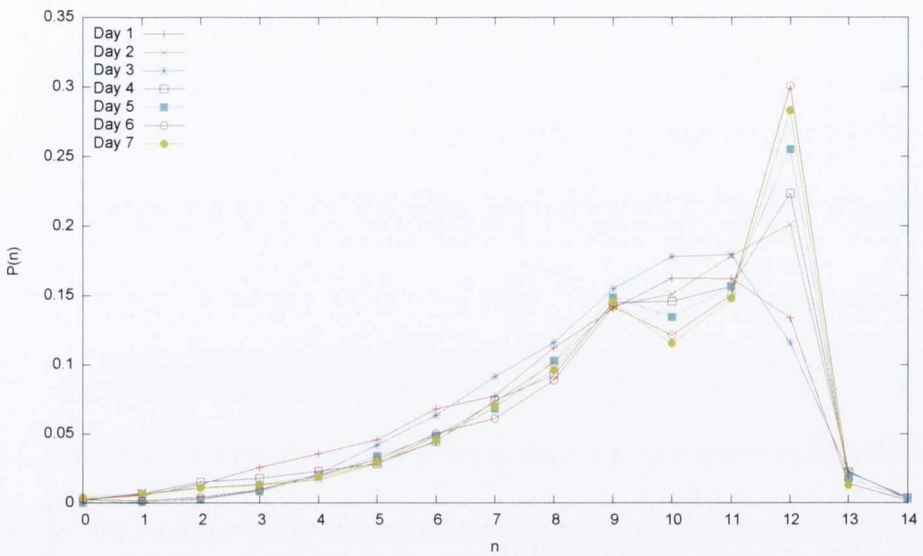

Figure 3.21: Variation of the contact number distribution over the lifetime of the experiment. The number of contacts n is plotted against the probability of that contact within the sample $P(n)$. Over the course of the experiment, the initial wide distribution is seen to resolve itself into a two-peaked distribution centred at n=9 and n=12. These peaks correspond to hexagonal ordering occurring along the foam boundary and within the foam bulk.

peak is seen to remain at a constant value throughout the lifetime of the experiment. This implies that the ordering of bubbles around the boundary of the sample does not change - the increase in the order within the sample occurs within the foam bulk. This indicates that he disordered central region of the foam is progressing towards a more ordered state.

3.3.2.2 Translational order parameter evolution

Fig.3.22 shows the translational order parameter G as calculated for the sample over the seven days of the experiment. It is seen that the order parameter decreases over the first two days, before dramatically increasing

on the third day. This corresponds to the previously discussed disturbance of the sample on the third day. During the next four days, G is seen to decrease. This corresponds to the ordering of the sample which was observed from the XY center positions shown in Fig.3.20.

Over the last four days of the experiment, G decays roughly exponentially, $G(t) = 0.45e^{-0.94t} + 0.018$, seen as the solid line in Fig.3.22.

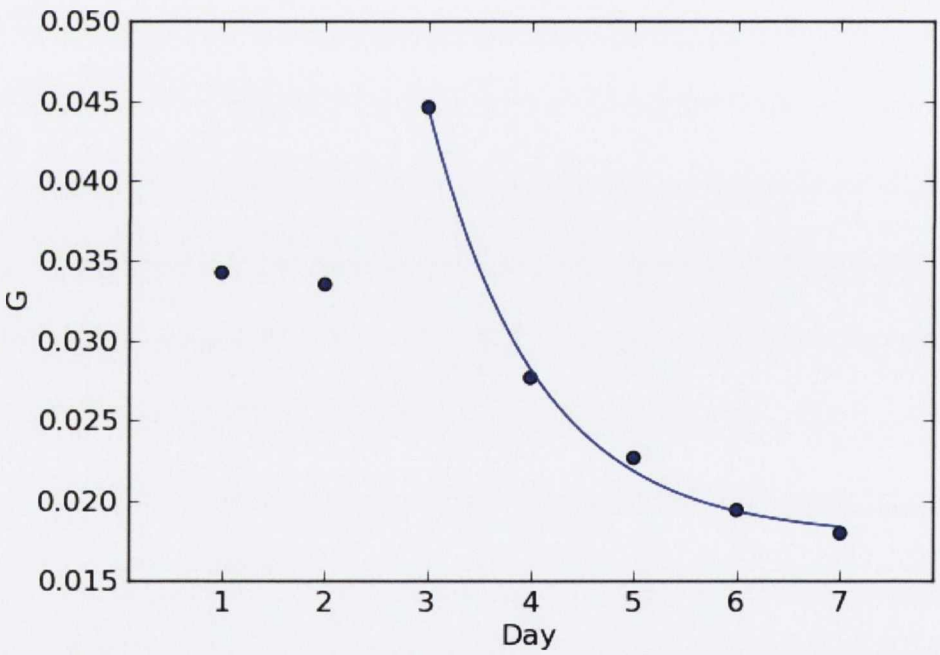

Figure 3.22: Graph showing the variation of the translational order parameter G over the course of the seven days of the experiment. It is seen that G decreases during the first two days of the experiment, before dramatically increasing on the third day due to the disturbance of the sample. This is followed by a smooth decrease in G, fitted to an exponential with an offset.

3.3.2.3 Bond orientational order coefficient

While the calculation of the translational order parameter shows that the sample is progressing towards a more ordered state, it does not provide information about local configuration of bubbles. In our pursuit of this local information, we calculated the Bond Orientational Order Parameter (BOOP) for each bubble within the sample.

The BOOP or Steinhardt order parameter is a measure of the rotational order within a sample [61]. Although there exists several methods by which this rotational symmetry may be classified, it is found that Steinhardt's characterisation, developed to investigate the onset of ordering within glasses, has proven the most useful in a variety of simulations and experiments [62, 45]. In particular, it has proven useful in determining order within colloidal systems and granular media and is used to determine the onset of phase transitions in these systems.

The bond orientation order parameter is based upon the association of a spherical harmonic $Q_{ml} = Y_l^m(\phi_{ij}, \theta_{ij})$ with each "bond" within the system. A bond, for the BOOP case, is defined as a vector $\vec{r_{ij}}$ joining the center positions of neighbouring objects i and j. ϕ_{ij} and θ_{ij} are the polar and azimuthal angles of this bond with respect to a spherical coordinate system. For the bond orientational order parameter, two particles are considered neighbours if the distance between the centres of two particles $|\vec{r_{ij}}|$ is less than 1.3 $\bar{d}$ where $\bar{d}$ is the average particle diameter, as demonstrated in Fig.3.23 (This corresponds to the position of the first minimum of the RDF function for a disordered packing [61]). Other definitions used to define the neighbourhood of a particle are based on the Voronoi tessellation, or a weighted Voronoi tessellation, of the center positions of the lattice. The faces of the resulting tessellation point to neighbouring particles within the sample. It is found, however, that changes in the definition of the neighbourhood does not produce significant differences in the BOOP parameters calculated for the same packing [63].

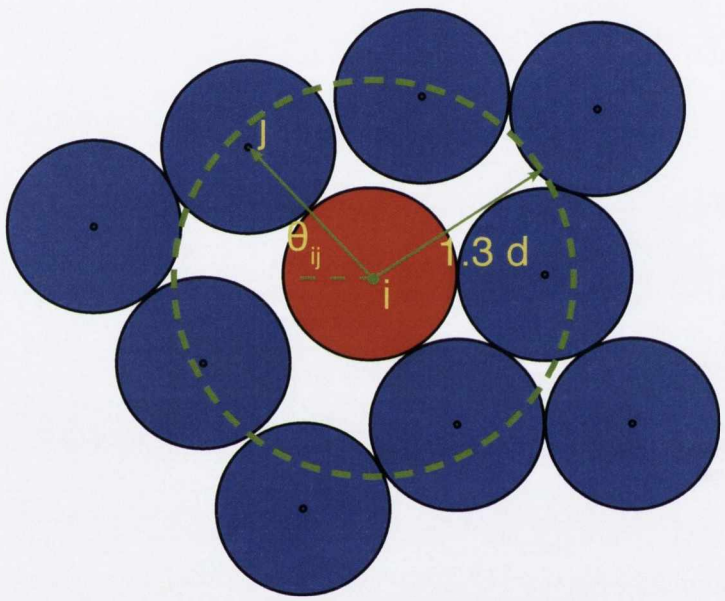

Figure 3.23: A 2D illustration showing the bond associated between the packing of two particles i and j. Only those particles whose centers lie within the disc of radius $1.3\bar{d}$ are considered nearest neighbours within the packing. (r, θ_{ij}) are the polar coordinates of neighbouring particles with respect to an arbitrary reference frame. For a three dimensional system, the azimuthal angle ϕ_{ij} between neighbouring particles must also be included.

So as to guarantee the directional invariance of the BOOP parameter, only even spherical harmonics (l = 0,2,4,6...) are considered. For symmetric packings the first nonzero results are obtained for l=4 and l=6. Spherical harmonics with l=4 are particularly sensitive to hcp order and crystals with cubic symmetry, while l=6 is sensitive to icosahedral symmetry [61]. For this reason, only the fourth and sixth spherical harmonics are considered. It is found that the value associated to a particular bond through the use of these spherical harmonics is dependent on the frame of reference chosen. To ensure the invariance of the order parameter associated with a particular bond, frame-independent averages of spherical harmonics need be considered. For the 4^{th} and 6^{th} spherical harmonics, these averages are defined as,

$$Q_4 = \left(\frac{4\pi}{13} \sum_{m=-4}^{4} \frac{1}{N} \sum_{i=1}^{N} \frac{1}{n_i} \left| \sum_{j=1}^{n_i} Y_4^m(\phi_{ij}, \theta_{ij}) \right|^2 \right)^{\frac{1}{2}} \tag{3.1}$$

$$Q_6 = \left(\frac{4\pi}{13} \sum_{m=-6}^{6} \frac{1}{N} \sum_{i=1}^{N} \frac{1}{n_i} \left| \sum_{j=1}^{n_i} Y_6^m(\phi_{ij}, \theta_{ij}) \right|^2 \right)^{\frac{1}{2}} \tag{3.2}$$

where ϕ_{ij} and θ_{ij} are the polar and azimuthal angles associated with the particular bond within the system, Y_l^m is the l^{th} spherical harmonic, n_i is the number of nearest neighbours of the particle being considered and N is the total number of particles within the system [61]. $Y_l^m(\phi_{ij}, \theta_{ij})$ is the spherical harmonic, defined as

$$Y_l^m(\phi_{ij}, \theta_{ij}) = \sqrt{\frac{2l+1}{4\pi} \frac{(l-6)!}{(l+6)!}} e^{im\phi_{ij}} P_l^m(cos\theta_{ij}) \tag{3.3}$$

where $P_l^m(cos\theta_{ij})$ are the Legendre polynomials. Each crystal structure will have associated with it a unique set of Q_4 and Q_6 values with which it may be identified. Examples of Q_4 and Q_6 BOOP parameters associated with a variety of crystal structures are listed in table 3.1. If the system

studied exhibits no particular ordered structure, a wide distribution of BOOP parameters is seen to occur, as shown in Fig.3.24.

Table 3.1: BOOP parameters of several common structures.

Structure	Q_4	Q_6
fcc	0.19094	0.57252
hcp	0.097722	0.48476
Icosahedral	0	0.66332
Liquid	0	0

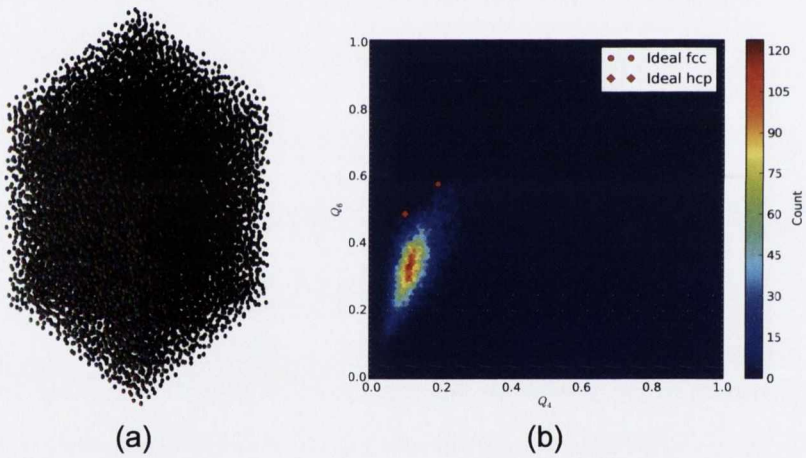

Figure 3.24: BOOP analysis of a disordered sphere packing produced using a computer simulation. (a) Simulation of a disorder packing produced using a standard conjugate gradient method to minimise the system energy [64]. (b) a wide distribution of Q_4 and Q_6 parameters are seen to characterise such a disordered structure.

We produced histograms of Q_4 and Q_6 parameters for the positional data of each bubble within the sample over the lifetime of the experiment. To

compute the BOOP parameter, we used the C algorithm produced by Wang *et al.* [65]. Examples of such histograms are shown in Fig.3.25 and Fig.3.26. In these plots there occurs several peaks in the experimental data at positions associated with fcc and hcp ordering. Note however, in Fig.3.25, there does not exist a peak in the experimental data which corresponds to the onset of hcp ordering. This is a result of Q_4 and Q_6 being sensitive to different crystal symmetries [61].

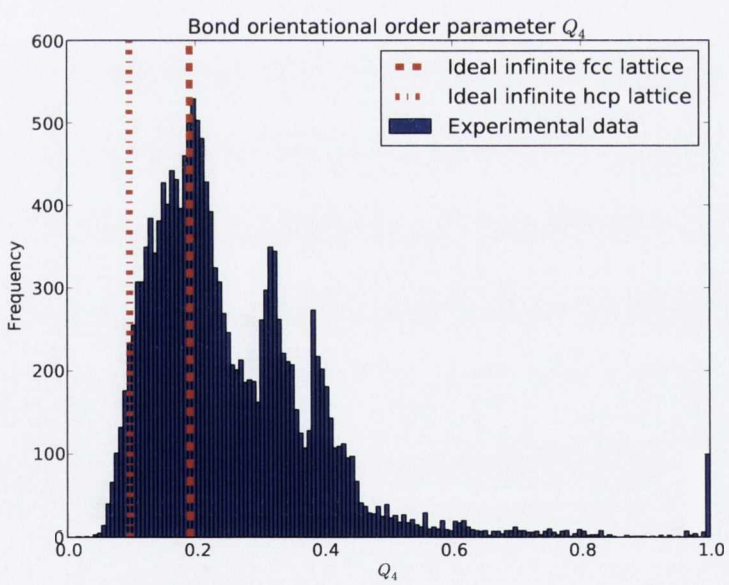

Figure 3.25: Example of the calculation of Q_4 for an experimental packing (day 1 of the lifetime experiment). Note that there exists no peak corresponding to hcp ordering within the Q_4 distribution.

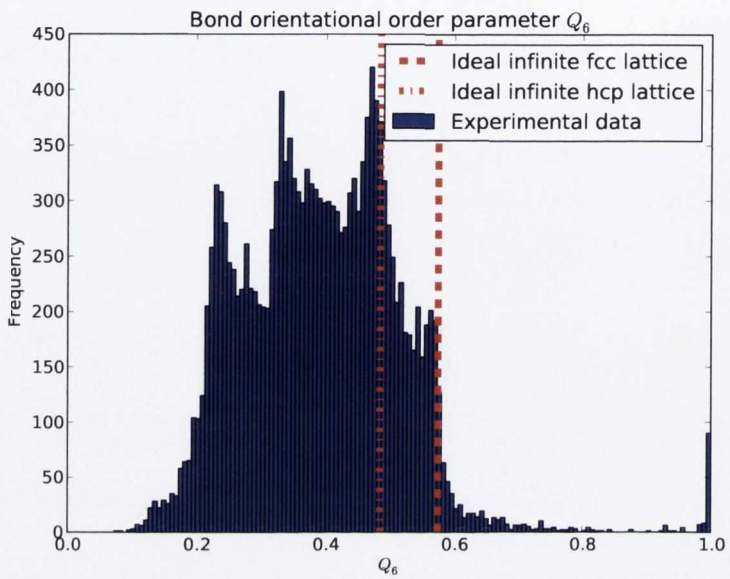

Figure 3.26: Example of the calculation of Q_6 for an experimental packing (day 1 of the lifetime experiment).

To overcome these problems associated with the different sensitivities of the BOOP parameters, two-dimensional histograms of both the Q_4 and Q_6 order parameters may be produced. Such a plot for the first day data is seen in Fig. 3.27. The bubble center positional data was analysed to calculate the BOOP for each particle within the packing. Local regions of crystallisation, as well as amorphous regions, could then be identified and classified. For our purposes, we identified a region as belonging to a particular crystallographic group if the bubble examined lay within ± 0.1 of the Q_4 and Q_6 values associated with the ideal case of such a lattice. Such bounds were found to correctly identify crystalline regions when compared to a visual inspection of the sample.

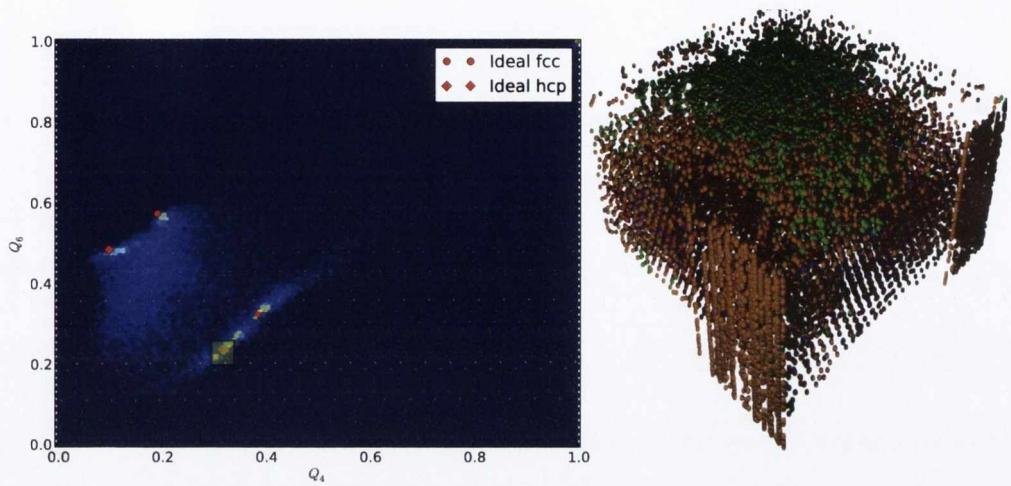

Figure 3.27: (a) graph of Q_4 against Q_6 for the first day of the experiment. It is noted that in addition to the peaks associated with fcc and hcp packings, there also exists a separate peak located at (0.30,0.22). To determine the reason for this separate peak, a visualisation of the sample was produced, shown in (b). Regions corresponding to the unidentified peak were coloured green.

It is seen that the BOOP data is composed of a series of peaks as well as a wide distribution of points. Most prominently within the data there exists two peaks located at (0.19,0.57) and (0.09,0.48). These peaks correspond to the formation of fcc and hcp regions of crystalline ordering within the sample. In addition to these peaked regions, in the region $0.2 < Q_4 < 0.4$ and $0.2 < Q_6 < 0.24$ a wide distribution of points is seen. These points correspond to the amorphous regions within the foam sample. This distribution is similar to the wide distribution reported for amorphous configurations within granular media [45].

It is noted that a separate peak exists at roughly (0.30,0.22). This region was not seen to correspond to any known crystal configuration. To determine

the origin of this peak, we produced a visualisation of the system in which points in space corresponding to this unknown region where coloured green (see Fig.3.27b). This analysis shows that the peak corresponds to linear chains of particle along the boundary and top of the sample. This is due to segmentation noise within the sample and was exclude from all further analysis. The remainder of our analysis is shown in Fig.3.28 and Fig.3.29 which show the evolution of the Q_4 and Q_6 order parameters, as well as a plot of the positions of bubble ordered locally into fcc configurations (shown in red) and hcp region (shown in blue).

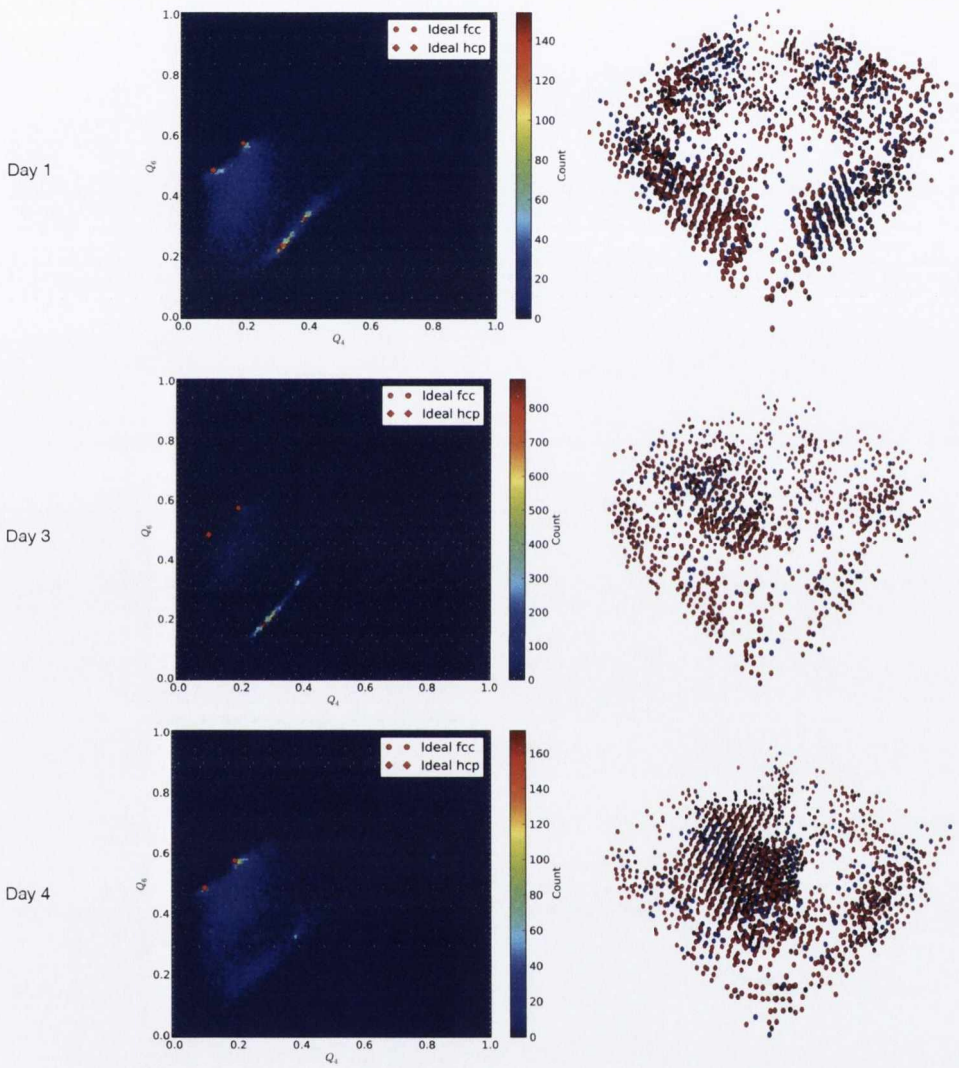

Figure 3.28: Figure showing the evolution of the Q_4 and Q_6 order parameters of the foam sample during the 1st, 3rd and 4th days of the experiment. In addition to the 2D histogram of the Q_4, Q_6 order parameters, a plot of the bubble center positions is also included. Those particles identified as existing in an fcc configuration are shown in red while hcp bubbles are shown in blue. Over the lifetime of the experiment, it is seen that the heights of the points associated with fcc and hcp ordering increas in time, while the regions associated with disordered spheres decreases in intensity.

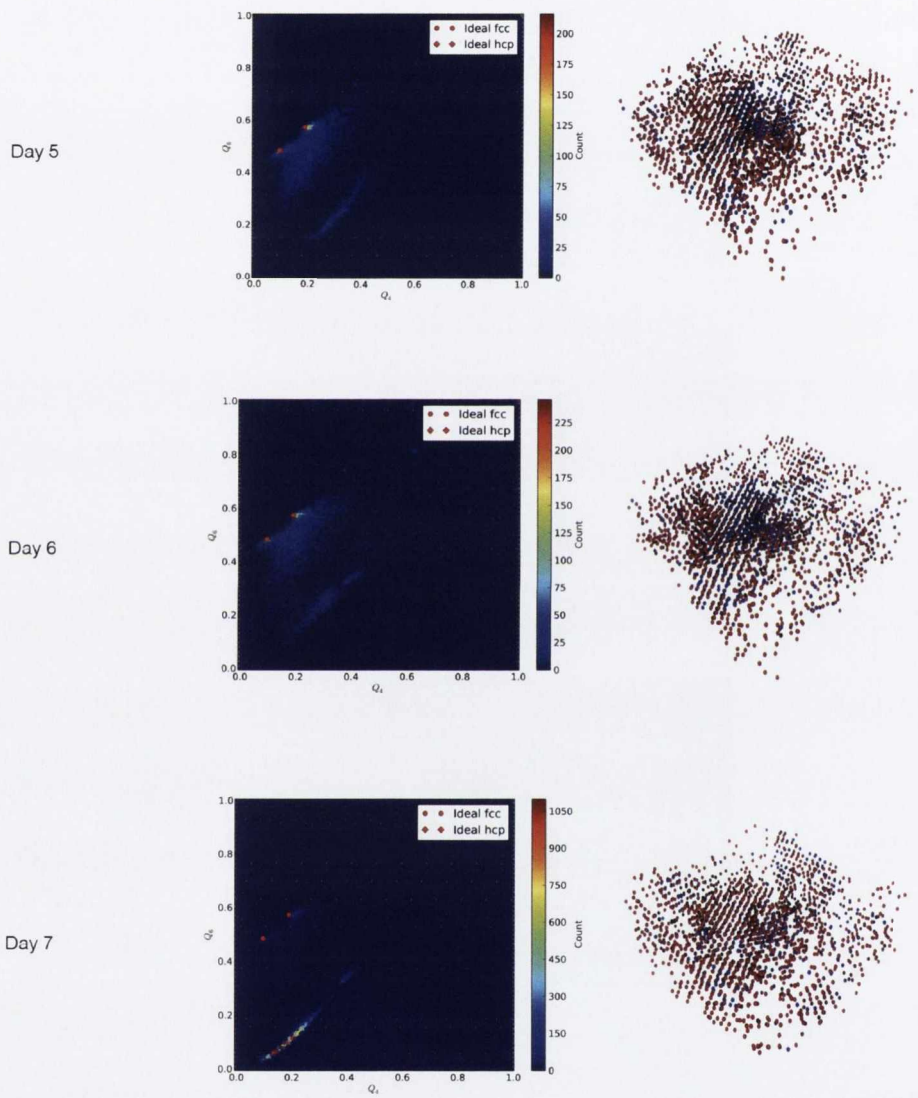

Figure 3.29: Figure showing the evolution of the Q_4 and Q_6 order parameters of the foam sample during the 5^{th}, 6^{th} and 7^{th} days of the experiment. In addition to the 2D histogram of the Q_4, Q_6 order parameters, a plot of the bubble center positions is also included. Those particles identified as existing in an fcc configuration are shown in red while hcp bubbles are shown in blue.

Throughout the lifetime of the experiment there is no clear divide between regions of fcc and hcp crystallisation. Instead, the two regions of crystallisation seem to coexist within the same regions of the foam sample. This suggests the formation of RHCP regions within the sample.

As the system evolved in time, it was seen that the Q_4, Q_6 distribution changes with time. The two peaks associated with fcc and hcp ordering increase in intensity, while the broad region of points associated with a disordered sphere packing is seen to decrease in extent. This corresponds to the increase in the ordered nature of the sample, which we have previously seen through the use of the translational order parameter G.

From our BOOP data, we calculated the ratio of the number of fcc ordered bubbles (N_{fcc}) and hcp bubbles (N_{hcp}) within the sample, the variation of which, over the seven days of the experiment, is shown in Fig.3.30.

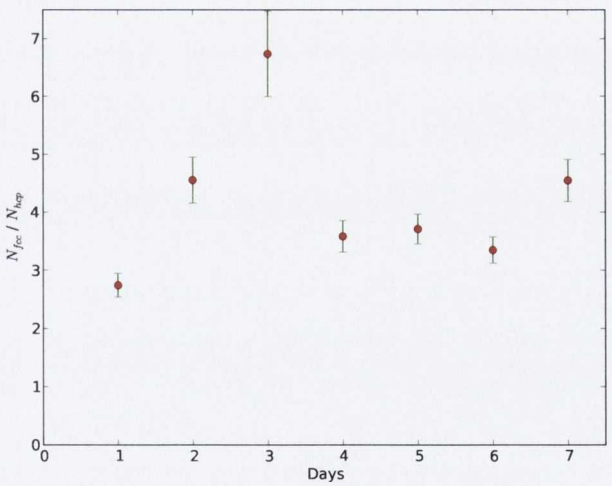

Figure 3.30: $\frac{N_{hcp}}{N_{fcc}}$ plotted over the seven days of the experiment. It is seen that the ratio remains above 1 for the lifetime of the experiment, indicating a preference for fcc crystallisation.

$\frac{N_{fcc}}{N_{hcp}}$ is seen to reside above a value of 1 for the entire lifetime of the experiment. This indicates a preference for fcc crystallisation throughout the foam lifetime. This is in keeping with recent theoretical work on the preference for fcc over hcp by Heitkam *et al.* [66]. They determined that linear arrangements of spheres present within an fcc lattice (e.g. along the [110] direction) which are absent within the hcp lattice make these structures mechanically more stable when formed under deposition of spheres. This results in a preference for fcc crystals within monodisperse bubble crystals.

3.3.2.4 Packing fraction

The packing fraction ϕ for our foam sample was calculated over the seven days of the experiment. We limited the calculation of ϕ, however, to the central region of the foam which is seen to be disordered on the first day of the experiment. In this manner, we might expect to observe a steady increase in packing fraction from the value associated with a random packing of spheres ϕ_{RCP} =0.64 to the value associated with hexagonally closed-packed structures of $\phi = 0.74$ on the seventh day of the experiment [13, 30].

The packing fraction was calculated for within a sphere of radius R centred within the sample. A spherical volume was chosen due to the ease by which those bubbles on the boundary of such a sphere may be accounted for. R was chosen such that the outer limit of the sphere did not intersect the ordered boundary regions of foam on the first day seen in Fig.3.20(1).

The packing fraction of the sample may be given by

$$\phi = \frac{\sum_{i=0}^{N} V(r_i, d_i)}{\frac{4}{3}\pi R^3} \tag{3.4}$$

where r_i is the radius of the i^{th} bubble, R is the test volume being examined, and d_i is the distance from the center of the test sphere to the center of the i^{th} bubble. When calculating ϕ using Eq.3.4, bubbles on the border of the test volume examined (i.e. $|R - r_i| < d_i < |R + r_i|$) must be taken into account.

To do this, we consider the intersecting volume of a sphere of radius R with a spherical bubble of radius r_i. Doing this, we may write $V(r_i, d_i)$ as

$$V(r_i, d_i) = \begin{cases} \frac{\pi(R+r-d)^2(d^2+2dr-3r^2+2dR+6rR-3R^2)}{12d} & |R-r_i| < d_i < |R+r_i| \\ \frac{4}{3}\pi r_i^3 & d_i < |R-r_i| \\ 0 & \text{otherwise} \end{cases} \tag{3.5}$$

Applying this formula allowed the packing fraction of the sample to be measured accurately while taking account of boundary bubbles. The results of this volume-fraction measurement are shown in Fig.3.31.

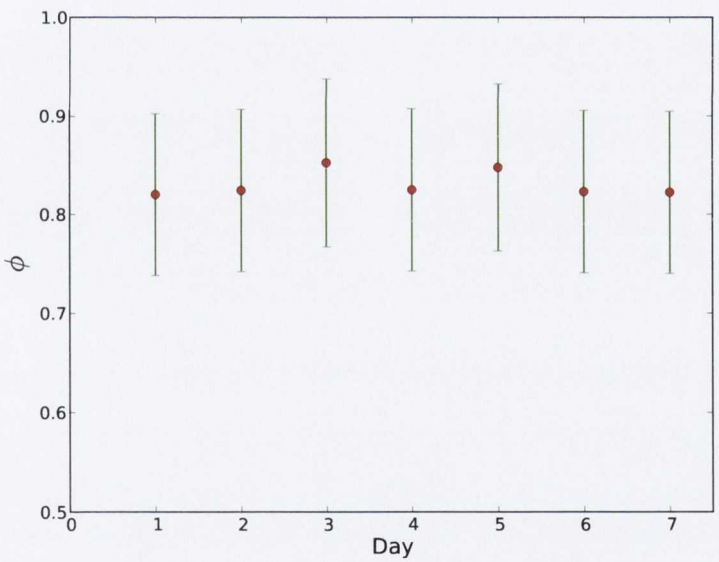

Figure 3.31: Variation of the packing fraction ϕ of the sample over the seven days of the experiment.

It is seen that the resulting volume fraction does not behave as one would expect for a similar system of hard spheres. Firstly, ϕ resides above the

maximum packing fraction associated with hard spheres of 0.74. In addition, no variation is seen to occur in ϕ over the seven days of the experiment - no complementary increase in ϕ is seen to occur as the order within the sample increases.

To verify this packing fraction calculation, and to obtain a more detailed understanding of the variation of the packing fraction within the foam sample, we decided to calculate the *Voronoi tessellation* of the sample.

3.3.2.5 Voronoi tessellation

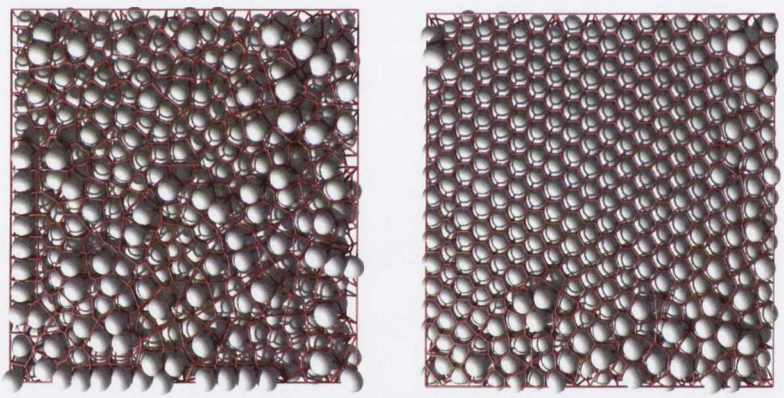

Figure 3.32: Visualisation of the Voronoi tessellation of the central region of the foam sample. (a) shows this region as imaged on the 1^{st} day while (b) shows the same section on the 7^{th} day. The bubbles are represented by spheres of the same radius while the red lattice shows the Voronoi tessellation . The images have been generated using *POV-Ray* [70].

The Voronoi tessellation is a method of dividing space based on the distribution of a number of points. More specifically, given a finite set of distinct points in space, the Voronoi tessellation associated with each point all regions

in space which are closest to it, as determined by some metric of distance [67]. For our purposes, we use the Euclidean distance metric. This tessellation may be used to accurately characterise the neighbourhood distribution of a packing, as well as providing a method by which the local packing fraction of a sample may be calculated [68]. To calculate the Voronoi tessellation of our sample we used the freely-available C++ libraries Voro++ [69].

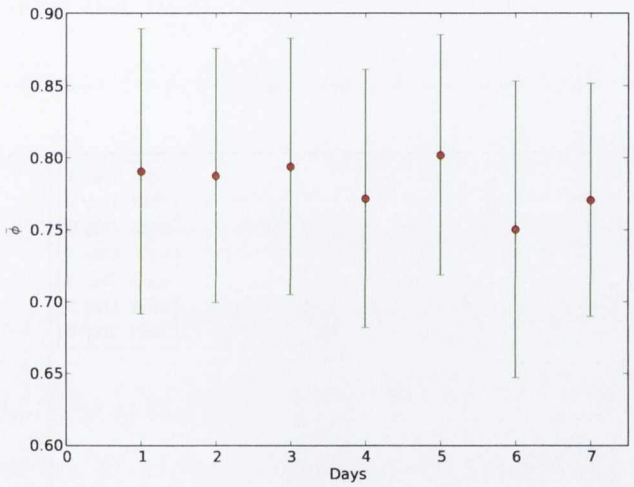

Figure 3.33: Variation of the average packing fraction $\bar{\phi}$ over the seven days of the experiment. This average is not seen to vary significantly over the lifetime of the experiment.

The Voronoi tessellation of a cubic section excised from the central region of the foam sample was calculated. This is the central region which appears disordered on the first day of the experiment, but approaches an ordered state on the last day of the experiment. Fig.3.32 shows a visualisation of the Voronoi tessellation of this internal section on the first and last day of the experiment.

The Voronoi tessellation may be used to calculate a local volume fraction for each bubble ϕ_i within the sample by diving the volume of the i^{th} particle by the volume of the corresponding i^{th} Voronoi cell. Fig.3.33 shows the average of these local packing fraction $\bar{\phi}$ for each day of the experiment. It is seen that, through this distinct measurement method, the packing fraction is again seen to reside above the expected values for both random and ordered sphere packings. In addition, no obvious variation of packing fraction occurs over the lifetime of the sample. Also, no change in the distribution of local packing fractions is seen to occur, see fig.3.34.

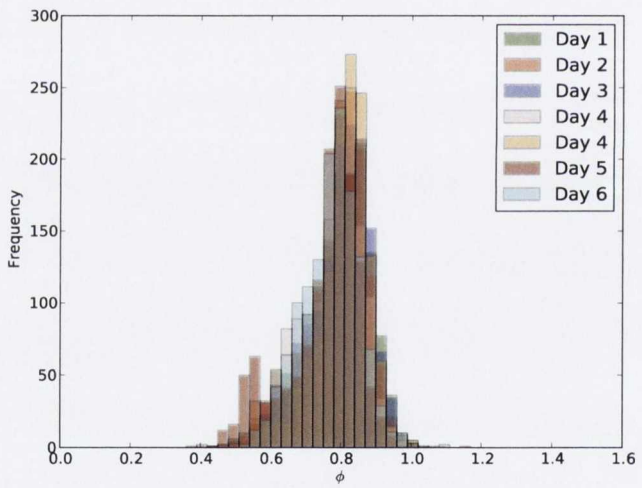

Figure 3.34: Distribution of the average packing fraction for each day of the experiment. The distribution is not seen to change significantly over the seven days of the experiment.

To verify that the Voronoi tessellation had been correctly implemented, we classified the order within the sample through the use of the isoperimetric quotient Q defined as

$$Q = \frac{36\pi V^2}{S^3} \tag{3.6}$$

where S and V are the surface area and volume of the Voronoi cell [71]. The Voronoi tessellation of each crystal structure has associated with it a particular Q value (see table 3.2).

Structure	Q
fcc	0.7405
hcp	0.7534
sc	0.5236
sphere	1

Table 3.2: Q factor for various crystal symmetries [71].

Fig.3.35 shows the distribution of the Q factor for the first, third and seventh day of the experiment. The peak corresponding to hexagonal ordering within the sample ≈ 0.74 increases over the lifetime of the experiment, showing the progressive ordering of the sample. Our analysis is not sensitive enough to distinguish between fcc and hcp using this order parameter. On the seventh day of the experiment, however, a second peak in the Q distribution is seen to occur at $Q = 0.67$. This sub-peak does not correspond to a Q value of any well-known crystal structure. To determine the sources of this extra peak, a xz plot of the bubble center position was produced (see Fig.3.36), the points in the plot coloured to correspond to particular Q factor.

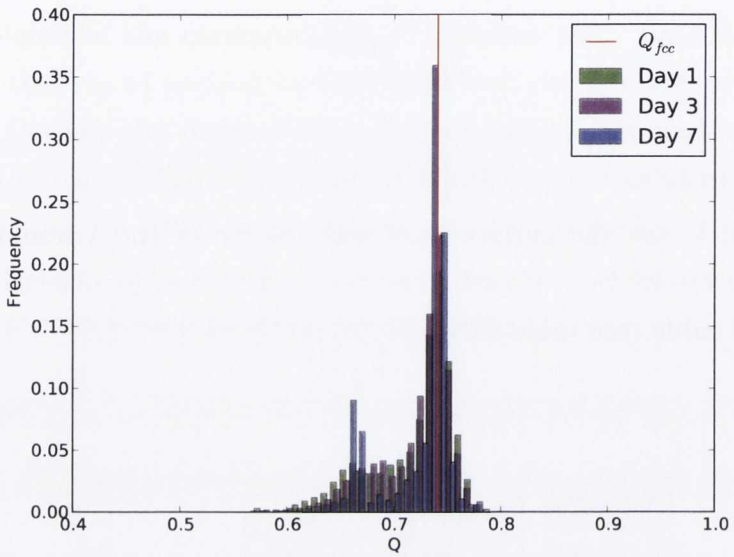

Figure 3.35: Distribution of the Q factor for the first, third and seventh day of the experiment.

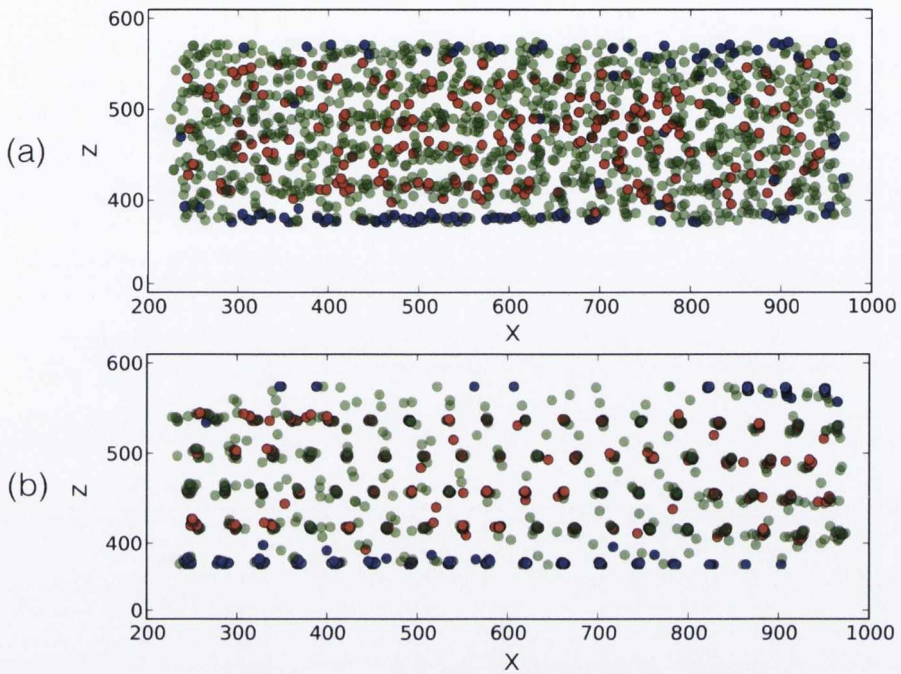

Figure 3.36: Xz plot of the center positions of the bubbles within the excised central section of the foam on (a) the first and (b) the last day of the experiment. Those regions corresponding to hexagonally closed packed regions were coloured red, those regions corresponding to the peak at $Q = 0.68$ are coloured blue, while those regions corresponding to other Q values are coloured green.

It is seen that the peak at $Q = 0.68$ corresponds to bubbles at the top and bottom of this excised foam sample. These bubbles are most likely hexagonally ordered bubbles whose Voronoi cells have been affected by the boundary condition imposed.

The results of the isoperimetric quotient analysis of the Voronoi sample correctly identified regions of hexagonal ordering within the sample. We therefore conclude that the Voronoi tessellation has been correctly imple-

mented for the sample. The unexpected results of the packing fraction analysis, however, is still unexplained. To determine the cause of the unusually high packing fraction, the variation of the packing fraction of the individual Voronoi cells was analysed for each structure. In particular, the variation of the packing fraction as a function of vertical height within the excised foam structure was analysed. The result of this analysis is shown in Fig.3.37. The individual Voronoi cell volumes are shown in red, while the average Voronoi cell packing-fraction is shown with cyan diamonds.

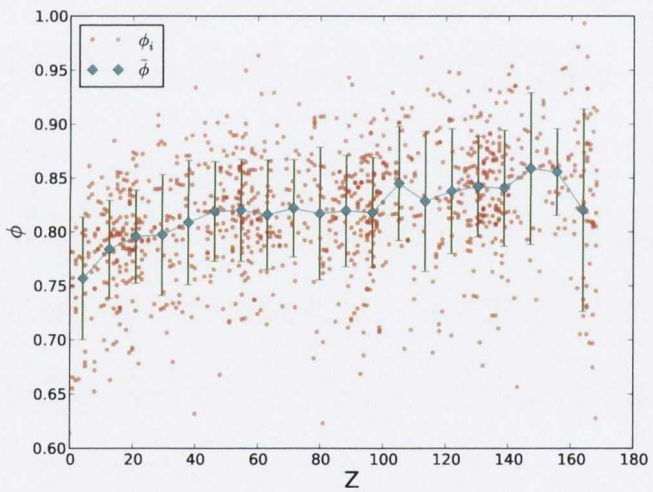

Figure 3.37: Plot of the variation of the average packing fraction $\bar{\phi}$ as a function of height Z for the third day of the experiment. The packing fraction for each Voronoi cell ϕ_i is shown in red. It is seen that the packing fraction increases as the distance from the bottom of the section (at $Z = 0$) increases.

While the individual packing fraction varies significantly ($0.60 \leq \phi \leq 1.00$), it is seen that the average packing fraction increases steadily with height within the sample. The onset of ordering within the sample produces

a banding of the Voronoi packing fraction data as the bubbles arrange into parallel planes (see Fig.3.38). This leads to difficulty in calculating the average packing fraction as a function of height within the sample.

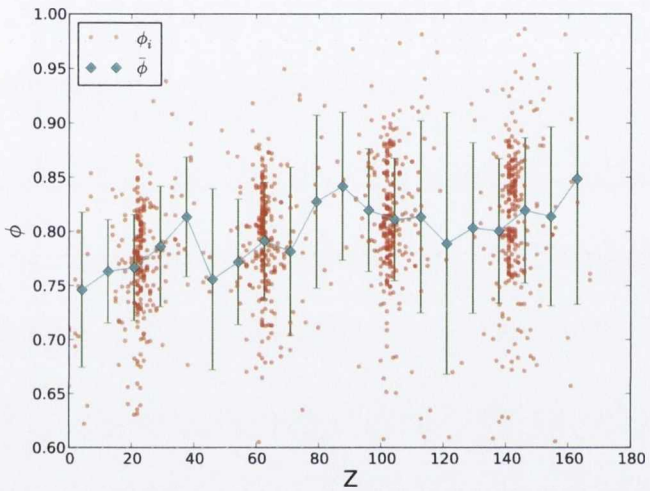

Figure 3.38: Plot of the variation of the average packing fraction $\bar{\phi}$ as a function of height Z for the seventh day of the experiment. The packing fraction for each Voronoi cell ϕ_i is shown in red. It is seen that the packing fraction increases as the distance from the bottom of the section (at $Z = 0$) increases. Note the grouping of data indicates the onset of ordering within the sample. This leads to a difficulty in calculating the packing fraction between ordered planes of bubbles.

We repeated this analysis for each day of the experiment, the resulting variation of the average packing fraction as a function of height is plotted for each day of the experiment in Fig.3.39.

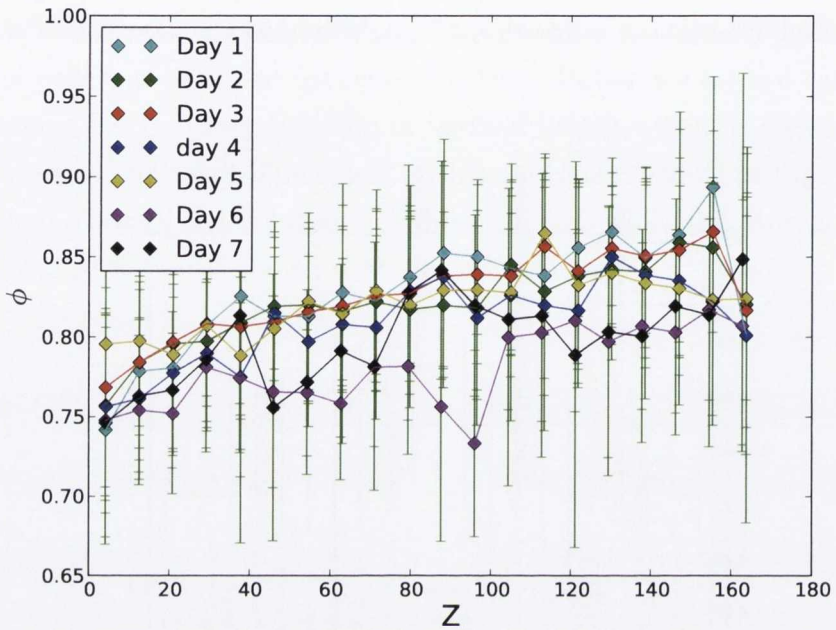

Figure 3.39: Variation of the average packing fraction within the foam sample as a function of height. In general, each day of the experiment shows the same increasing trend in the packing fractions.

On each day, the average packing fraction is seen to follow the same general trend, increasing with height within the sample. ϕ is seen to be relatively constant for a given height throughout the lifetime of the sample, indicating that the transition from a disordered to a ordered state does not effect the packing action of the sample. This behaviour is due to the compressibility of the bubbles being used in experiment. The finite compressibility of these bubbles allow them to achieve a packing fraction higher that the upper bound of of 0.74 associated with hard spheres. The packing fraction increases as a function of height within the sample due to the action of underlying foam layers. For a given layer within the foam, the buoyancy force of the underly-

ing foam layers forces bubbles of upper layers closer together. This has the effect of increasing the packing fraction of these higher foam layers, as seen in experiment.

3.4 Fcc-bcc transition

So far, our experiments have focused on a three-dimensional characterisation of foams within the wet-foam limit where an fcc packing of bubbles is seen to occur. As we have seen, however, monodisperse foams may spontaneously crystallise into both fcc and bcc crystals, depending on their liquid fraction [5]. These configurations correspond to the most efficient packing of spheres (fcc structure in the wet limit) and one of the most efficient partitioning of space (bcc lattice in the dry limit).

Foams provide a unique opportunity to study the continuous change between these densely packed structures as a function of liquid fraction. By varying the osmotic pressure of a monodisperse foam, Hohler *et. al.* successfully studied the nature of this transition, carefully observing the structural re-arrangements that must occur between an fcc and a bcc foam [5].

Their study, however, involved the optical characterisation of foam structure within a cylindrical geometry. Such a study is limited to surface layers. In addition, a cylindrical boundary condition is not commensurate with the symmetry of a bcc lattice which leads, inevitably , to defects within the crystal. In order to overcome these problems, we aimed to investigate the fcc to bcc foam transition using X-ray tomography.

Our experiment involved filling a rectangular container of internal dimensions 20mm x 20mm x 80mm (schematic shown in B.6). Approximately 70,000 bubbles of average diameter 700 μm were loaded into our container. The relative height of this container was such that gravitational drainage would produce a wet foam near the foam-liquid interface, while a dry foam would exist near to the top of the container. The container was then imaged

along its length. Our first relatively successful tomographic reconstructions is seen in Fig.3.40.

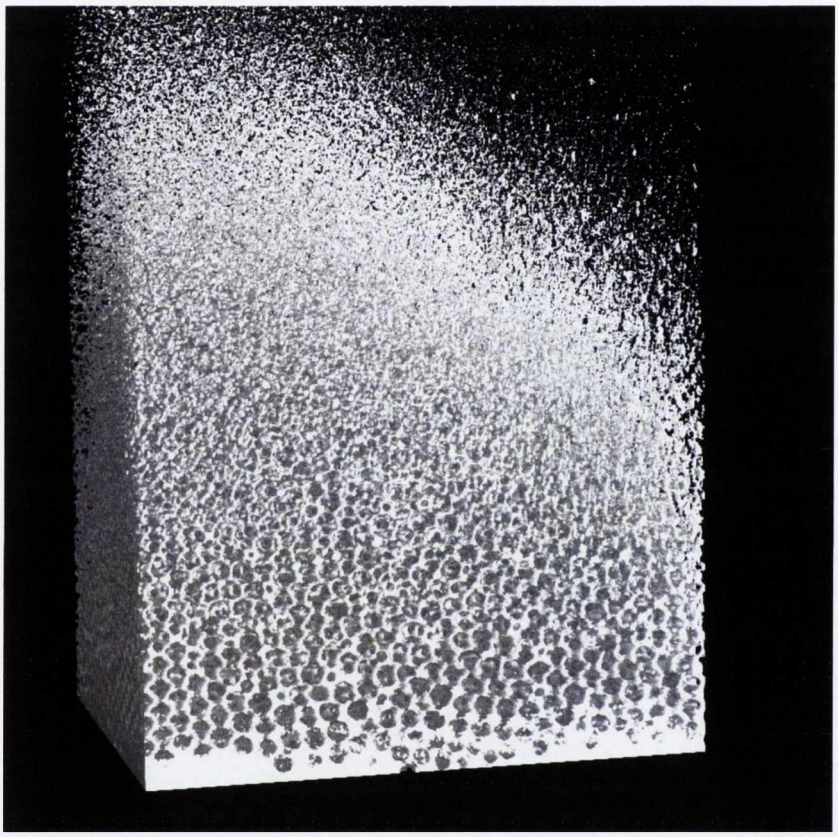

Figure 3.40: Imaging of monodisperse foam of average bubble diameter roughly 400 μm. Successful reconstruction of the foam is possible only near the foam-liquid interface. As the distance from this interface is increased, the liquid fraction of the foam decreases, and reconstruction is no longer possible.

Close to the foam-liquid interface, successful reconstruction of the foam sample is possible. However, the local liquid fraction of the foam decreases with distance from this interface, resulting in a reduction of the X-ray absorption profile of the foam, resulting in a failure to reconstruct the dry areas

of the foam. Thus, we are unable to successfully observe the transition between fcc and bcc regions. In an attempt to increase the X-ray absorption of our foam sample, we added silica nanospheres to our surfactant solution. This has been previously found to increase the probability of imaging such features using our low-energy X-ray tomography method [54]. We found, however, that this did not produce the increase in X-ray absorption required to produce a usable reconstruction. With our current imaging technique is therefore not able to successfully image this fcc to bcc transition.

3.5 Conclusions

We have investigated the crystalline nature of monodisperse aqueous foams in a rectangular container. We have found that small samples, 8 layers deep, form fcc foam crystals. The crystal nature of the sample was determined through the analysis of the packing structure of subsequent layers of the foam sample and the radial distribution of the center positions of the bubbles. This ordering was seen to propagate through the foam bulk of the thin sample. These thin foam samples are seen to demonstrate many three-dimensional crystalline defects, including grain boundaries and interstices, due to the rectangular confinement of the sample.

On increasing the number of layers of the foam sample, it is seen that the crystal nature of the sample changes. Along the boundaries of these samples, hexagonal ordering is seen to occur. The central regions of these samples, however, do not demonstrate any particular hexagonal ordering. On calculation of the RDF for these samples, the second peak of the distribution was seen to split with sub-peaks located at roughly $\frac{r}{r_0} \approx \sqrt{3}$ and 2. This split second peak is associated with a Bernal packing of spheres. This is the first observation that the center of these samples are not crystalline in nature. In addition, this is the first experimental evidence that a foam may be approximated as a Bernal packing of spheres.

We also investigated the temporal evolution of our monodisperse foam samples. To do this, we image a sample composed of 16000 bubble formed into a sample 14 layers in depth. On the first day of the experiment the sample was composed of ordered regions along the boundary of the sample and a disordered region within the center of the sample. Over the seven days of the experiment, this disordered region was seen decrease in extent over the lifetime of the experiment. Through the calculation of the translational order parameter G and the Q_4 and Q_6 bond orientational order parameter, the ordering of this central region could be charted. It was seen that the system did indeed progress towards a more ordered state. Through a calculation of the ratio of the number of fcc and hcp ordered bubbles, it was seen that there is a preference for the formation of fcc rather than hcp regions of crystallisation, in keeping with recent theoretical calculations and previous experiments.

On calculation of the packing fraction of the sample, it was found that the packing fraction of the sample resided above the upper bound of 0.74 associated with hard spheres. It was also found that ordering of the sample did not produce a corresponding increase in the packing fraction measurement. To determine the reason for this unusual behaviour, the Voronoi tesselation of the internal structure of the foam sample was computed. This allowed the packing fraction of each cell within the foam sample to be calculated separately. From these measurements, it was again seen that the average packing fraction was independent of the structure of the foam sample. On examination of the individual cells, however it was found that the packing fraction increased as a function of height h within the sample. We therefore see that packing fraction is not a good metric of order within a foam system, unlike for hard sphere systems.

We believe that the onset of ordering of this sample is due to an unintentional "annealing" caused by a change in temperature within the experimental lab over time. The sample was kept in an experimental lab the temperature

of which changed by up to $5°C$ between day and night. This change in temperature leads to an expansion and contraction of the bubbles within the sample. This 'anneals' of the sample, leading to an increase in order over time.

We attempted to capture the transition between regions of fcc and bcc crystallisation. It was found, however, that the sensitivity of our current experimental apparatus was not sufficient to capture this transition, due to its low liquid fraction.

Chapter 4

Forming the Weaire-Phelan structure - the use of templates for directed foam crystallisation

In Chapter 3 we saw how bubbles may spontaneously crystallise into fcc or hcp structures. Here we report on experiments using templates, which force bubbles, of the appropriate bubble size, into predefined crystals. Using such techniques we were able to produce for the first time an experimental example of the Weaire-Phelan structure.

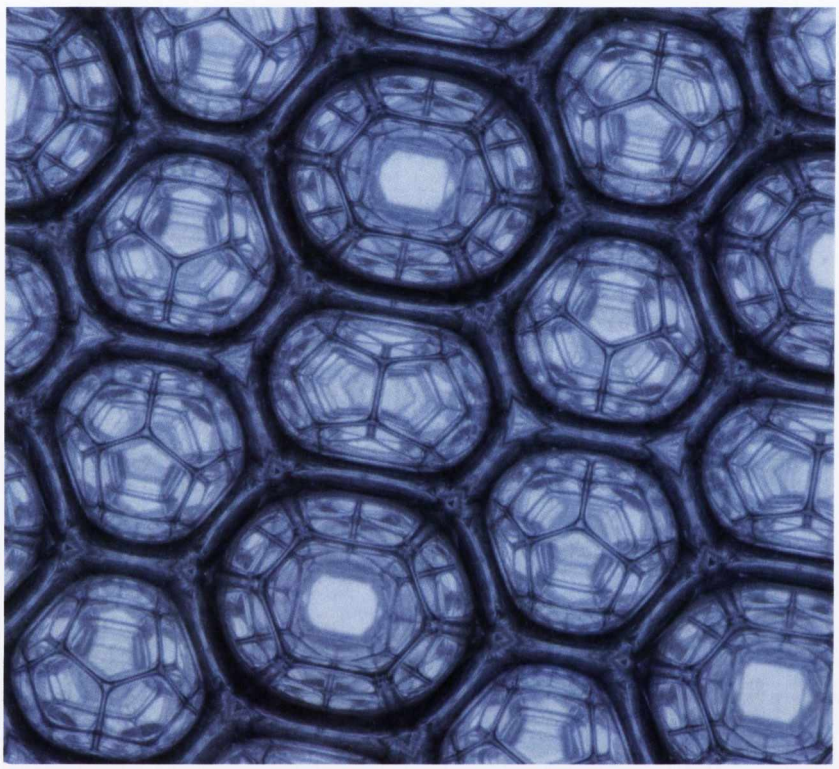

Figure 4.1: High resolution image of the Weaire-Phelan structure composed of monodisperse bubbles of average diameter 1.2 mm

4.1 Weaire-Phealan structure

From our X-ray tomographic experiments, we have seen that monodisperse aqueous microfoams spontaneously crystallise into fcc and hcp crystal structures, as well as random Bernal packings [72]. These structures, however, are associated with a wet foam, where the liquid fraction of the foam is above 15% [73]. For lower liquid fractions the expected energy-minumum configuration is different. Kelvin's original conjecture for the most efficient partitioning of space was a 14-sided truncated octahedron, arranged into a bcc lattice [74].

Computer simulations, however, have shown that this Kelvin cell is not the most efficient partitioning of space. Indeed, in 1993, Prof. Denis Weaire and his PhD student, Robert Phelan, showed that a new structure - the Weaire Phelan (WP) structure - was more efficient than Kelvin's original solution [14]. This structure is based upon the energy-minimised Voronoi tessellation of the A15 lattice with the constraint that the cells of the resulting structure are of equal volume. The WP structure is composed of an ordered arrangement of two types of polyhedral cells - an irregular dodecahedron and a tetrakaidecahedron (coloured red and green respectively in Fig. 4.2).

Since its discovery in 1993 an experimental realisation of the structure proved elusive, except for reports of sightings of partial WP structures [75]. Instead, dry monodisperse foams were found to form random structures with a wide distribution of cell shapes [76]. However, Fortes *et. al.* found that by confining monodisperse bubbles of average diameter 3 mm between a liquid interface and a glass plate, large crystalline samples of the Kelvin structure could be produced [77]. Such experimental examples of the Kelvin structure could also be produced through the use of monodisperse microbubbles. By reducing the liquid fraction of such foam, either through the manipulation of the osmotic pressure [5] or generating a foam column a few centimetres in height [29], a transition between an fcc and a bcc foam crystal may be provoked.

The relative ease by which the Kelvin structure is produced in experiment when compared to the more efficient WP structure is due to a fundamental difference in their structure. The {110} planes of the Kelvin structure are well adapted to fit against a planar surface, forming a surface pattern close to that of the honeycomb [1, 78]. Due to this, the Kelvin structure may be easily produced against a flat liquid surface, or against the flat walls of most experimental containers. The WP crystal, however, cannot be cleaved so as to present such a flat surface.

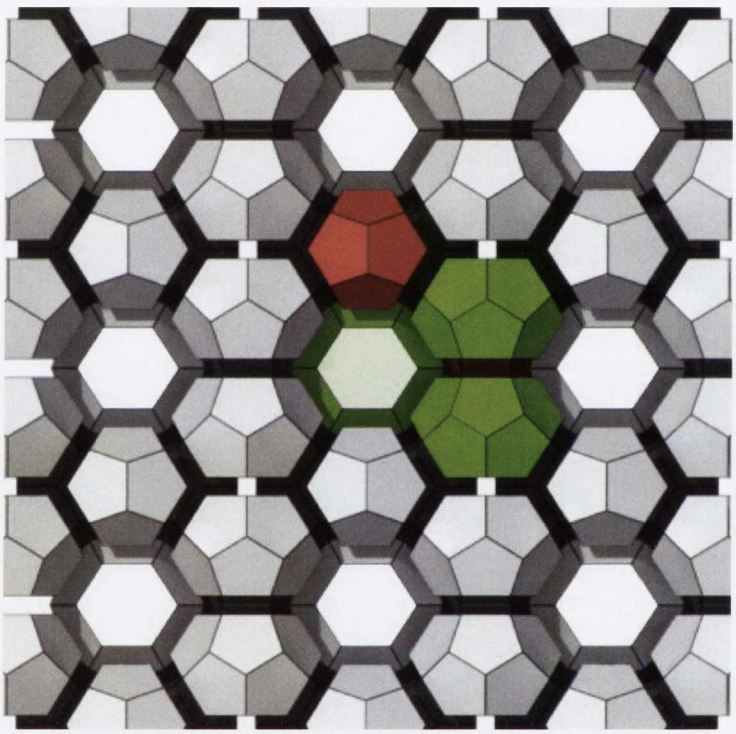

Figure 4.2: Computer generated Voronoi tessellation of the A15 lattice under the constraint of equal-volume cells. The WP structure is the surface-minimised version of this tessellation. The structure is composed of two layers of bubbles on parallel {111} planes. The unit cell of is shown is shown in colour - dodecahedron highlighted in red and tetrakaidecahedra in green. Image generated with 3 dt [15].

4.1.1 Experimental method

The experimental formation of the WP structure required the production of a container the surface of which is templated with the WP structure. Initially, an attempt was made to produce such a container using the commercial software *Solidworks* [79]. However, it was found that the complicated nature of the curved surfaces involved in the construction of large WP templates exceeded the resources available to this software. Instead, the template geometry was produced using the freely available software *Surface Evolver*[80]. A large rectangular WP structure was produced such that the {100} planes formed the walls of the structure. This crystal was then subtracted from a rectangular block, producing a schematic composed of the negative of the WP structure. The schematic was saved as a .stl file, suitable for processing using a 3D printer. The physical container was then fabricated using an *object 250* ^{TM} rapid prototype machine allowing the generation of objects of resolution 85 μm. The material used for the generation of these templates was *Objet FullCure720*. This transparent material allows the sample to be illuminated from a wide variety of directions. An example of one such template is shown inis shown in Fig. 4.3.

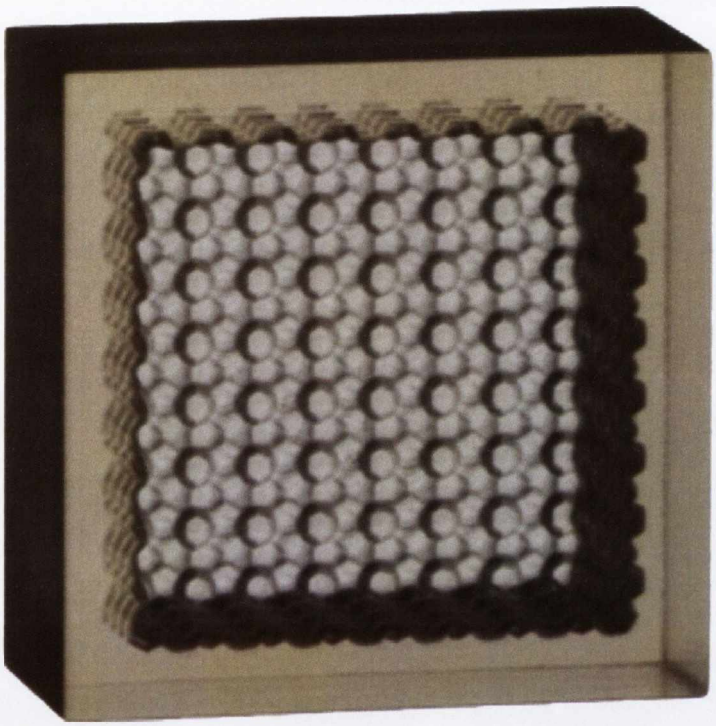

Figure 4.3: Photograph of the template used to produce the WP structure. The template is placed in a surfactant solution, to receive bubbles emitted from below. The inner surfaces correspond to {100} faceted planes of the WP structure (sample dimension 41x41x20mm^3; lattice spacing 4mm; volume available to each bubble 8mm^3; maximum number of bubbles 16 x 16 x 7 = 1792).

A surfactant solution of 1% volume fraction *Fairy Liquid* in water was used. Monodisperse bubbles were produced through the injection of nitrogen gas through a capillary tube with internal diameter of roughly 0.3 mm, placed into the surfactant solution at constant depth. The diameter of the resulting bubbles was determined by measuring the inter-bubble distances in a two-dimensional closed-packed array of bubbles. The WP container was inverted

in the surfactant bath to remove trapped air and positioned to collect the microbubbles. By varying the filling time of the container, the number of complete foam layers could be controlled. Once filled, the container was sealed by sliding a glass plate over the open face of the container. The container was then slightly shaken by hand as this was found to produce coherent foam crystals. Finally, the sample was then mounted on a glass stand, illuminated from above using a planar backlight, and photographed from below using a Canon EOS 50D camera.

4.1.2 Results

An example of the resulting WP structure is seen in Fig.4.4. A comparison between the vertex positions in the experimental foam (Fig.4.4) and the simulation of the WP structure (Fig.4.2) shows that coherent WP foam crystals could indeed be formed. We have successfully made foam crystals up to 1600 bubbles in size. We have also made foam crystals up to 6 bubble layers in thickness, seen in Fig.4.1.

As seen in Fig.4.1, the tetrakaidecahedron cells of the experimental WP structure apparently have a square central face, expanded on in Fig.4.6a. This is due to an optical effect of produced by the bubbles of the WP structure in contact with the liquid layer. The surface of these bubbles are hemispherical in shape (see Fig.4.5), resulting in a lensing effect, making the faces of subsequent layers of the WP structure appear smaller.

We may show this by treating the surface of the bubbles as ideal hemispheres (see Fig.4.5). Applying the usual equations associated with refraction from a curved interface, it may be shown that the magnification M associated with such an interface is given by

$$M = \frac{1}{\frac{n_2 - n_1}{R n_2} S + \frac{n_1}{n_2}} \tag{4.1}$$

Where n_2 and n_1 are the refractive indices of the water and liquid phases,

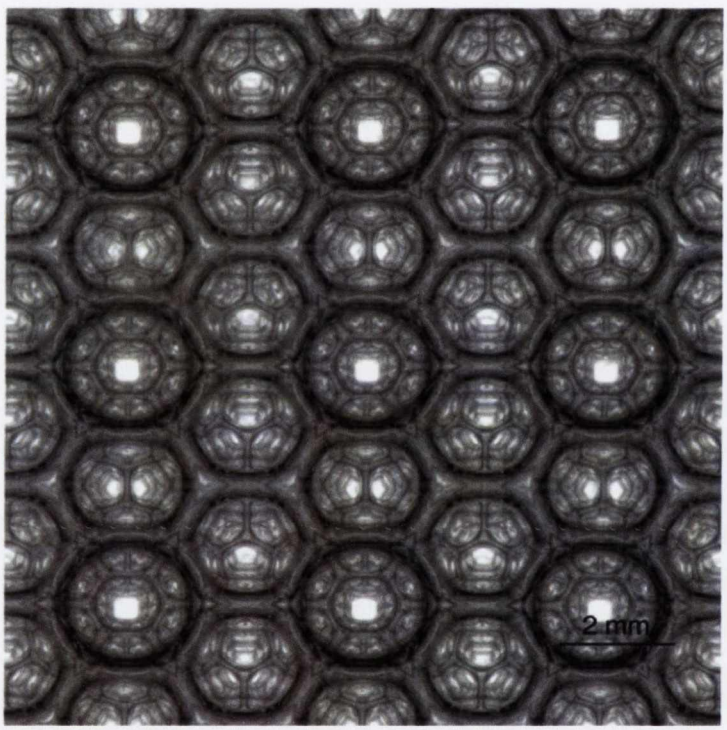

Figure 4.4: Photograph of the experimentally produced WP foam viewed along its ⟨100⟩ 2-fold axis of symmetry. The foam was produced in the template shown in Fig.4.3. The sample contains approximately 1500 bubbles, arranged into six layers. Many fine details are observed, which are also seen in simulation, confirming the absence of defects.

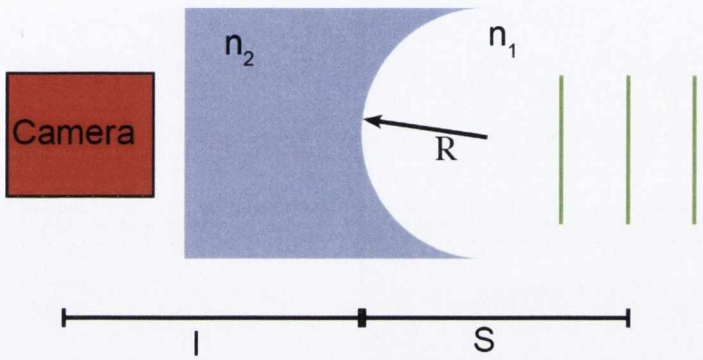

Figure 4.5: Illustration showing hemispherical interface which results in the optical distortion of the WP structure, resulting in the formation of an apparent square face in what WP structure when viewed along the $\langle 100 \rangle$ direction. The hexagon faces of the WP structure are shown as green planes.

R is the radius of curvature of the bubble interface in contact with the liquid phase. Using Mathematica we apply this magnification constant to a series of hexagons, rotated 90° with respect to each other and separated by the same distances as they would appear in an experimental foam. It is seen that the resulting image mimics the experimental photographs of the WP structure, as shown in Fig.4.6.

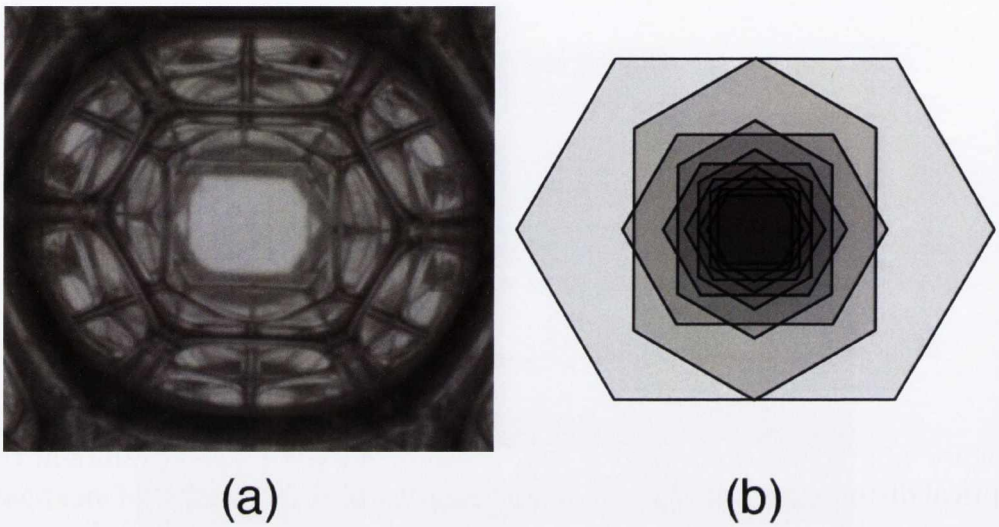

Figure 4.6: (a) Detailed view of one of the tetrakaidecahedron cells of the experimental WP structure. (b) A simulation of the optical effect leading to the apparent square face within the WP structure.

We found that coherent foam crystals could only be produced if the bubble size was matched to the template dimension. If a direct match between the two length scales was not made, the resulting foam contained several defects.

Several templates were made for different bubble sizes. It was found, however, that WP crystals could not be produced for bubble diameters greater than 3 mm in diameter. The deposited bubbles are seen to deform, failing to produce the WP structure. For smaller bubbles, it was again found that the production of a WP structure was difficult. This is due to the WP structure being not stable for liquid fractions above 0.18 [81].

4.2 Directed-crystallisation of wet foam samples

In Chapter 3 we have seen that monodisperse micro foams spontaneously order into hexagonally closed packed crystals for small foam samples, while larger samples exhibit random disordered arrangements of bubbles within the foam bulk [72]. For future experiments, as well as for industrial applications, we are interested in methods by which the structure of these wet foam samples may be controlled. To do this, we investigate how the surface of the containers into which the bubbles are placed influences the resulting foam structure.

Our previous experiments involved placing monodisperse bubbles into rectangular containers with flat internal surfaces. These flat surfaces are complimentary to the $\langle 111 \rangle$ closed-packed planes of the fcc lattice. In particular, the flat top of the container against which the bubbles are forced due to buoyancy, causes these bubbles to form a fcc $\{111\}$ closed packed plane, with defects required to match the rectangular boundary condition of the container. We believe that this closed-packed plane then forms a template, which provokes the ordering of further bubble layers.

To determine the effect of the structure of this top surface layer on the resulting foam structure, we investigate the effect of a "rough" surface on the resulting foam structure. Following this, we determine if an ordered arrangement of cylinder holes may evoke the crystallisation of a monodisperse foam sample along the fcc $\langle 100 \rangle$, as has been previously demonstrated in colloidal crystals [82].

4.2.1 Random-template surface

To determine if a rough surface will frustrate the formation of an initial ordered foam layer, and thus the formation of an ordered foam crystal, a template was designed composed of a random arrangement of square pegs,

each peg of dimensions 0.8 x 0.8 x 0.8 mm^3. A random arrangement of these pegs was guaranteed through the use of a computer script which produced a random 24 x 24 array of 1s and 0s. This array was then used to produce an arrangement of 24 x 24 pegs, the presence or absence of a peg corresponding to a 1 or 0 in the generated array. The resulting template is shown in Fig.B.5. Monodisperse bubbles of average diameter 790 $\pm$ 40 μm were placed into the container using the method described in section 3.1, after which the sample was imaged by X-ray tomography, the reconstruction of the foam shown in Fig.4.7.

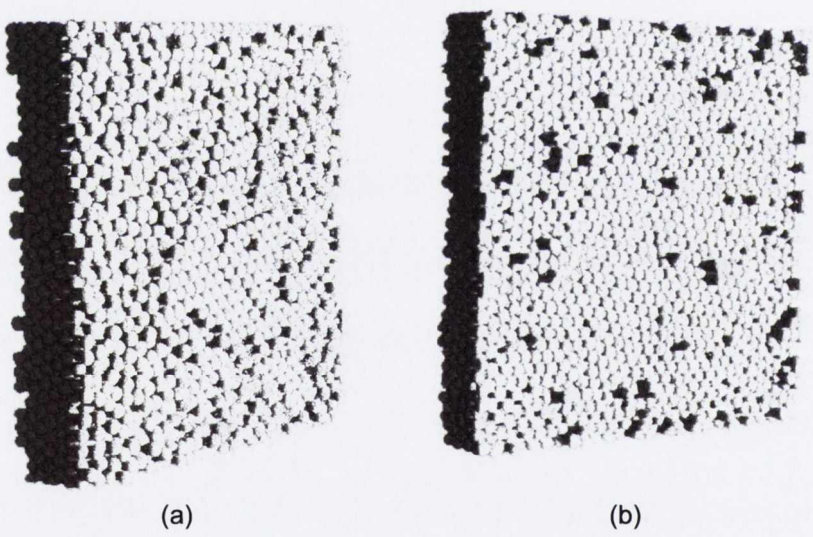

Figure 4.7: Ordering of bubbles 790 $\pm$ 40 μm within the the container with the random template, shown in Fig.B.5.(a) and (b) show the top of the foam, in contact with the templated surface, and the bottom of the foam, in contact with the foam-liquid interface, respectively. It is seen that both of these faces, although not planar in nature, appear to be closed-packed.

It is seen that both the top of the foam, in contact with the container

template, and the bottom of the foam, in contact with the foam-liquid interface, show the same hexagonally ordered structures. To determine the exact nature of this ordering, we calculated the RDF of the the foam structure, shown in Fig.4.8. This RDF is compared against the RDF of an ideal fcc lattice, as well as the crystalline foam sample examined in section 3.2.1.

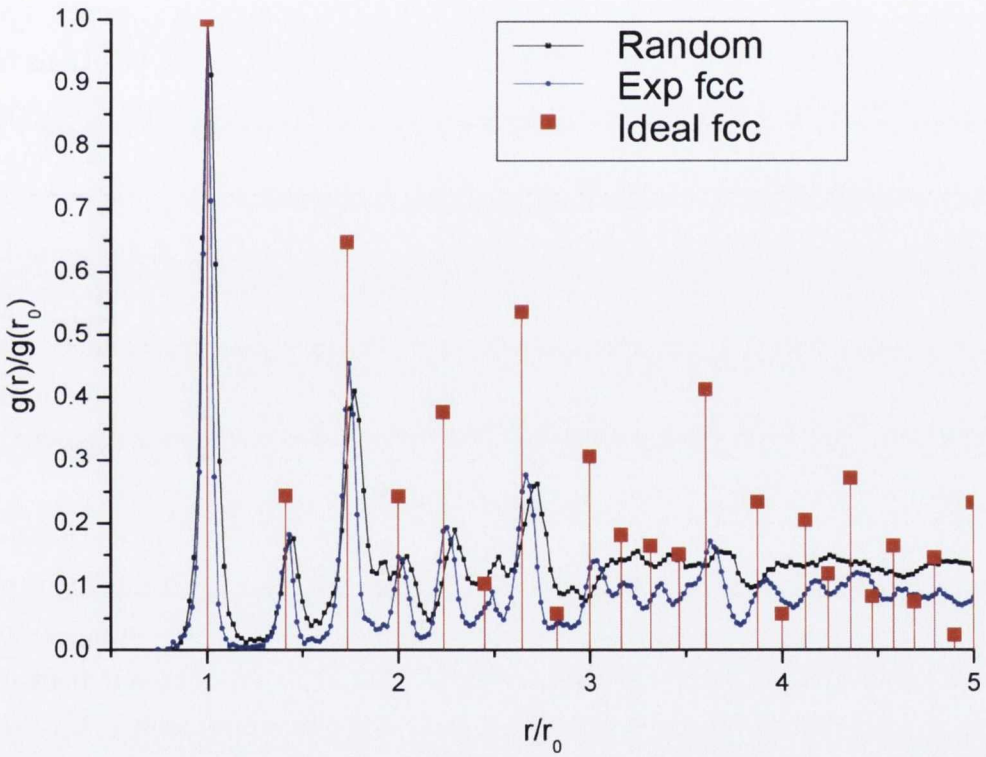

Figure 4.8: Graph showing the RDF of the sample shown in 4.7. The narrow peaks of the distribution, and coencidence with the theoretical peaks of an ideal fcc lattice, indicate the formation of such a structure.

Although the peak positions of this sample compare favourably with the peaks of the ideal fcc lattice, it is seen that a deviation of this RDF is seen when compared to the RDF of a sample ordering against a flat boundary.

We believe this deviation is due to the rough boundary condition imposed upon the sample. However, on the whole, the sample may still consider the sample as ordered.

4.2.2 Fcc ⟨100⟩

A container was produced the top surface of which was templated with a square arrangement of cylindrical holes, of diameter $800\mu m$ and depth 400 μm (see Fig.B.3). These cylindrical holes matched the expected positions of bubbles within a fcc ⟨100⟩ plane. Monodisperse bubbles of approximately $800\mu m$ were introduced into the container and imaged using X-ray tomography, the result of which is shown in Fig.4.9.

The square arrangement of bubbles in each layer of the foam sample indicate that the sample has been successfully directed to crystallise along the fcc ⟨100⟩. Several defects are seen to occur within the sample, such as a grain boundary seen in the middle of the sample. This, we believe, is due to a possible mismatch between the template and bubble size. Such a mismatch has been see to produce similar defects within colloidal crystals [82].

In addition to the the templated container composed of a square arrangement of cylindrical holes, an additional template of a square arrangement of cubic "pegs" was constructed. It was originally hoped that these square pegs would again force the foam structure into a similar square arrangement of bubbles, invoking the formation of fcc {110} planes in subsequent foam layers. The top surface of this container was composed of a square lattice (12 x 12) of cubic "pegs" (0.8 x 0.8 x 0.8 mm^3) as shown in Fig.B.3. Fig.4.10 shows the ordering of a foam sample, 6 layers deep, of average diameter 840 $\pm$ 40 μm within this container. It is seen that the topmost layer of the foam, in contact with the template surface of the container, has indeed form a square arrangement of bubbles associated with an fcc ⟨100⟩.

We calculated the RDF for the sample, the results of which are shown in Fig.4.11. Unexpectedly, however, the RDF demonstrates the same form as

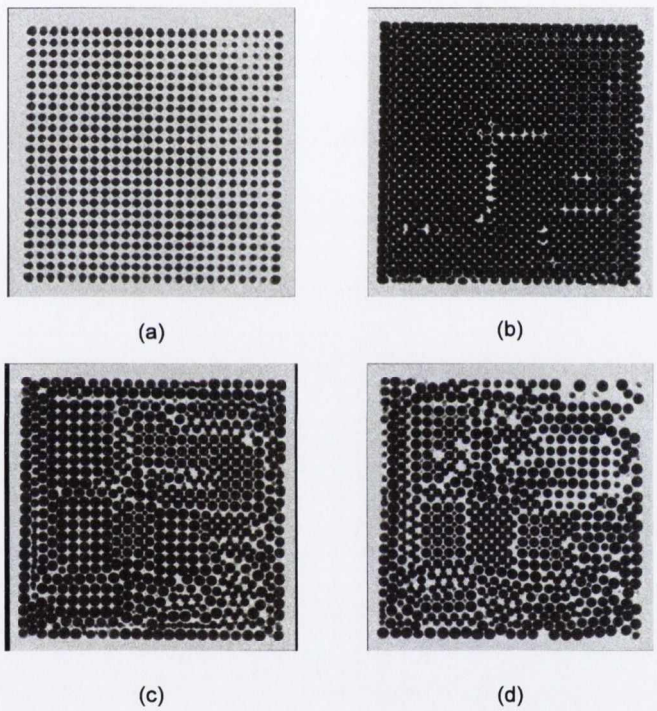

Figure 4.9: Images showing 2D image slices through the monodisperse foam of average bubble diameter approximately 800 μm placed within the templated container shown in Fig.B.3. (a), (b), (c) and (d) show sections taken through the 1^{st}, 2^{nd}, 3^{rd} and 4^{th} layers of the foam sample. The square arrangement of the bubbles in each layer indicate that the foam sample is growing along the $\langle 100 \rangle$.

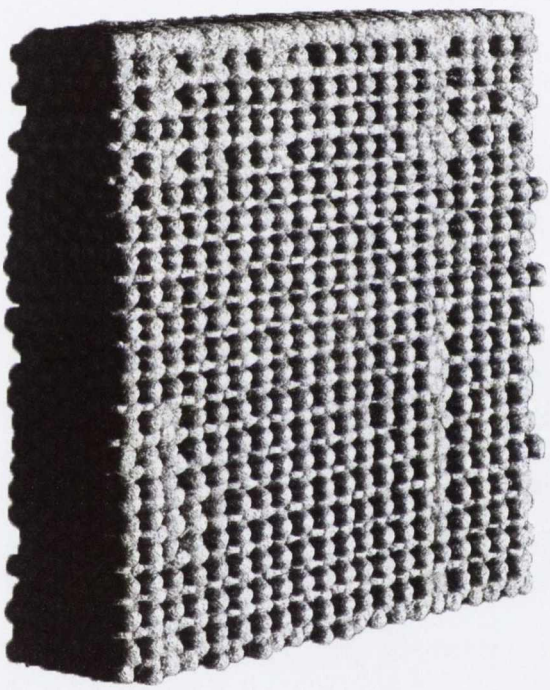

Figure 4.10: Ordering of bubbles 840 $\pm$ 40 μm within the the container templated with the square lattices of pegs shown in Fig.B.3. It is seen that the topmost layer of the foam sample, in contact with the container template, has ordered into a regular square arrangement of bubbles.

for a random packing of bubbles, as demonstrated in section 3.2.1.

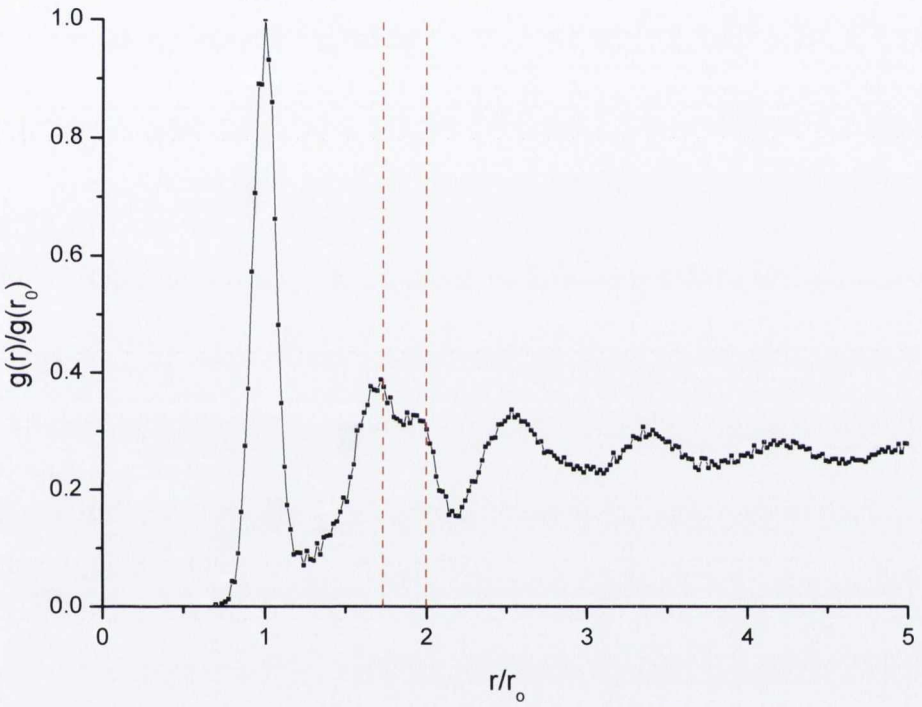

Figure 4.11: RDF for the sample shown in Fig.4.10. It is seen the the function is composed of broad peaks, with a split second peak characteristic of a random packing of bubbles. The red lines, drawn at $\frac{r}{r_0} = \sqrt{30}$ and 2 indicate the positions of the two sub-peaks associated with a random packing of spheres.

4.2.3 Conclusions

We have successfully produced the Weaire-Phelan structure using a container the internal surfaces of which were templated with the Weaire-Phelan struc-

ture. Perfect crystals of up to 1600 bubbles were easily formed. Continuing research will be devoted to other possible ordered foam structures, including the family of clathrates and structures such as those derived from the Frank–Kasper phases, which have been conceived and discussed for many years, but never realized [83, 84, 85]. Achieving this will open the field to the experimental investigation of their properties. In addition, such samples could be solidified using gelling agents [86], opening up further possibilities to experimentation and application.

We have also seen that simple templates may also be used to alter the crystal structure of these monodisperse foam structures. A rough boundary condition was not seen to change the crystallisation of the sample. Through the use of a square arrangement of cylindrical holes of the same diameter as that of the bubbles employed in experiment, we were successfully able to direct the growth of a foam along the fcc {100} direction. it was found that a similar square arrangement of pegs frustrated the crystallisation of the sample, the resulting bubble pile resembling a disordered packing of spheres.

Chapter 5

Building the pyramids: perfect bubble crystals

5.1 Introduction

Through the use of X-ray tomography, we have seen that the internal structure of monodisperse microbubbles (see Chapter 3). We have seen that these foam samples may be either fcc, polycrystalline, or indeed disordered in structure [72]. This is due, in part, to the rectangular containers in which these foam samples are prepared. Such a container will generally produce a sample containing grain boundaries, because the favoured surface planes of the crystal structure (e.g. {110} etc. for the Kelvin structure) cannot be matched to all of the faces. This is also the reason fcc crystals grown in such a container are found to contain grain boundaries [29].

If we wish to extend the initial work of Bragg (see section 1.1.2), however, extending the bubble model of crystal structure in three dimensions, an efficient method of controlling the crystal structure of the sample is required. This is necessary as, unlike in the two-dimensional raft of Bragg, there exist several stable structures in three dimensions [60].

We have seen in chapter 4 that we may control the crystal nature of a

sample through the use of a templated mould to direct the crystallisation of the sample. Using such a technique, we have successfully generated the first experimental realisation of the Weaire Phelan structure (see chapter 4.1). This templating method, however, has associated with it several disadvantages. Firstly, due to the fine detail required to produce a given structure, this templating method requires access to high-precision manufacturing facilities. Secondly, due to the requirement of matching the bubble size to the template dimensions, a new container must be produced for each bubble size. This also results in the failure of many experiments due to slight variation in the bubble size.

In this chapter, we report on the development of a technique to direct the crystallisation of a foam sample through the use of flat-sided *pyramidal shaped* containers. This new method offers the possibility of creating perfect single crystals, without the rigorous control over bubble size required when using a rectangular container [87], or a templated container [88]. In addition, the flat boundaries of such a container do not require the same precision machining that a templated container requires. Finally, the initial growth in small layers at the apex of the pyramid effectively seeds the growth of a single crystal. Accidental grain boundaries therefore seem less likely in a pyramid.]

Our strategy has fulfilled expectations. In particular, perfect fcc crystals of up to 500 bubbles have been made very easily. With appropriate pyramids, we have also made bcc and simple cubic crystals, although the total number of bubbles that can be ordered is severely limited by instability[89]. We believe this instability will become less limiting when smaller bubbles are used.

We are also able to make strained versions of all these crystal types through small variations of pyramid geometry. Further designs can induce deliberate defects, such as the fcc twin boundary described here in section 5.3.1. In addition we have conducted the first experiments aimed at producing ordered bidisperse foam, analogous to familiar ionic solids, with some

success, and the expectation of their extension to larger systems.

Our work carries further into three dimensions the original research programme of Bragg, which was to use bubbles as model atoms. In addition the methodology may also provide a route to fabrication of solidified crystals for a variety of applications, e.g. polymeric, metallic or ceramic foams, possibly for industrial applications [86].

5.2 Experimental techniques

To create a crystal of a given type, a container must be fabricated the walls of which are parallel to an appropriate plane of the corresponding lattice. By examining the conventional cells of the sc, bcc and fcc crystal structures, as shown in Fig.5.1, such a choice may be made by selecting close-packed planes or planes on which the spheres are relatively well packed.

For example, the selected simple cubic (sc) pyramid geometry is formed from the intersection of three {100} planes, producing a tetrahedron with a vertex angle - the face angle at the vertex of the pyramid - of 90°.

The chosen bcc pyramid, produced from the intersection of four {110} planes, is a 4-sided pyramid of vertex angle $\cos^{-1}(\frac{1}{3})$.

The walls of the fcc pyramid are formed from the intersection of three {111} planes, resulting in a regular tetrahedron of vertex angle 60°. Note that during the extraction of these geometries no reference has been made to any particular bubble size. The intention is that these geometries should evoke particular crystal types independent of the size of the particles being used.

Most pyramids were fabricated with a *Object 300* rapid prototype machine using Object Vero Clear polymer as was used for the WP structure. Each of these pyramids had an internal edge length of 3 *cm*. Larger pyramids were fabricated by hand using perspex sheeting.

As a preliminary, several hard-sphere experiments were conducted. The

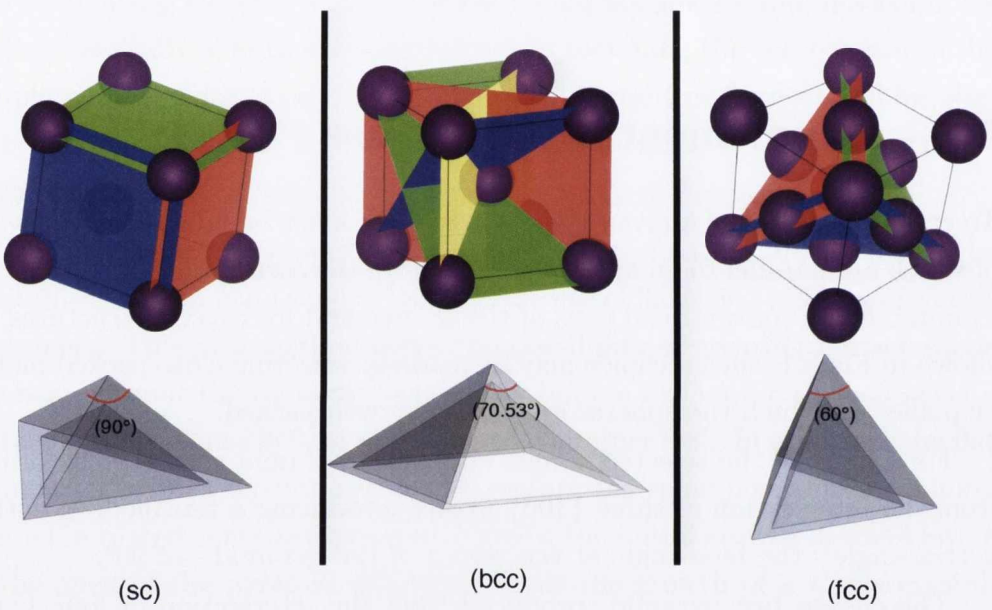

Figure 5.1: The conventional crystal cells and appropriate pyramid container associated with simple cubic (sc), body-centred cubic (bcc) and face-centred cubic (fcc) crystals. The chosen crystal directions that correspond to well-packed planes are highlighted. The intersection of these planes produces the pyramid structures which may be used to direct crystallisation of monodisperse and bidisperse foams. Unit cell images produced using Vesta rendering software [90].

pyramids were inverted and filled with monodisperse metal spheres of diameter 0.98 ± 0.01 mm. This involved dropping spheres individually into a pyramid and shaking the structure slightly so the sphere would find its lowest position. The container was photographed after the addition of each sphere.

All our foam experiments were conducted using an aqueous solution of the commercial detergent *Fairy Liquid* (5 % volume fraction). Monodisperse bubbles were produced by the injection of nitrogen gas under constant pressure into this solution via a capillary tube (see Fig.5.2a). Bubble size was controlled by regulating the gas flow rate. Most of our experiments were carried out with bubbles of diameter significantly smaller than the capillary length (about 2mm). In this regime (that of *wet* foam), many layers of bubbles can be prepared under gravity, while maintaining spherical shapes with small distortions.

The average bubble diameter was determined from an experiment in which these bubbles are allowed to form a two-dimensional hexagonal raft at the surface of the solution. The centre-to-centre distance of bubbles then approximates the bubble diameter.

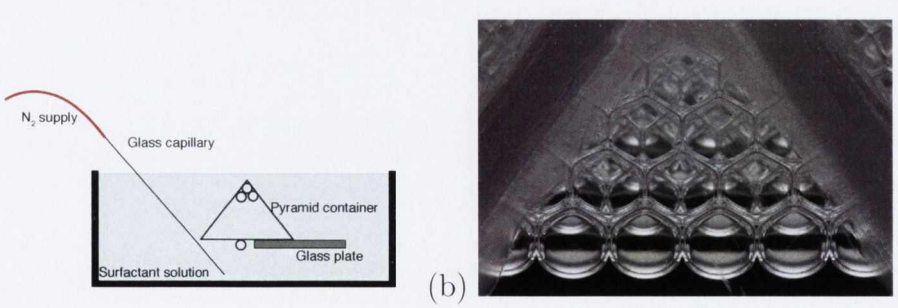

Figure 5.2: Experimental set-up. (a) An inverted open pyramid is submerged into surfactant solution and filled with monodisperse nitrogen bubbles. (b) Example of the side view of bubbles (diameter 5.04 ± 0.08 mm), crystallised in the bcc structure inside a pyramid of the type shown in Fig.5.1 (middle).

The pyramids were placed into the solution and inverted to remove trapped air, before being positioned with the apex pointing upwards, as shown in Fig. 5.2. They were then slowly filled from below with monodisperse bubbles, as described above. Due to the nature of our experimental setup, the filling process of the containers was not directly observable. Once filled, the pyramid was sealed by sliding a glass plate over the open side. At this stage, the pyramid was shaken gently by hand as this helps to produce coherent crystals. The container was placed on a glass stage, lit from above using a planar backlight and photographed from below using a CCD camera. The foam structure was checked by examining the refracted image of sub-surface bubbles in the outermost foam layers [28].

For the formation of a perfect fcc crystal within the geometry that we have constructed here, the number of bubbles N_{fcc} may be determined by counting the number of complete foam layers n. The i^{th} layer within the fcc foam will contain $\frac{i(i+1)}{2}$ bubbles. The total number of bubbles within the foam sample is then given as $\sum_{i=1}^{2} n\frac{i(i+1)}{2} = 1/6(n)(n+1)(n+2)$. Repeating this analysis for the ideal sc and bcc structures generated by out pyramids yields

$$N_{sc} = N_{fcc} = 1/6(n)(n+1)(n+2), \tag{5.1}$$

$$N_{bcc} = 1/6(n)(n+1)(2n+1). \tag{5.2}$$

5.3 Main results

5.3.1 Face centred cubic and related structures

As expected, the most successful experiments were those undertaken with the aim of producing the fcc structure, bounded on all sides (including the free surface of the bottom layer) by close packed planes.

The results of the hard sphere experiments is shown in Fig.5.3. The photograph shows the pyramid from above. It is seen that the growth technique successfully produces successive close-packed layers grown along the fcc $< 111 >$ direction.

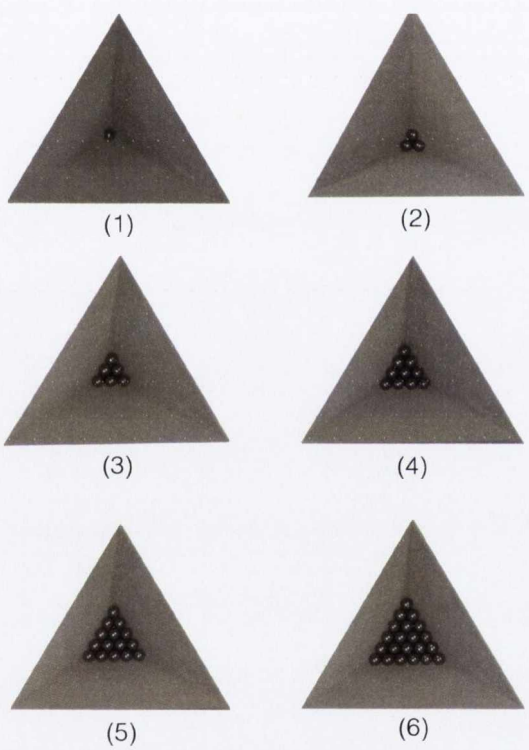

Figure 5.3: A series of images showing the growth of a hard-sphere fcc crystal within a regular tetrahedron of vertex angle 60°. Each image is labelled by the number of fcc layers imaged, showing the crystal growing to 7 layers deep. Note that each subsequent layer is close-packed and free of defects.

Bubbles were loaded into the pyramids as described above. As Fig.5.4 illustrates, using the 3-sided 60° pyramid we were able to produce perfect fcc crystals comprising of up to 500 bubbles. The photographs show three such crystals, consisting of bubbles of 0.54, 2.42 and 4.72 mm in diameter.

We find that fcc crystals are stable in both wet (bubbles much less than the capillary length $l_0 \simeq 2mm$) and fairly dry foams (bubbles larger than l_0).

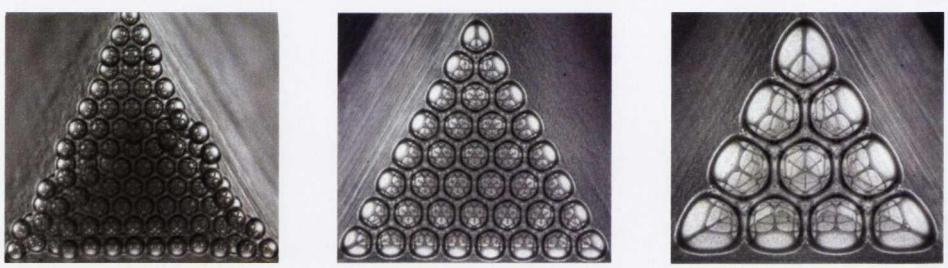

Figure 5.4: Images of the generation of fcc crystals for a 10 fold change in bubble size. The foam crystals are imaged from the base, i.e. in a $\langle 111 \rangle$ direction.

In order to demonstrate the flexibility of this technique to direct the crystallisation of foams, we designed a pyramid to produce a coherent grain boundary between the two distinct regions of fcc crystallisation. This geometry was formed conceptionally from the joining of two fcc pyramids producing a four-sided pyramid with a vertex angle of 60° (see Fig. 5.5a). The basal plane of this conjoined pyramid corresponds to crystal planes of $\{1\frac{1}{2}\frac{1}{2}\}$ type on each side.

It was found that this four sided pyramid was successful in generating a coherent grain boundary, a twin boundary between two perfect fcc crystals. Fig. 5.5b shows a typical example of the foam structure generated. The position of the grain boundary is highlighted. As the $\{1\frac{1}{2}\frac{1}{2}\}$ is not close-packed, the foam is seen to create two sets of opposed terraces of close-packed 111 planes (Fig.5.5c)

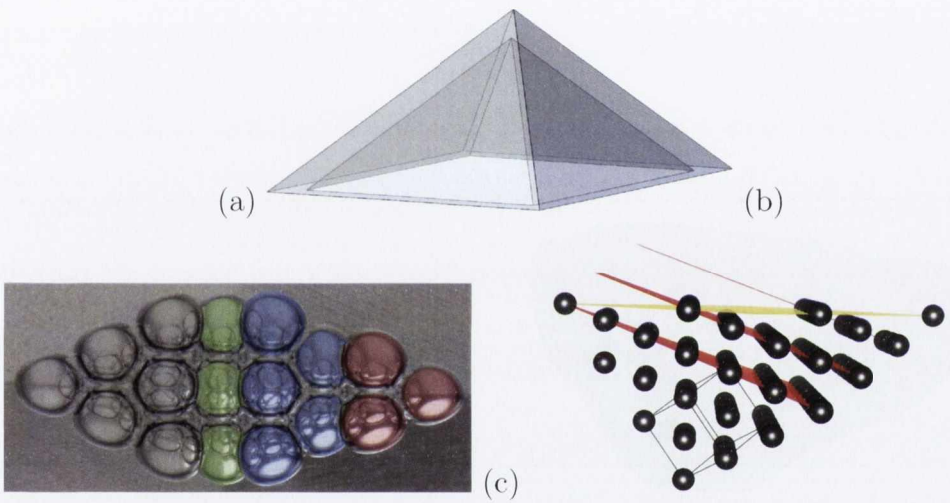

Figure 5.5: (a) Rendering of the four-sided 60° pyramid used to generate the coherent grain boundary. (b) Photograph showing the $\{1\frac{1}{2}\frac{1}{2}\}$ plane of the experiment. The first two $\{111\}$ planes are shown in red and blue, while the twinning boundary is shown in green. (c) fcc lattice showing the intersection of three $\{111\}$ planes (in red) and a single $\{1\frac{1}{2}\frac{1}{2}\}$ plane (in yellow). This intersection produces the stacked terraces of $\{111\}$ planes which are seen in experiment and indicated by matching colours.

5.3.2 Preliminary experiments on other systems

5.3.2.1 Body centred cubic crystals

Body centred cubic (bcc) crystals were formed in the 4-sided pyramid shown in Fig.5.1 (b). Our experiments with hard spheres readily show that these indeed form the bcc structure in this geometry, as is shown in Fig.5.6.

Our bubble experiments have shown that monodisperse foam structure within this pyramid strongly depend on the diameter of the bubbles used. For large bubbles (i.e. dry foams), with a diameter roughly greater than 2 mm, it is seen that the bubbles spontaneously crystallise into perfect bcc crystals. For such relatively dry foam, this is the well-known Kelvin structure [77, 29, 5]. We have successfully generated such perfect bcc crystals up to 7 layers deep composed of 140 bubbles. When the bubble size is reduced below 2 mm, it is seen that complete crystallisation of the sample is no longer guaranteed, pointing to the instability of bcc for wet foams (see section 1.1.2).

Nevertheless, the attempt to make bcc wet foams in this way is not futile. The shear instability of bcc refers to uniform shear and this is incompatible with the hard-wall boundary conditions of the pyramidal experiments. This is demonstrated by our ability to successfully form many-layered bcc crystals with incompressible hard spheres within such a geometry (see Fig.5.6). Our current inability to form bcc crystals with monodisperse bubbles is due to their finite compressibility, which is inversely proportional to the bubble radius. We therefore expect to be able to make such crystals (and also sc) up to a certain critical size determined by the capillary length, for sufficiently small bubbles.

5.3.2.2 Simple cubic crystals

An attempt was made to form a simple cubic (sc) crystal using the 90° pyramid shown in Fig.5.1. Note that the sc structure is susceptible to the same type of instability as the bcc lattice. Due to this we could only produce

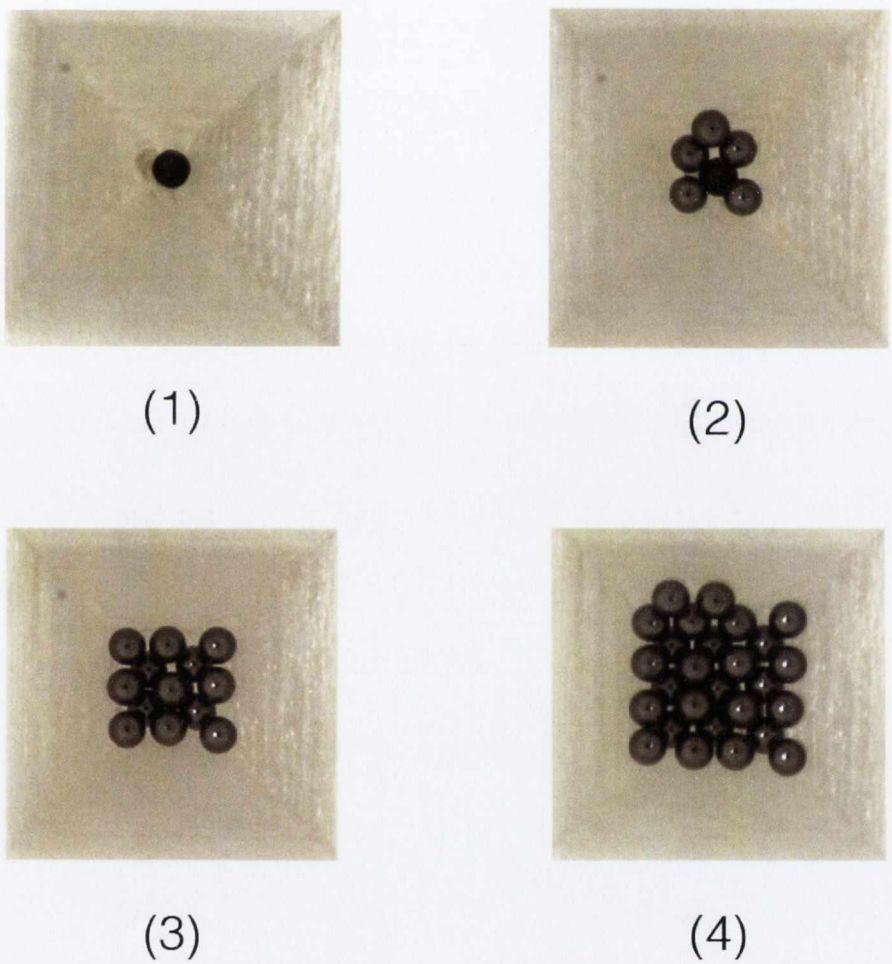

Figure 5.6: A series of images showing the generation of a bcc lattice of hard spheres of diameter 1 mm within a 4-sided pyramid. The images are labelled by the number of complete layers.

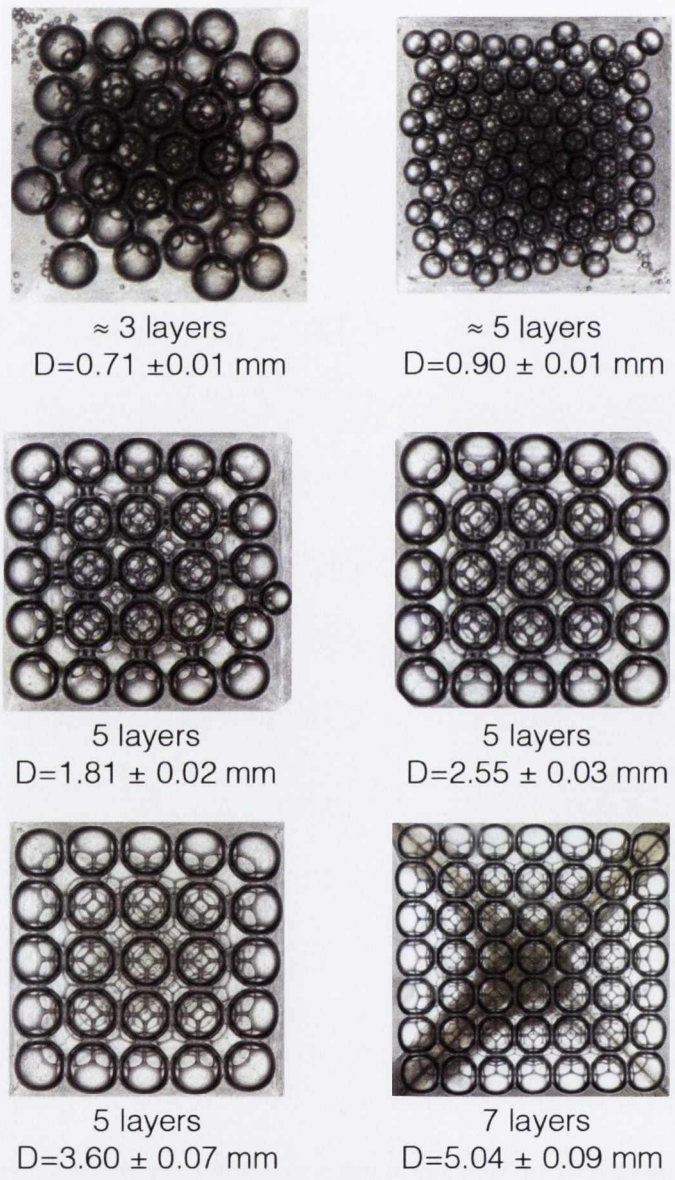

Figure 5.7: Within the square pyramid bubbles of diameter exceeding roughly 1 mm spontaneously crystallise into bcc along the $< 100 >$ direction. Such ordering does not occur for smaller bubbles (bottom row of photographs). (Photographs taken from below.)

perfect sc structures up to 3 layers in depth, as shown in Fig.5.8 (b). A second complication arouse in the intervention of the fcc crystal (Fig.5.8 (d)). This is due to the cubic symmetry of the two structures.

Increasing the number of foam layers above this, it was found that the foam formed a polycrystalline structure (see Fig.5.9). Close to the boundaries of the container, the foam orders into a sc structure, while the centres of such samples are arranged into a hcp configuration.

5.3.2.3 Bidisperse foams

We also carried out preliminary experiments concerning the ordering behaviour of *bidisperse* foams within the same geometries. In relation to the model of Bragg, this corresponds to the production of "ionic" bubble crystals and it also calls to mind the educational work of Rämme [91].

The experimental procedure was similar to that employed in the production of monodisperse foams. The pyramids were filled until the formation of a complete foam layer. This filling scheme was continued, the bubble diameter alternated between successive foam layers.

As shown in Fig.5.10, we formed three-layered ordered bidisperse foams. However, on production of the fourth layer, it is seen that the deposited bubbles disrupt the lower layers, producing interstitial defects and a disordered foam. It is possible that such a disturbance of lower layers occurs also during the formation of monodisperse foam crystals, but since in this case the bubbles are all the same, the foam can relax again into a perfect crystal. Future systematic experiments, involving a more gradual deposition process, should enable the formation of much larger ordered bidisperse foam samples, as there seem to be no inherent instabilities in this case.

5.3.2.4 Strained lattice

We have seen that a perfect fcc lattice may be formed through the ordering of bubbles within a three-sided pyramid of vertex angle 60°. By changing

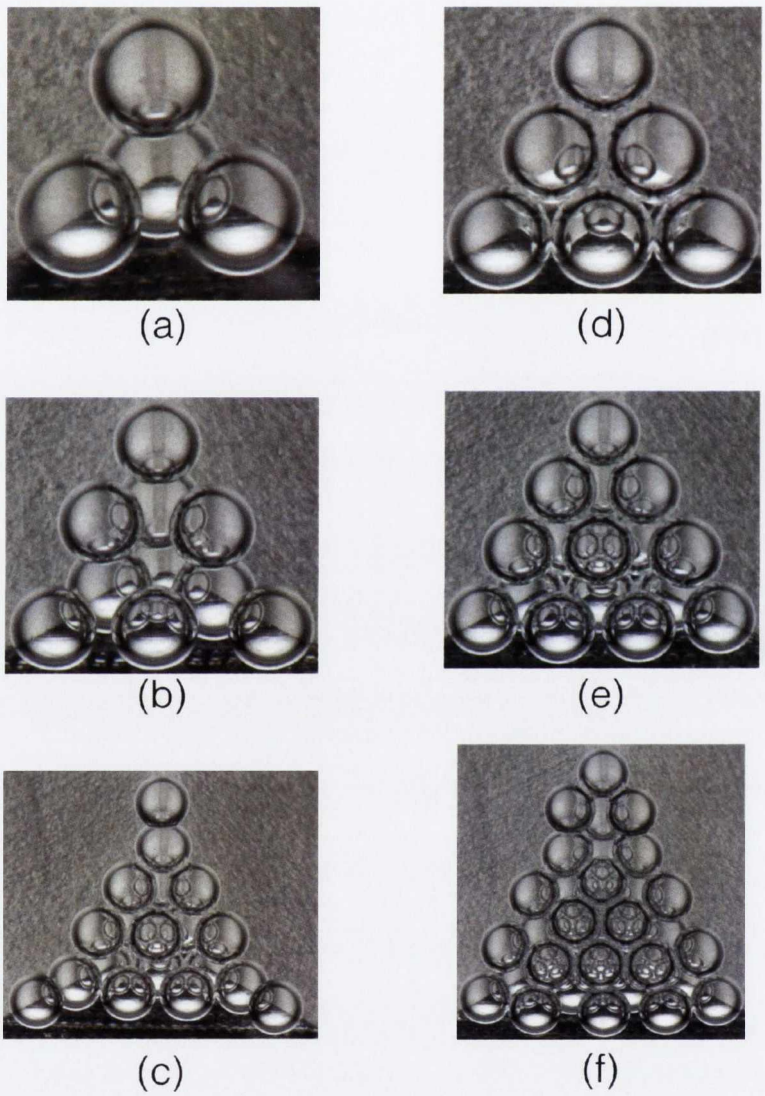

Figure 5.8: Formation of crystals in a three-sided pyramid of vertex angle 90° pyramid (bottom view, D= 1.09 ± 0.02 mm). (a), (b) and (c) show successive layers of a simple cubic (sc) lattice, with 3, 6 and 10 bubbles, respectively. However, (d), (e) and (f) show the formation of an alternative crystal structure, consisting of 6,10 and 18 bubbles in the successive layers.

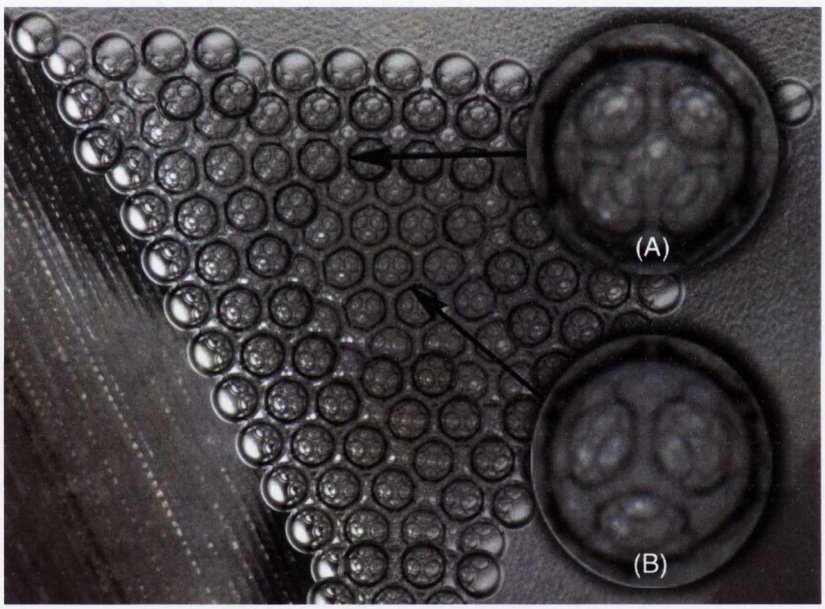

Figure 5.9: The same pyramid as in figure 5.8, but filled with more than 10 layers of bubbles (D=1.09 $\pm$ 0.02 mm, as before), shows the formation of a polycrystalline foam. In the centre of the crystal the bubbles have arranged into a hcp configuration (B), while closer to one of the pyramid walls they form an sc structure (A).

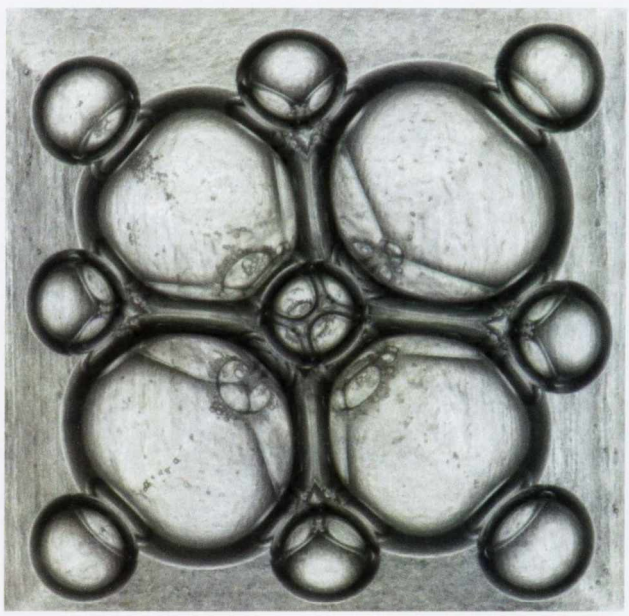

Figure 5.10: Three layers of an ordered *bidisperse* foam (bubble diameter ratio 0.37) within a 60° three-sided pyramid (bubble diameters: 5.60 ± 0.12 mm and 2.07±0.03 mm).

this vertex angle we can study the effect of a strain on the bubble crystal structure. We conducted a series of experiments where we placed monodisperse microbubbles into three-sided pyramids of vertex angle 60°, 65°, 75°, 85° and 90°. In this way, we can also investigate the transition of an ordered foam from a fcc configuration to a sc configuration.

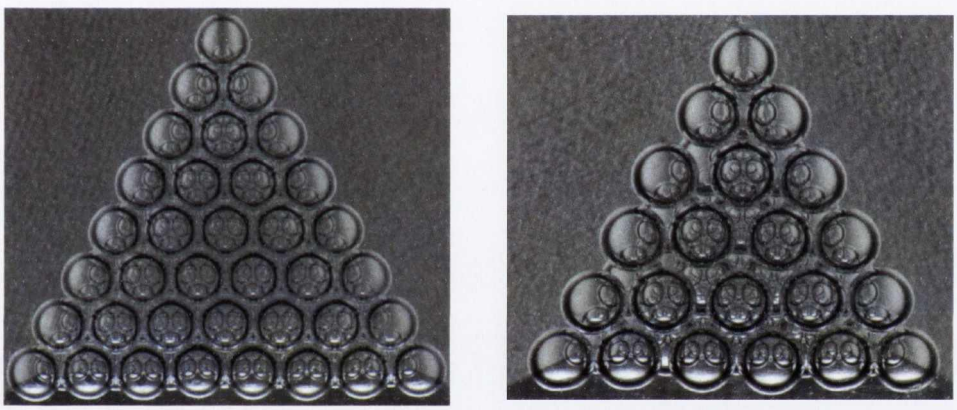

Figure 5.11: Images showing the arrangements of bubbles in three sided pyramids of vertex angles 65° and 75°. The bubbles within the 65° pyramid appear to arrange into the defect-free strained fcc crystal as seen for a 60° pyramid (see Fig.5.4). The bubbles in the 75° pyramid still conform to strained fcc structure.

Fig.5.11 shows the ordering of monodisperse microbubbles of approximately 1 mm in diameter in such pyramids. (The cases of bubbles ordering within 60° and 90° pyramids have been discussed separately in the sections on fcc and sc crystallisation.) The 65° pyramid produces a fcc lattice, with no obvious defects observed in our largest sample, 12 layers deep, composed of roughly 350 bubbles. In the 75° pyramid, the bubbles again appear to order

Structure	Observed plane	Current Max no. bubbles	Comments
fcc	{111}	500	Successful for all sizes reported here.
bcc	{100}	140	Successful for dry Currently unstable foams due to comp ity of bubbles. Furt periments with smal bles may be successf
sc	{111}	18	Unstable for both w dry foams.
Twinned fcc	$\{1\frac{1}{2}\frac{1}{2}\}$	500	Successful generat twinning defect.
Bidisperse	{111}	12	Currently limited t crystals

Table 5.1: Summary of experimental results.

into an fcc lattice. However, on comparison with the ordered crystals produced from the 60° pyramid, it is noted that the interbubble distance in each layer is now greater than the bubble diameter, making subsurface bubbles visible. This corresponds to the formation of a face-centred orthorhombic crystal structure [92]. Bubbles in the 85° pyramids formed crystals which closely resembled those produced in the 90° pyramid associated with the sc lattice.

5.4 Conclusions

Through selective choice of the vertex angle of three and four sided pyramid containers, we have directed the crystallisation of monodisperse foams into fcc,bcc and sc configurations, albeit with limited success for bcc and sc, as yet. A summary of the experimental results is shown in table 5.1.

We have seen that in the most promising case, that of fcc, monodisperse foam grown in an appropriate pyramid can produce perfectly ordered foams

across a wide range of bubble sizes. Bcc and sc are more problematic, in that instabilities are unavoidable. Nevertheless, with more carefully controlled experiments, and smaller bubbles, we expect to extend these experiments considerably, since confined growth tends to suppress instability.

We found that the generation of fcc crystals was robust against strain imposed by small changes in the vertex angle.

We have shown that this method may be easily adapted to the generation of ordered bidisperse foams as well as the selective generation of defects within otherwise perfect crystals.

This methodology may easily be scaled upwards for practical applications, allowing for the selective crystallisation of metallic, ceramic and polymer foams. For such applications we intend to investigate the ordering behaviour of these monodisperse microbubbles under forced drainage conditions. The forced continuous flow of surfactant solution through the apex of a pyramid during the filling procedure would replace the shaking of the samples that we currently apply to produce coherent crystals.

Finally, our ability to precisely control the three-dimensional structure of monodisperse foam samples, combined with new tomographic techniques [72], will allow us to greatly expand the original programme of Bragg which was to elucidate the structure of ordered and defective materials with a system visible to the naked eye.

Chapter 6

Formation of columnar crystals in wet foam systems.

Figure 6.1: Graphic showing the ordering of monodisperse microbubbles within a cylindrical tube. The bubbles are seen to order in a regular, repeating structure. The nature of these ordered cylindrical packings will be examined in this proceeding chapter.

The ordering of spheres within cylindrical confinement is found to be a non-trivial and important packing problem. First studied computationally, such structures have been found in a variety of physical systems. In this chapter, we investigate these ordered structures using monodisperse microbubbles (see Fig.6.1).

6.1 Introduction

Fcc crystal structures are seen to be the most efficient packings for *unbounded* three dimensional systems [93]. Within the atomic structures of solids, the crystallisation of nanoparticles, the arrangement of colloidal spheres and the crystallisation of foams in the wet limit, the fcc structure is readily seen to occur [21, 60, 94, 95]

However, the question which the fcc structure addresses - which is the most efficient packing of spheres - only provided a universal answers for the specific case of an *unbounded* packing. For more realistic case of a *bounded* packing, the limitations of the border may result in the pure fcc lattice being no-longer the most efficient packing structure. Although it is possible for the boundary of such a finite packing to be chosen to match the symmetry of a particular crystal structure (see Chapter 5) in general, this will not be the case. In these cases, an "alternative" structure must be formed.

These alternative structures may take the form of a random arrangement of spheres [45], or a crystalline lattice with the addition of specific defects - such as dislocations, grain boundaries etc. [72]. However, for certain extreme cases, the most energy efficient structure diverges significantly from the fcc configuration of the bulk. One particularly rich and interesting example of such boundary conditions resulting in unique crystal structures occurs when spheres are confined in cylindrical tube of similar internal dimensions.

Present in various physical systems, the first systematic approach to this problem was conducted by Pickett*et. al.* in 2000 [96]. By conducting simulated annealing of frictionless hard spheres in cylindrical confinement, Pickett found the minimum energy configuration of hard spheres of diameter d when placed in a cylindrical tube of internal diameter D. By dividing these two lengths, a non-dimensional parameter $\lambda = \frac{D}{d}$ may be defined to describe the system. On increasing λ from the minimum possible value of 1, at which value the system consists of a linear chain of spheres, Pickett found that the optimum packing structures migrated through a series of chiral and non-

chiral ordered phases. In addition, it was found that the packing fraction of spheres ϕ varied in a non-linear fashion as λ is increased (see Fig. 6.2).

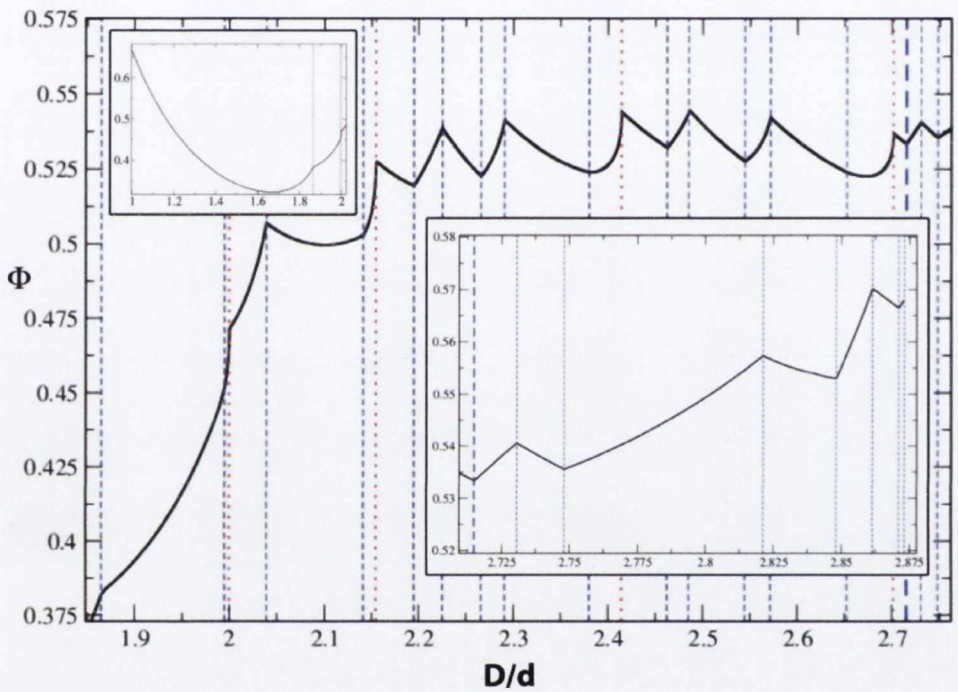

Figure 6.2: Graph showing the variation of packing fraction ϕ against $\frac{D}{d} = \lambda$. As λ is increased. Figure reproduced with permission from Mughal *et. al* [97]

Following the initial study of Pickett, the theoretical basis of the packing problem was finally unwrapped by Mughal *et al.* in 2011 [98]. They determined that each of these *columnar crystals* may be described by a periodicity vector, V, which links equivalent spheres within the structure. Unwrapping the cylindrical centre positions of the sphere within the packing results in a pattern of points which, when combined with the periodicity vector can be extended to produce a infinite 2D lattice of points. Each structure may then be categorised by the type of deformation of a regular 2D hexagonal lattice

required to replicate the sphere-packing lattice.

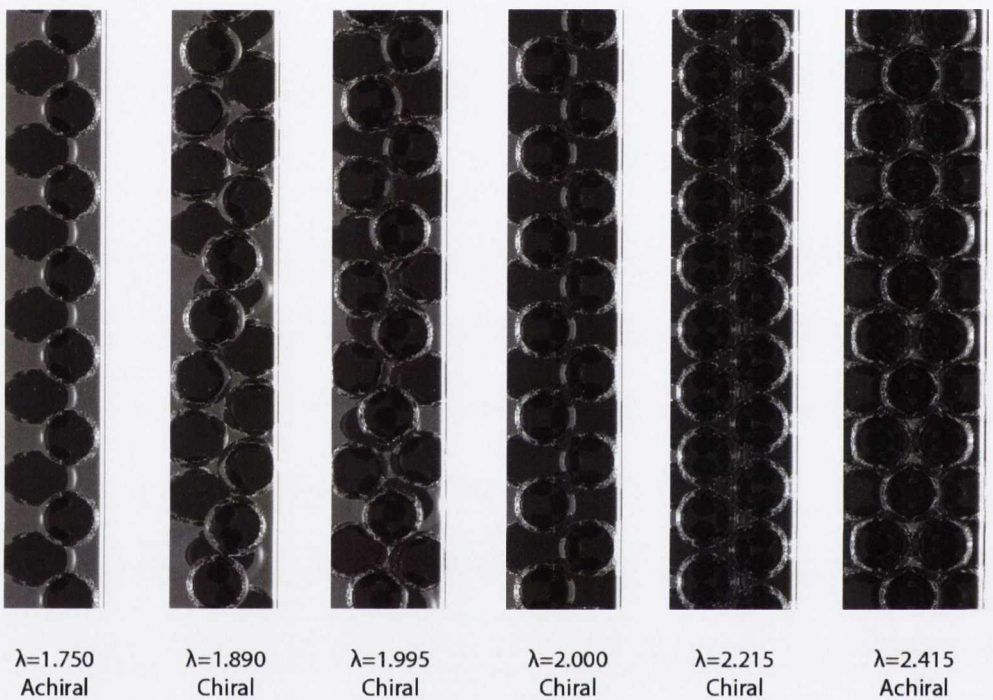

Figure 6.3: Examples of optimum cylindrical packings generated from simulated annealing for several values of λ, represented as bubbles within a glass capillary. Images generated from simulation data provided by Mughal *et al.* [99] and generated using *POV-Ray* [70].

Those structures which require no deformation i.e. whose periodic vector fits onto a regular hexagonal lattice, are called *symmetric structures* (example: $\lambda = 2.000$ in Fig.6.3). Those structures which require a localised strain of the lattice are know as *line slip* structures [98] (example: $\lambda = 2.215$ in Fig.6.3). The theoretical basis of Mughal *et. al.* may be used to understand a wide variety of systems in which the ordering of spherical particles within cylindrical geometries occurs.

One of the most interesting examples of these cylindrical systems was studied by Hodak and Girifalco. Using Monte Carlo methods, the minimum energy arrangement of C_{60} particles with diameter of 6.27 $\mathring{A}$ within cylindrical nanotubes of varying width was studied[100]. Although the potential between the particles differed significantly from the excluded-volume interaction, as employed by Pickett and Mughal, it was found that the ordering properties of the system was very similar to the hard sphere model for low λ value. On increasing λ, the ordered structures produced are seen to diverge from the results of simulated annealing.

Tymczenko *et. al.* investigated the ordering characteristics of polystyrene spheres of diameter 1 μm inside the cylinder-like pores of a silicone membrane [101]. Again, although the system interactions differed significantly when compared to an ideal hard sphere system, the two systems were seen to exhibit the same ordering behaviour for low λ values and independent of the boundary conditions used.

We believe that wet foams offer the ideal system with which to study these cylindrical packing of spheres. Previously, Weaire *et al.* demonstrated that a wide variety of ordered dry foam structures are seen to spontaneously occur if monodisperse bubbles of average diameter roughly 1 cm are introduced into a cylindrical tubes of diameter of the same order (see Fig.6.4) [102]. Each structure may be defined by a number λ, equal to the tube diameter divided by the average bubble diameter, and may be characterized through the use of phyllotactic notation[1]. Such ordered structures were also seen to spontaneously occur within tubes of square and triangular cross-sections

[1] For each ordered structure, the surface layer of the foam is composed of a hexagonal grid of cells. This allows the structures to be categorised through the use of phyllotactic notation, first developed to describe the distribution of leaves around the branches and stems of plants. By unwrapping the surface structure so as to form a hexagonal gird, in a similar fashion as that employed by Mughal *et. al.*, a set of basis vectors may be defined [102]. By decomposing the vector V linking identical cells into this basis, the number of each lattice vectors l and m may be calculated. These two numbers, along with their sum n, are then used as a triplet (l,m,n) to describe the resulting cylindrical structure.

[103, 104].

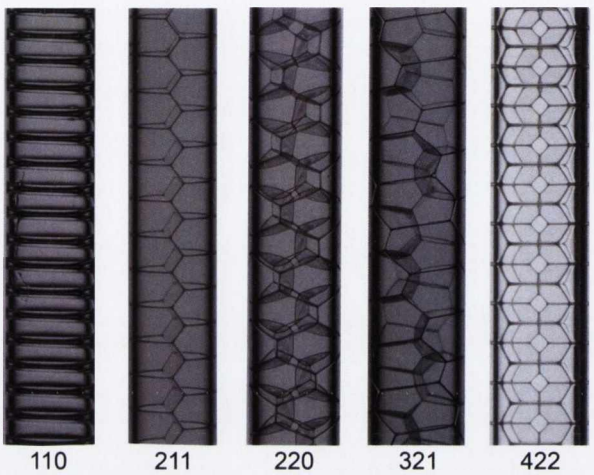

Figure 6.4: Monodisperse bubbles of average diameter roughly 1 *cm* are seen to spontaneously order under cylindrical confinement. Each structure is labelled using phyllotactic notation.

By making such cylindrical dry foams wet, the resulting structures resemble the previously discussed hard-sphere cylindrical packings (see Fig.6.5). If we employ monodisperse microbubbles bubbles in such experiments, a good approximation to the ideal hard sphere system of Pickett *et al.* and Mughal *et al.* may be expected in the limit of small bubble radius. This is due to the limited friction which exists within foam systems and the scaling of the bulk modulus, K, of a bubble to the radius r as $\frac{1}{r}$ [1].[2] As the bubble

[2]The bulk modulus of a material is the resistance of that material to compression. It is given by $K = -V\frac{\delta P}{\delta V}$, where V is the volume of the object, δP is the pressure change. For the case of an isolated spherical bubble $V = \frac{4}{3}\pi r^3$ and $P = \frac{4\gamma}{r}$ where γ is the surface tension of the liquid phase. Inserting these parameters into the equation for the bulk leads to

$$K = \frac{4\gamma}{3r}. \tag{6.1}$$

This leads to $K \propto \frac{1}{r}$.

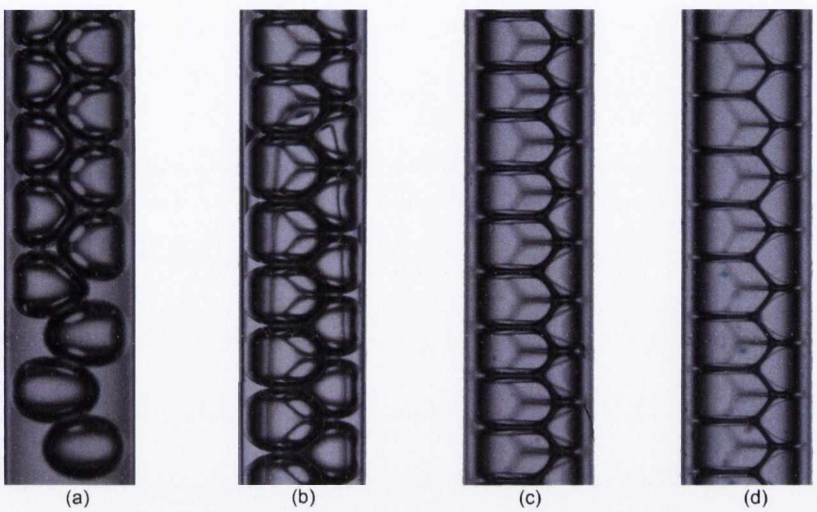

Figure 6.5: A monodisperse foam, of average bubble diameter 1.2 mm, producing a λ =1.5. (a) Near the foam-liquid interface the structure, is seen to resemble a packing of spheres of the same λ value. As the distance form the foam-liquid interface is increased (b) - (d), the liquid fraction of the foam is decreased and the polyhedral nature of the foam increases. A direct comparison between the foam structure and the hard-sphere experiments is then not possible.

diameter is decreased the bulk modulus increases, leading to the bubble becoming more hard-sphere-like. The negligible contact friction which exists between the bubbles allows the foam to spontaneously produce the maximal volume-fraction state without requiring the annealing necessary to generate similar structures in hard-sphere systems [105]. For this reason, they form the ideal system to study the optimum packing of spheres within cylindrical geometries.

Two sets of experiments were conducted to determine the ordering behaviour of monodisperse microbubbles within a cylindrical geometry and how they compare to similar hard-sphere systems: Firstly, by introducing

monodisperse microbubbles into glass capillaries, we attempted an optical characterisation of their structure. Following this, we used X-ray tomography to characterise their internal structure within cylindrical polymer containers.

6.2 Optical experiments

Our optical experiments involved the ordering of monodipserse microbubbles within thin glass capillary tubes, of internal diameter of the order of 1 mm. The capillaries were formed from glass tubing, initially of internal diameter 1 cm and length 15 cm. The tubes were heated to melting point using a bunsen burner, at which point they were stretched by hand, the final length of the hollow glass filament determining its internal diameter. The glass filament was then cut into 5 cm long pieces. The capillary tubes were photographed from both ends, their internal diameter and circularity were then measured using *ImageJ*. [3] Tubes whose circularity was above 0.85 and whose diameter varied less than 1% along the tube length were then used for our packing experiments.

Monodisperse microfoam was produced using a flow focusing device, as described in Chapter 2. The foams were produced from nitrogen gas and 5% by volume aqueous solution of commercial detergent *Fairy Liquid*. Once produced, the foam sample was collected in a petri dish. The sample was then illuminated from below using a planar back-light and imaged from above. The bubble diameter was calculated by measuring the centre-to-centre bubble distance in a 2D hexagonal array. A characterised tube was placed into the foam layer, the capillary action of the surfactant solution drawing the bubbles into the tube. The tubes were then mounted either horizontally or vertically. The filled tube was photographed using a *Canon EOS 50 D* DSLR camera

[3] Circularity is a measure of the divergence of two-dimensional shape from that of a perfect circle [50]. It is defined as $C = \frac{4\pi A}{P}$ where A is the area of the object and P is the perimeter of the object [50]. For a perfect circle, C=1, but this value decreases as the circular nature of the object decreases.

combined with a 190mm macro lens and 15 cm bellow extension, which allows high-resolution optical images.

From the optical images, the packing fraction ϕ may be calculated as follows, assuming that the bubbles are both spherical and incompressible. For N bubbles of radius r, ordering within a cylindrical tube of radius R, we obtain

$$\phi = \frac{\frac{3}{4}\pi N r^3}{\pi R^2 h},$$

where h is the length of the foam sample being examined. Using the relation $\lambda = \frac{r}{R}$ this leads to:

$$\phi = \frac{3N\lambda^2 r}{4h}. \tag{6.2}$$

The packing fraction of the cylindrical packing may then be calculated by measuring the number of particles N per unit length h within the wet region of the foam. The optical distortion of the bubble packing by the glass of the capillary tube made determining the exact location of bubbles difficult. This increased the error associated with our packing fraction data.

6.2.1 Results

It was seen that the cylindrical foam structure strongly depended on the orientation of the capillary tube with respect to gravity. We thus examine the horizontally and vertically orientated capillary tubes separately:

6.2.1.1 Horizontal tube experiments

When mounted horizontally, the resulting "height" of the foam column with respect to gravity is, at most, equal to the diameter of the containing cylinder. It is therefore easy to ensure that the entire foam column remains wet, increasing the number of bubbles that may be included when determining the packing fraction of the system. The packing fraction results for the ordering

of microbubbles within a horizontally orientally capillary tube are shown in Fig.6.6.

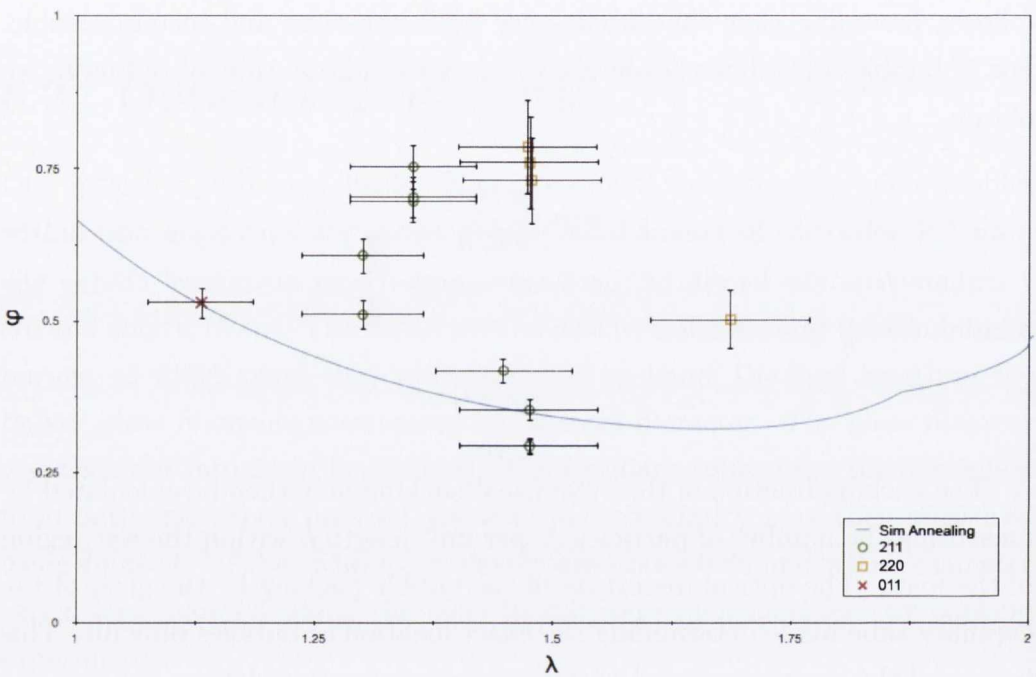

Figure 6.6: Variation of the packing fraction ϕ with λ obtained from experiments using monodisperse microbubbles in horizontal capillary tubes. The continuous line refers results of simulated annealing from this range of $\lambda = \frac{r}{R}$ [106].

It is seen that the experimentally obtained values for volume fraction reside far above the expected volume fraction of hard sphere packings as several experimental values also resided above $\phi = 0.74$, the upper-bound for hard-sphere packings in three dimensions. In addition, the structures observed occur at λ values not expected from the hard sphere simulations. For example, 220 structure was found at $\lambda = 1.5$, where simulated-annealing experiments predict such a structure for $2 \leq \lambda \leq 2.039$ [99].

The differences between this experimental system and simulation is due,

in part, to the horizontal orientation of the tube. Although advantageous producing a uniform liquid fraction along the foam, the horizontal orientation results in the buoyancy force of the bubbles being directed normal to the central axis of the tube. In this respect, the resulting system does not resemble the simulations of Pickett and Mughal in which the bubbles are forced together.

6.2.1.2 Vertical tube experiments

The experiments were repeated with the capillary tube now mounted vertically. The action of the buoyancy force along the long axis of the cylindrical tube now forces the bubbles together, reducing the inter-bubble distance. In this respect,the system now more closely resembles the hard-sphere model of simulated annealing, against which our experiments are compared.

Examples are seen in Fig. 6.7. For each experimental λ value, the resulting foam morphology now matches that expected from simulated annealing, however the experimental packing fraction still resides above that expected for hard-spheres, although it is closer to the theoretical results (see Fig.6.6). Again, this is due to the finite compressibility of the bubbles. The experiment was repeated for samples of several different bubble diameters. It was seen that variation of bubble diameter did not produce a measurable difference in packing fractions using this experimental method.

6.3 Tomographic experiments

Due to the optical distortion of the glass tube and the problem associated with determining the spacial limit of individual bubbles, it was decided to characterise the packings using X-ray tomography. This method of characterisation has several advantages over previous optical experiments. Firstly, due to the lack of refraction of X-rays from the wall of the cylindrical container, the optical distortion of the samples is no-longer a concern. Secondly,

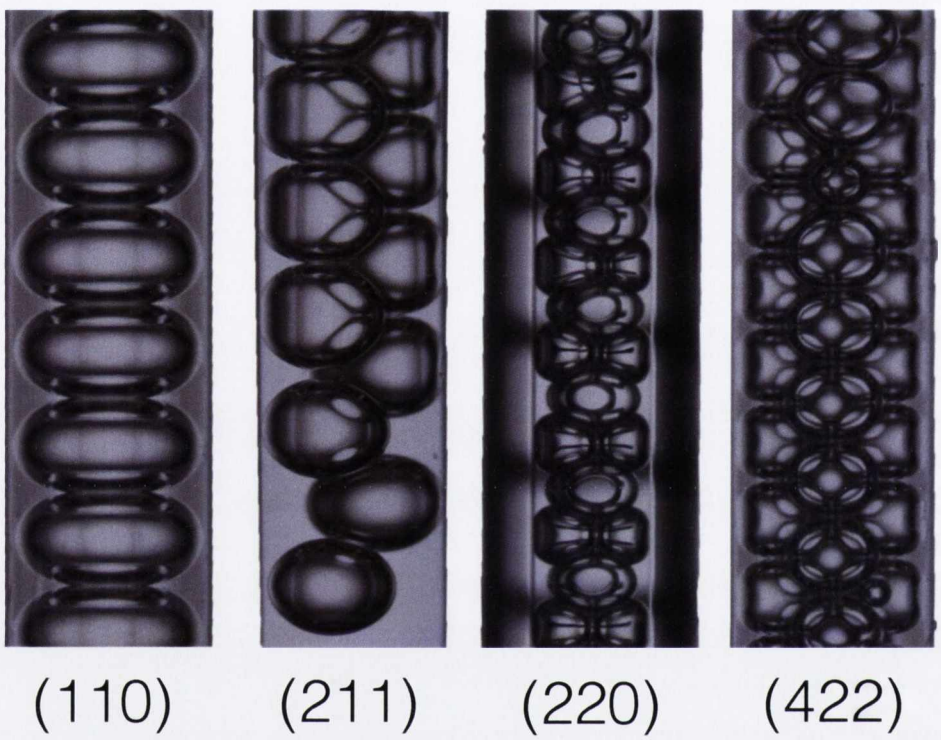

Figure 6.7: Examples of the 110, 211, 220 and 422 structures formed using bubbles of diameter approximately 1 mm,

due to the increased spacial resolution available from this method, we may greatly increase the accuracy of our packing fraction calculations. We may also calculate the contact number distribution for each packing. In addition, this method allows us to examine high λ value packings, whose many layers of internal bubbles may not be studied accurately using optical techniques.

6.3.1 Experimental method

Monodisperse foam was produced using the flow-focusing setup shown in Fig. 2.2. The bubbles were then loaded into a container fabricated using

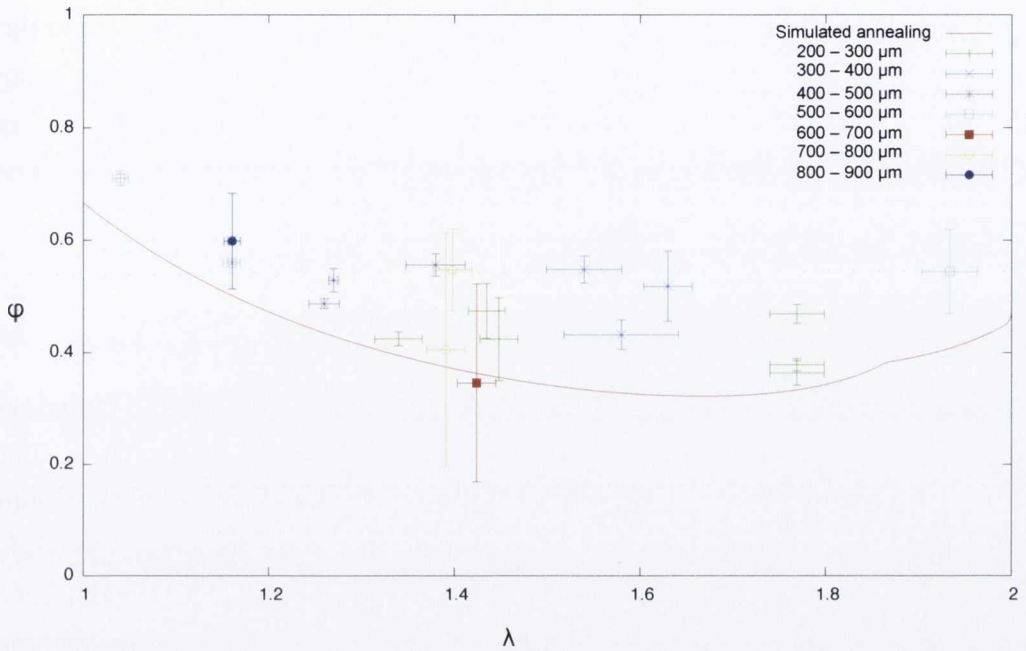

Figure 6.8: Variation of ϕ against λ for a vertically mounted capillary tube. It is seen that the experimental packing fraction resides above those values associated with simulated annealing. This is due to the finite compressibility of the foam sample.

an *Object Eden 3D* printer, described in section 4.1.1. The container was composed of a polymer block in which 26 separate cylindrical chambers were formed (see Fig. B.2). The holes ranged in diameter from 0.8 *mm* to 3.3 *mm* in 0.1 *mm* intervals. This allows 26 cylindrical packings of different λ values to be imaged at the same time. The container was placed in a surfactant solution (%5 by volume fraction aqueous solution of *Fairy Liquid*) and inverted to remove trapped air. A syringe was used to inject surfactant into each cylindrical chamber to remove any additional trapped air bubbles. The container was then moved over the outlet of the flow focusing device. Once sufficiently filled with bubbles, the container was tapped lightly to help

crystallisation. The outlet of the container was closed by sliding a glass plate over the open face of the container. The resulting system was then mounted on a polyurethane plinth and allowed to rest for two hours before being imaged. This allowed the system to settle, allowing for successful imaging of the sample. The tomographic data was then processed using the *Octopus* software as described in Chapter 2.

A collection of the resulting foam structure is shown in Fig.6.9. 5 cylinders of diameter 2.9, 3, 3.1, 3.2 and 3.3 *mm* are shown (left to right), with smaller tube diameters visible behind. Each bubble on the exterior of the foam sample may be resolved. Fig.6.9 (B) shows the top of the foam sample while Fig.6.9 (C) shows the bubbles near the foam-liquid interface. As the distance from the foam-liquid interface is increased, the bubbles are seen to become more polyhedral in nature, corresponding to a dryer foam.

In Fig.6.9 A it is seen that as the distance form the foam-liquid interface increases, the structure of the foam structure changes. This structural change may be explained by the compression of bubbles within the foam column by the buoyancy force of the underlying foam layers. This results in the effective bubble diameter *decreasing* as a function of height from the foam-liquid interface. This provokes the change in foam structure as a function of distance from the foam-liquid interface h. During our later analysis of these foam structures, we limited our investigation to those bubbles within a height H_w of the foam-liquid interface, defined by equation 1.2 in section 1. By focusing on this region, we guarantee that our foam sample may be considered wet, while avoiding the added complication of a structural change along the foam sample.

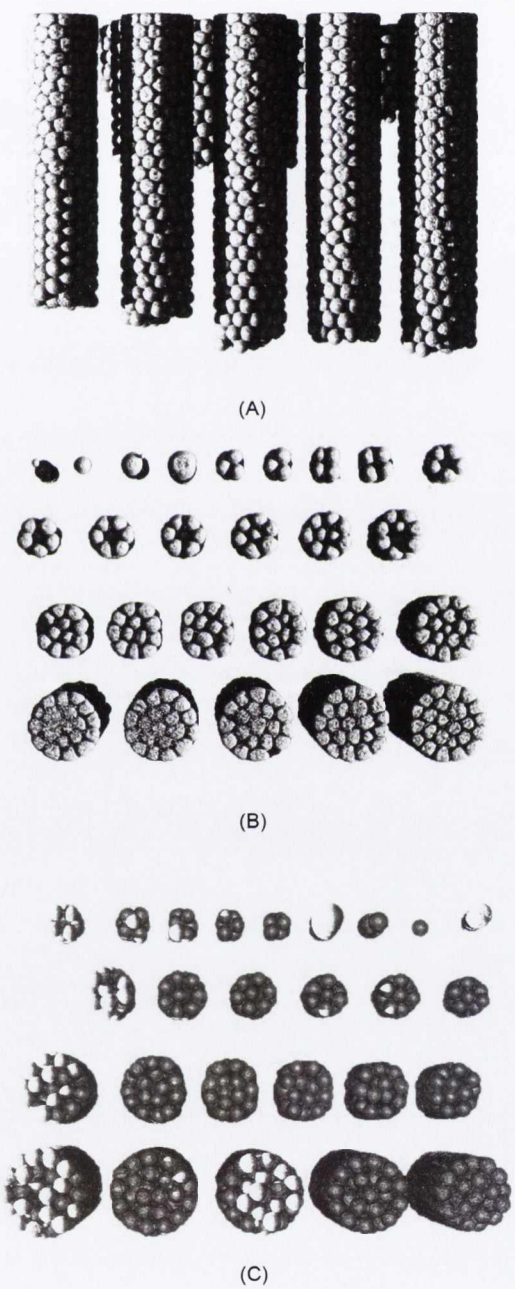

Figure 6.9: Reconstruction of the raw three-dimensional tomographic data showing the ordering of microbubbles within the cylindrical chambers. Several different viewpoints of the foam are shown, including (A) profile shot, (B) the top of the foam and (C) the bottom of the foam near the foam-liquid interface.

Note that an attempt was also made to analyse the structure of dry foams far from the foam-liquid interface using our tomographic data. However, it was found that due to the reduced liquid content of this foam, X-ray contrast was not sufficient to preform a usable segmentation of this data (see Fig.6.3.1).

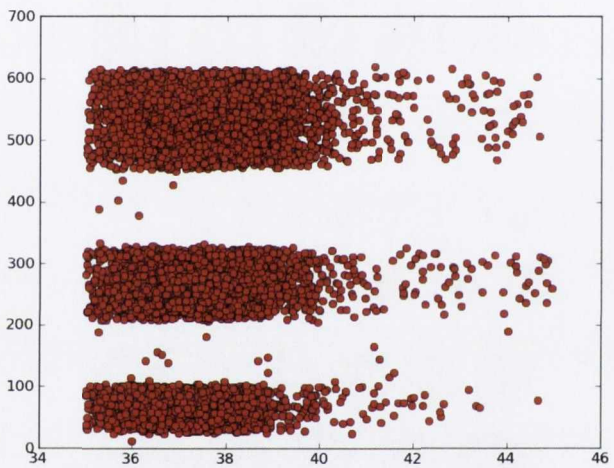

Figure 6.10: Plot showing the xz coordinates of the bubble center positions obtained from the data segmentation. It is seen that the density of bubble-center positions decreases dramatically far from the foams-liquid interface. The is due to our inability to successfully segment dry foam using our current X-ray tomography setup.

6.3.2 Data processing

Following the imaging of the foam sample, the data was processed to extract the bubble center positions as described in section 2 using *MAVI*. The average bubble size was calculated by fitting a Gaussian to the distribution of bubble diameters (see Fig. 6.11).

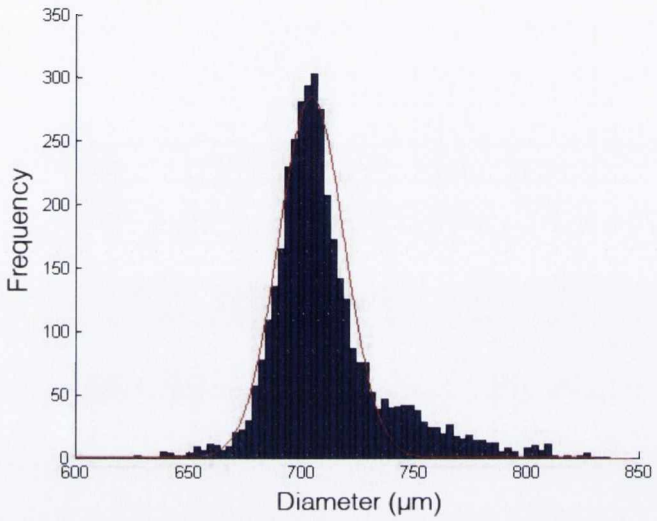

Figure 6.11: Histogram of bubble diameter distribution for a typical sample used in the cylindrical foam experiment. The resulting distribution was fitted to a Gaussian, resulting in an average bubble diameter of 720 $\pm$ 40 μm yielding a polydispersity of 5 %, thus identifying the sample as monodisperse according to the definition laid out in section 1.

Once a sample had been verified as monodisperse, the bubble center position data was then segmented to assign each bubble to a particular foam column. The xy center positions of each bubble within the sample was plotted and a rectangular grid was overlaid to aid in this segmentation process (Fig. 6.12).

6.3.3 Results

After successful segmentation of the positional data of the bubbles, the foam columns were analysed under three separate criteria.

- Cylindrical morphology

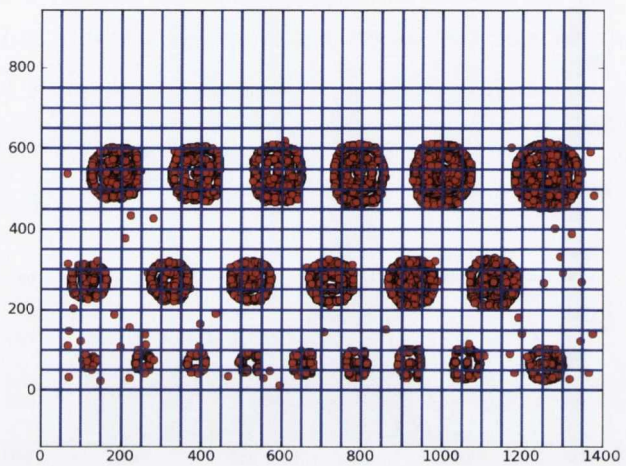

Figure 6.12: Partitioning of the experimental data. Red points indicate the bubble center position. The blue rectangular grid, 50 pixels in width, serves as a guide for the manual segmentation of the experimental data. Image noise leads to a few stray particles outside of the columnar bubble structures.

- Packing fraction
- Contact number distribution

6.3.3.1 Cylindrical morphology

The bubble center positions were visualised using the freely available software *POV-Ray* [70]. Each bubble was represented by a sphere, the radius of which was equal to the radius of the corresponding bubble.

It was found that the experimental foam ordered into coherent structures close to the foam-liquid interface. The foam structures were broken into two categories. We call those structure for which all bubble of the sample are in contact with the container wall *low* λ *value* structures. Structures which contain internal bubbles, i.e. bubbles which are not in direct contact with

the boundary of the container we call *high* λ *value* structures.

6.3.3.1.1 Low λ For low λ values it was found that the resulting foam structures were well described by the results of simulated annealing. Fig.6.13 and Fig.6.14 show the comparison between two foam structures of similar λ values - 2.22 ± 0.01 and 2.24 ± 0.01. It is seen that the foam structure closely follows the results of hard sphere experiments. In particular, it is seen that a small change in λ value produces the same structural changes in both the foam and hard-sphere system.

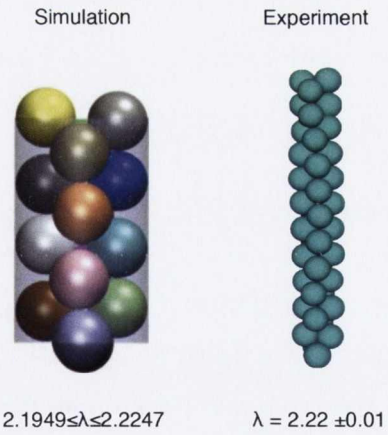

Figure 6.13: Comparison between the hard-sphere structure produced by simulated annealing and the foam experiment with a corresponding λ value of 2.22 ± 0.01. It is seen that both simulation and experiments show the same pairs of spheres rotated through 90°. Note the separation present between bubbles of each second layer of the structure.

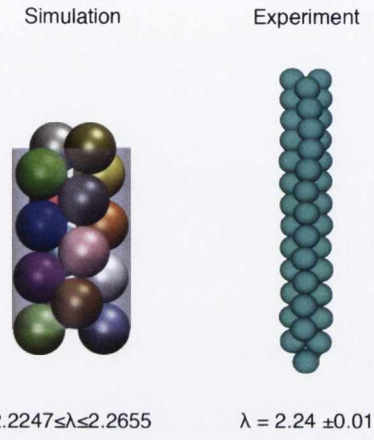

Figure 6.14: Comparison between the hard-sphere structure produced by simulated annealing and the foam experiment with a corresponding λ value of 2.24 $\pm$ 0.01. It is seen that both simulation and experiments show the same pairs of spheres rotated through 90°. Note that the bubbles that were separated in Fig.6.13 are now in contact.

6.3.3.1.2 Large λ An accurate determination of the exact onset of internal spheres is not possible from these tomographic experiments due to the inability to continuously measure the structural changes with increasing λ. However, we see that structures without internal spheres are seen up to λ = 2.5 after which the next successfully imaged structure, at λ = 2.9 shows the emergence of a structure with internal spheres. This range of λ values includes λ = 2.73, the value associated with the onset of internal spheres in simulated-annealing data [99].

The first of these foam structures with internal spheres is seen in Fig.6.15. Both the external and internal bubbles are seen to form ordered structures. For this structure (λ =3.13 $\pm$ 0.1) it is seen that the internal structure is composed of a series non-connected spheres. Results from simulated annealing show that a similar structure may occur for hard spheres, although at a

different λ value of $2.8711 < \lambda < 2.873$ [99]. As the λ value of the experiments is increased (Fig. 6.16 and Fig.6.17), it is seen that the ordered external and internal structures are seen to increase in complexity. In Fig.6.18 we see that the internal structure of the foam resembles a $\lambda = 2.215$ packing from the results of simulated annealing (see Fig.6.14).

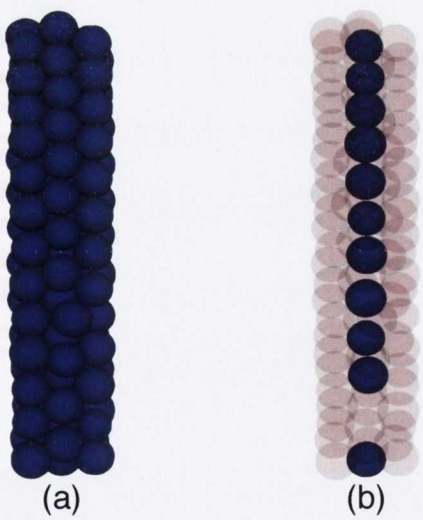

Figure 6.15: Foam structure of $\lambda = 3.13 \pm 0.1$. It is seen that the ordereded exterior foam structure (a) contains within it a series of disconnected internal spheres seen in(b)

Figure 6.16: Foam structure of $\lambda = 3.47 \pm 0.1$. The internal structure is seen to form a zig-zag structure.

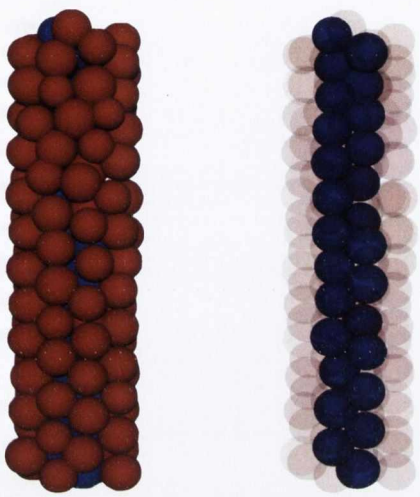

Figure 6.17: Foam structure of $\lambda = 3.66 \pm 0.1$. The internal structure is seen to form a closer-packed zig-zag structure.

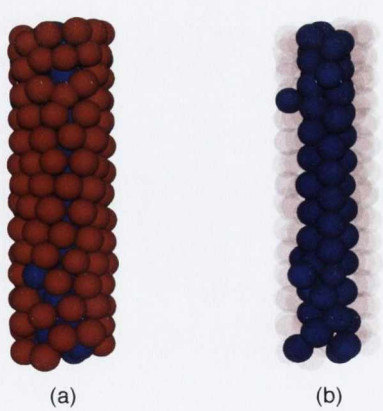

Figure 6.18: Foam structure of $\lambda = 4.19 \pm 0.1$. The internal structure is seen to resemble that of a $\lambda = 2.215$ structure.

On further increasing the λ value of the packing, it is found that a third layer of ordered bubbles may be found. Such a three-layered ordered foam structure is seen in Fig.6.19. As we remove the external layers of the foam sample, it is seen that each underlying foam layer is phyllotactic in nature. As the value of λ is increased, the internal structure of the foam is seen to change again. In Fig.6.20, it is seen that the increasing λ value results in the internal spheres of the packing coming into contact. Further simulations are required to study the exact transitions which occur within these systems as λ is increased. It is hoped that current experiments may form the seed for such simulation.

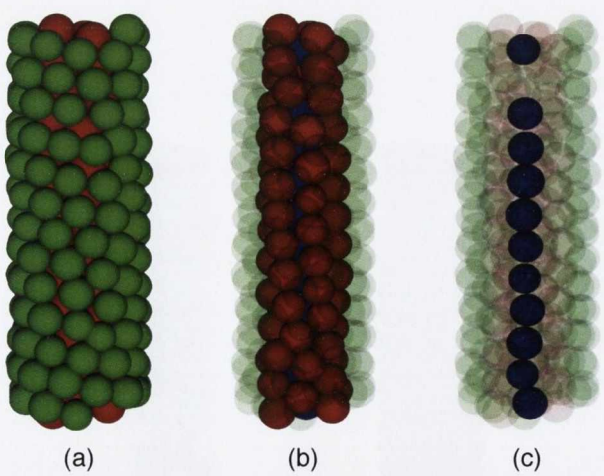

Figure 6.19: Visualisation of the foam packing structure for $\lambda = 4.74$. Successive ordered layers of the foam sample are coloured green, red and blue. Each successive layer of the foam is seen to be ordered

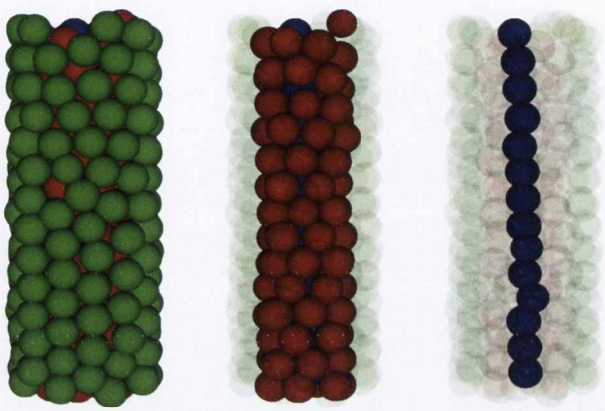

Figure 6.20: Visualisation of the foam packing structure for $\lambda = 5.14$. Successive ordered layers of the foam sample are coloured green, red and blue. Each successive layer of the foam is seen to be ordered

6.3.4 Packing fraction

From the positional and diameter data available for each bubble, we may more accurately calculate the packing fraction than possible from our previous optical measurements. In particular, we may take into account the effect of boundary bubbles on the resulting packing fraction.

Fig.6.21 shows a diagram of a packing of spheres, of radii r_i into a tube of radius D. The packing fraction for the system within a length H of tube may be written as

$$\Phi = \frac{\sum_{i=0}^{n} V_i}{\pi D^2 H} \tag{6.3}$$

where V_i is the volume of the i^{th} sphere within the tube length H and n is the total number of spheres being considered. There are three separate

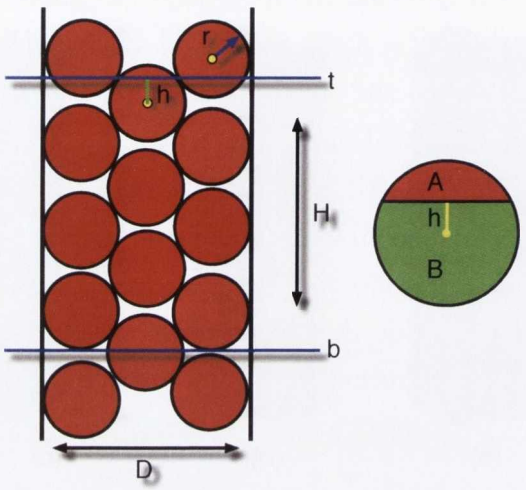

Figure 6.21: A diagram showing the packing of spheres, of radius r packed into a tube of diameter D. The packing fraction of the system is investigated in a section of length H.

cases for the form of this volume V_i. For those spheres which are completely contained within the tube section, the volume V_i is given as

$$V_T(r_i) = \frac{4}{3}\pi r_i^3. \tag{6.4}$$

For bubbles on the boundary of the tube element (i.e. $|z_i - t| < r_i$ or $|z_i - b| < r_i$ where z_i is the vertical coordinate of the i^{th} sphere, and t, b are the positions of the top and bottom of the tube section being examined) must be treated separately. The volume element V_i for such boundary spheres is given by either

$$V_A(r_i, h) = \pi\left(\frac{2}{3}r_i^3 - r_i^2 h + \frac{1}{3}h^3\right), \tag{6.5}$$

or

$$V_B(r_i, h) = \pi\left(\frac{2}{3}r_i^3 + r_i^2 h - \frac{1}{3}h^3\right), \tag{6.6}$$

depending on which section of the sphere is located within the tube element, as shown in Fig.6.21. Following these definitions of the volume associated with each sphere within the tube, the following rules can be written to determine each sphere's contribution to the volume fraction measurement.

1. For $|z_i - t| > r_i$ AND $|z_i - b| > r$ AND $b < z_i < t$, $V_i = V_T(r_i)$.
2. For $|z_i - t| < r_i$ AND $z_i > t$, $V_i = V_A(r_i, |z_i - t|)$
3. For $|z_i - t| < r_i$ AND $z_i < t$, $V_i = V_B(r_i, |z_i - t|)$
4. For $|z_i - b| < r_i$ AND $z_i > b$, $V_i = V_B(r_i, |z_i - b|)$
5. For $|z_i - b| < r_i$ AND $z_i < b$, $V_i = V_A(r_i, |z_i - b|)$

Using these rules, we may accurately calculate the packing fraction of each structure.

6.3.4.1 Results

The initial calculation of the packing fraction ϕ and λ using the tube radii obtained from the schematic shown in Fig.B.2 demonstrated several unusual results. On comparison with the simulated annealing results of Mughal *et. al.* [107], it was found that the wet foam structures diverged significantly from their hard sphere counterparts with, for example, a 422 foam structure occurring where a 110 hard-sphere structure is expected. Secondly, the calculated packing fraction resided high above the results of simulated annealing. Several experimental data points exceeded the maximum packing of 0.74 associated with fcc packing. In addition, several points were seen to reside above the physically unrealistic value of 1.

This discrepancy between the hard sphere simulations and the foam systems is due, in part, to the compressibility of the bubbles. However, due to the non-physical packing fractions above 1, we believe that the absorption of surfactant solution into the polymer from which the cylindrical containers

were produced played a significant role. This swelling of the polymer resulted in a reduction of the tube radius. Calculations based upon these decreased tube radii will result in artificially decreased λ and increased ϕ values. In addition, this swelling was found to result in the some of the cylinders becoming elliptical in cross section.

To combat these various problems,we fitted new tube radii to the distribution of points associated with each tube. This was done by first examining the distribution of bubble positions from the center of each tube (see Fig.6.22).

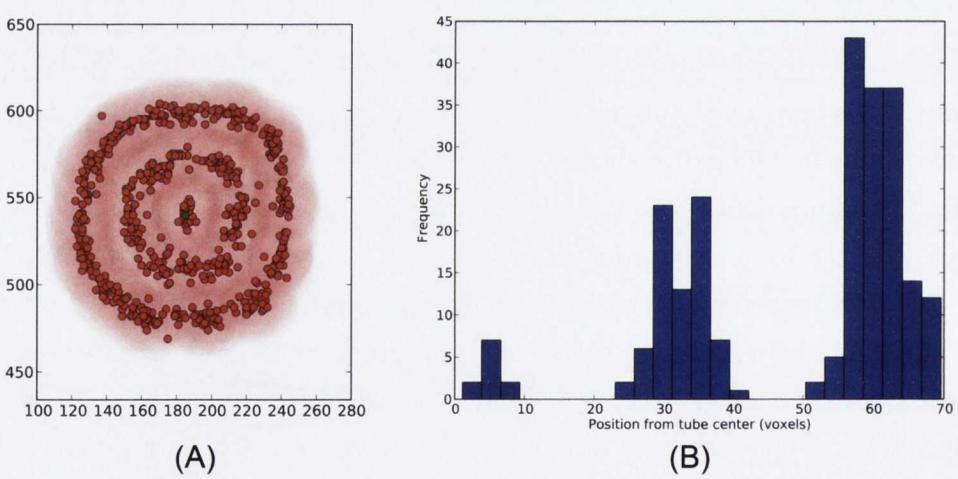

Figure 6.22: (A) plot showing the position of bubble centers within a cylinder and (B) a histogram of the bubble center positions. It is seen that the bubbles are arranged in concentric rings. The bubbles in the outer ring are used to determine a new tube radius for the system being examined.

Figure 6.23: Comparison between the fitted (left) and original (right) tube diameter. The center of each bubble is marked using a red point, while the extent of each bubble is shown by a light red disc. The center of the tube is marked in blue while the extent of the tube is shown in light blue. The fitted tube radius covers the extent of each bubble, while the original tube diameter suggests the extrusion of bubbles out of the cylindrical container.

Those tubes which were not found to be circular in nature were excluded from further analysis. The centres of the outermost peak of these histograms was used to fit a circle the diameter of which is used as the new tube diameter. It was found that this new tube diameters more realistically describe the packings, as seen in Fig6.23.

Upon successful calculation of the new tube radii, the packing fraction of the sample was again calculated and compared to the previously calculated packing fraction using the old tube radius. The comparison is shown in Fig.6.24.

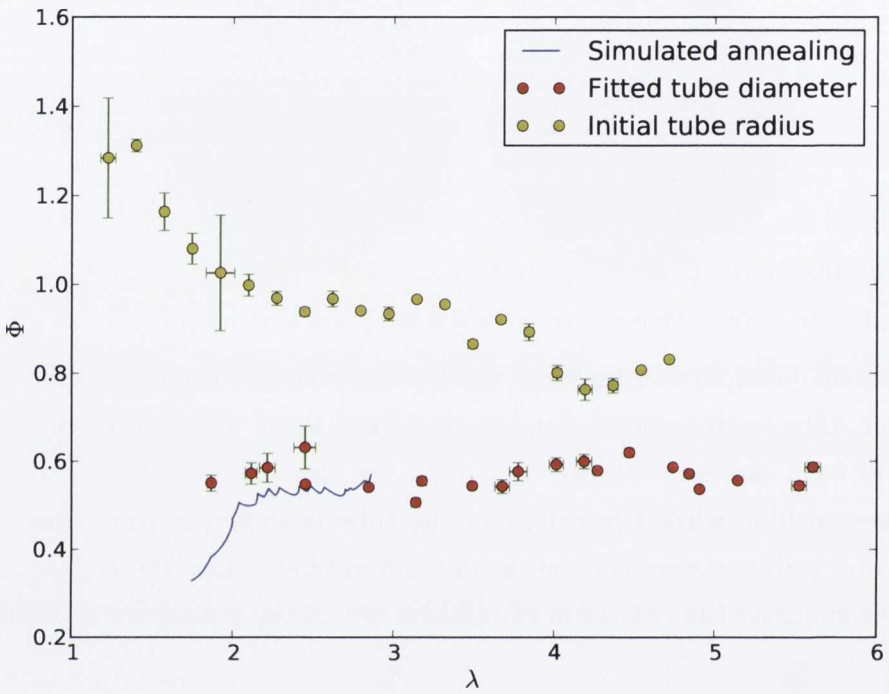

Figure 6.24: Comparison between the packing fraction as calculated using the initial tube radius (yellow) and the fitted tube radius (red). It is seen that the fitted tube diameter more closely follows the packings associated with simulated annealing.

The final packing fractions are shown in Fig.6.25. It is seen that the new packing fraction more closely follows the results of simulated annealing. The foam experiments overestimate the packing fraction associated with hard spheres, but this is due to the finite compressibility of the bubbles in the experiment.

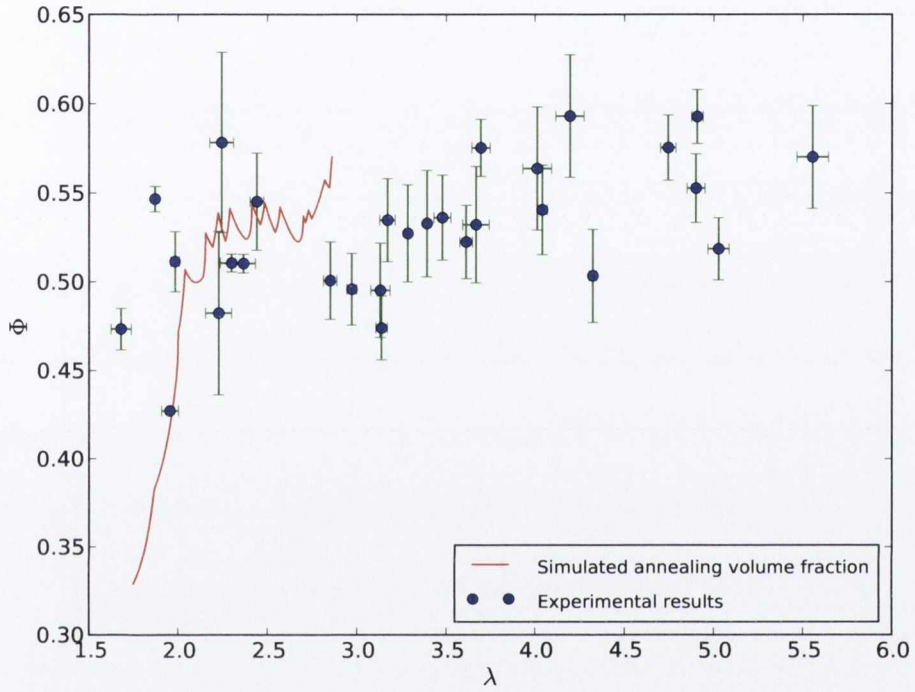

Figure 6.25: Comparison between the packing fraction as calculated using simulated annealing (continuous red line) and experimental foam packing data (blue points). It is seen that the experimental data lies roughly in line with the results of simulated annealing.

6.3.4.2 Contact number distribution

The contact number distribution was calculated for each experimental cylindrical packing. Again, the contact number for each particle was calculated using the conditions outline in section 1.2.1. The resulting contact number distribution is shown in Fig.6.26.

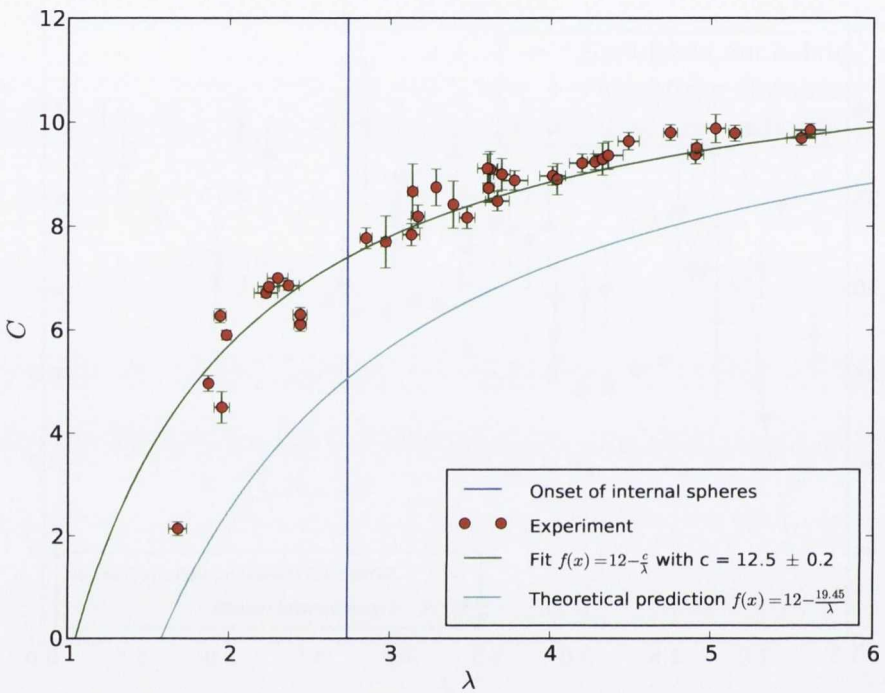

Figure 6.26: Variation of the distribution of the average number of contacts within the cylindrical foam structures with λ. It is seen that, as λ increases, the system approaches $C = 12$, the values associated with maximal contact number in three-dimensions. A theoretical prediction for the average contact number is shown in cyan, while our best experimental fit is shown in green.

It is seen that, as λ increases, the average contact number C increases as a function of λ, approaching $C = 12$ for large λ, the values associated with maximal contact number in three-dimensions. A simple theory may be put forward to describe the functional dependence of C on λ.

We examine an fcc lattice with a nearest neighbour separation of d. The density of points within this lattice ρ is given by

$$\rho = \frac{\sqrt{2}}{d^3}. \tag{6.7}$$

The density of *bonds* within this lattice ρ_B is given as

$$\rho_B = 6\rho = \frac{6\sqrt{2}}{d^3}. \tag{6.8}$$

On average, a plane, of angle ϕ and α with respect to an arbitrary normal vector $\vec{z}$, will cut N bonds per unit area where

$$\begin{aligned} N &= 2d\rho_B \cos\theta \cos\alpha \\ &= \frac{48\sqrt{2}}{(\pi d)^2} \end{aligned} \tag{6.9}$$

Averaging $\cos\theta$ and $\cos\alpha$ between 0 and $\frac{\pi}{2}$. A cylinder of length l and diameter D inserted into an fcc lattice will cut N_c bonds given by

$$N_c = \left(\frac{48\sqrt{2}}{(\pi d)^2}\right)(\pi D l) \tag{6.10}$$

The number of internal bonds within this cylinder is given by

$$\frac{\pi D^2 l}{4}\rho = \frac{\pi D^2 l}{2\sqrt{2}d^3} \tag{6.11}$$

The number of internal contacts of each sphere is given as

$$\begin{aligned} C &= 12 - \frac{\text{number of cut bonds}}{\text{number of spheres}} \\ &= 12 - \left(\frac{192}{\pi^2}\frac{d}{D}\right) \\ &\approx 12 - 19.47\frac{1}{\lambda} \end{aligned} \tag{6.12}$$

In the limit of $\lambda \to \infty$, C will approach 12, the value associated with closed-packed structures. For lower λ values, the boundary of the sample is more important, leading to deviations from our theory. This is seen in Fig.

6.26 where the theoretical prediction is plotted alongside our experimental results. Our prediction underestimates the contact number distribution for each λ value, however the deviation between theory and experiment decreases for increasing λ. A fit of our data (see Fig.6.26) to the expression $C = 12 - A\frac{1}{\lambda}$ results in a good description of the data, with $A = 19.46 \pm 0.01$ as expected form our simple theory.

6.4 Conclusions

Both optical and tomographic experiments of small bubbles, within the wet foam limit, have been shown to correspond well to the result of simulated annealing for the optimum configuration of hard spheres within cylindrical confinement. In both cases the morphology of the foam packing are seen to closely resemble what is expected from simulated annealing. When the packing fractions of such packings was calculated, it was found that the optical foam experiments consistently overestimate the packing fraction expected for hard spheres, while the tomography results showed large scatter when compared to the results of simulated annealing. We believe that this is primarily due to the finite compressibility of the bubbles and the finite compressibility of the bubbles when compared to hard spheres. For large λ values, it is seen that a series of foam structures with one and two layers of internal spheres occurs. Each internal layer of bubbles is seen to be ordered, with their structure similar to those foam structures of lower λ value. From the positional available from our tomographic data, we were able to calculate the coordination number for our foam packing. It is seen that the resulting contact number distribution follows the functional form of a simple theory based on the average number of contacts within an ideal fcc lattice.

In future, we will investigate larger λ value structures using X-ray tomography through the use of bubbles of smaller bubble diameter. This will also allow us to more accurately determine if such bubbles more closely approach

the hard-sphere limit. Through the use of phase-contrast synchrotron radiation, will will also investigate the transition regime between wet and dry foams which is currently difficult to probe using optical techniques.

Chapter 7

Future work

We have seen that convenient, low-energy X-ray tomography may be used to successfully image wet, monodisperse foams. We have also demonstrated that, through careful selection of the boundary conditions of such foam samples, their internal structure structure may be controlled.

In the future, we hope to extend this work, focusing on the use of these foam structures as an analogy for atomic crystalline systems. In this way we will further extend the original work of Bragg, providing new, exciting and fruitful insights into crystal structures and dynamic atomic processes [21]. Our current experimental setup allows us to capture features of the order of 30×10^{-6} m when successfully reconstructing a sample composed of bubble 700×10^{-6} m in diameter. In precious experiments, it has been shown that 700 μm bubbles the may be used to quantitatively model the behaviour of atomic copper systems [22]. This is due to unique scaling behaviour of the inter-bubble potential with the bubble radius directly to the atomic scale. If we, similarly, scale the resolution of our current 3D imaging technique we see that we can achieve a modelling resolution of roughly 9×10^{-12} m, comparable to current leading AFM setups, yet in fully-resolved 3D. This makes our experimental method one of the highest resolution, most economical methods of examining crystalline behaviour in three dimensions. In particular,

we will aim to conduct the first experimental particle-resolved indentation experiments.

7.1 Nanoindentation

Nanoindentation is a method of determining the physical characteristics of a material based upon the pressing of a hard tip, of defined geometry, under small load into the substance being tested [108]. The Bragg bubble model has been successfully used to model the nanoindentation process in two dimensions [26, 27, 109]. However, there are many three-dimensional crystalline defects which do not have a two-dimensional counterpart, and therefore cannot be explored with current methodology. We aim to produce the first indentation experiments into a three-dimensional bubble crystal. We have already conducted a preliminary experiment in which a Berkovich style indenter (see Fig.7.1) is forced into an ordered bubble pile composed of 2000 bubbles of average diameter 700 μm.

Using our current imaging X-ray tomographic technique, we found that we can successfully image these foam samples, as shown in Fig.7.2.

Through the use of a stepper motor and force gauge, we will repeat this experiment in a quasi-static indentation experiments. By imaging after each indentation increment, we will be able to chart the various structural changes which occur as the crystal is deformed. In particular we will, for the first time, be in a position to investigate the nucleation of subsurface defects within a perfect crystal lattice in three dimensions.

Due to the high resolution of our imaging techniques, the deformation of each bubble will be measurable. From these deformations, we may calculate the local stress within our sample as is currently performed in analogous two-dimensional experiments [110]. This will allow the stress distribution within an experimental indentation experiment to be measured locally for the first time.

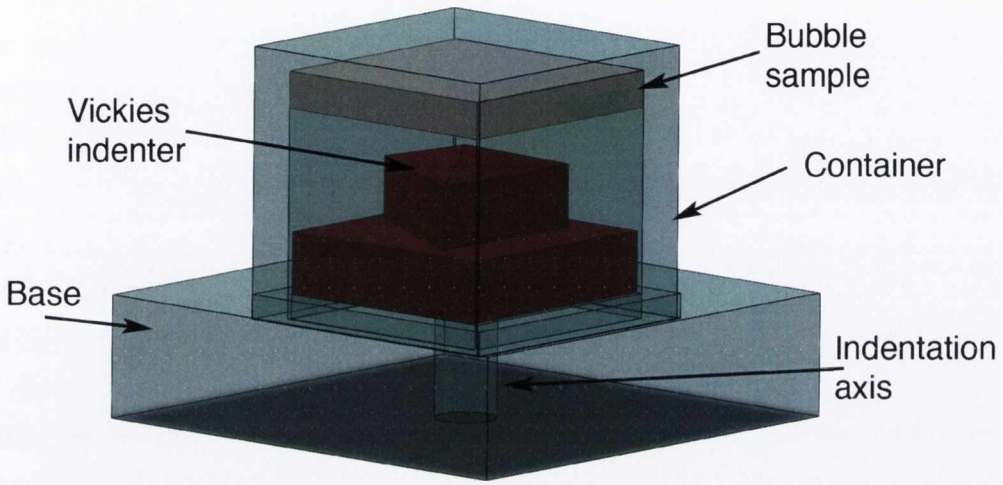

Figure 7.1: Sketch of the experimental setup used to conduct the first indentation into an ordered bubble pile. In our experiments, we used a small foam sample (composed of 5000 bubbles of average diameter 700 μm) into which is indented a Vickies style indenter.

Using the advances we have made in directed crystallisation, we will investigate how indentation dynamics depend on the crystal structure of the solid under investigation. Such a study is not possible in two dimensions where only one structure – a hexagonal arrangement of bubbles – is stable. We may, using the same techniques, study the dynamics of a grain boundary, or dislocation, and determine their effect on the load curve measured by the indentation tip. The flexibility and control permitted to us with this bubble model will allow us to tailor our experimental setup to study many real three-dimensional crystalline system.

7.2 Phase contrast synchrotron imaging

Our current imaging technique allows a rapid, cost-effective method of imaging wet foams samples, thus opening a wide frontier of experiments to be

explored. The success of this imaging technique is due to the increased X-ray absorption associated with the high liquid fraction of these foams. As we have seen in section 3.4, however, our imaging technique is not applicable to dry foam where sufficient sample absorption for producing a usable reconstruction is not available.

We may overcome this problem through the use of phase-contrast synchrotron imaging. This imaging method, based upon object reconstruction from the phase-change of a X-ray beam, provides higher-sensitivity than accessible by standard absorption based tomography [111]. This will enable us to study several interesting aspects of dry foams as well as to perform many dynamic experiments due to the high temporal resolution available at such facilities.

In particular, we aim to investigate the structural transition which occurs between an ordered fcc wet foam and an ordered bcc dry foam. We have already unsuccessfully tried to capture this transition region using our low-energy X-ray tomography method (discussed in chapter 4). Using phase-contrast tomography, however, we will repeat this experiment, allowing for the form of this transition to be imaged in three-dimensions for the first time.

The temporal resolution at these facilities will allow for the first topographic imaging of a sheared foam. The shearing of foam has been the subject of intense investigation as foams serve as a relatively easy experimentally accessible example of a complex fluid [112]. It is also found that microfoams represent an ideal system with which to study the glass transition, the shearing of polydisperse microfoams having been previously used to study the formation and mechanical properties of metallic glasses [113]. Although these experiments have been conducted in three dimensions, such studies have been limited to bulk characterisation of the foams due to the difficulties of imaging within the foam mass. As a result, the opportunity to link global behaviour to local dynamics is lost[114]. This has led to the restriction of most shearing experiments to two-dimensions where the resulting experimental images can

be processed to show such interesting phenomena as shear banding, vortices formation, etc. Using these high-energy imaging facilities we will be able to perform the first three-dimensional shear experiments with particle-resolved data. Such experimental data, without two-dimensional confinement, will allow direct comparison with a variety of physical models. In particular, we will be able to directly compare our experiments to recent theoretical work on the onset of the glassy phase in soft matter[115]. We will also investigate the shear behaviour of a coherent grain boundary, controlled through our work on controlled crystallisation section 5, providing the first experimental images of dislocation nucleation at a grain boundary, its propagation through an ordered crystalline structure, and its re-absorption into a neighbouring grain boundary. Such an analysis of this important dynamic process is not possible using other experimental techniques.

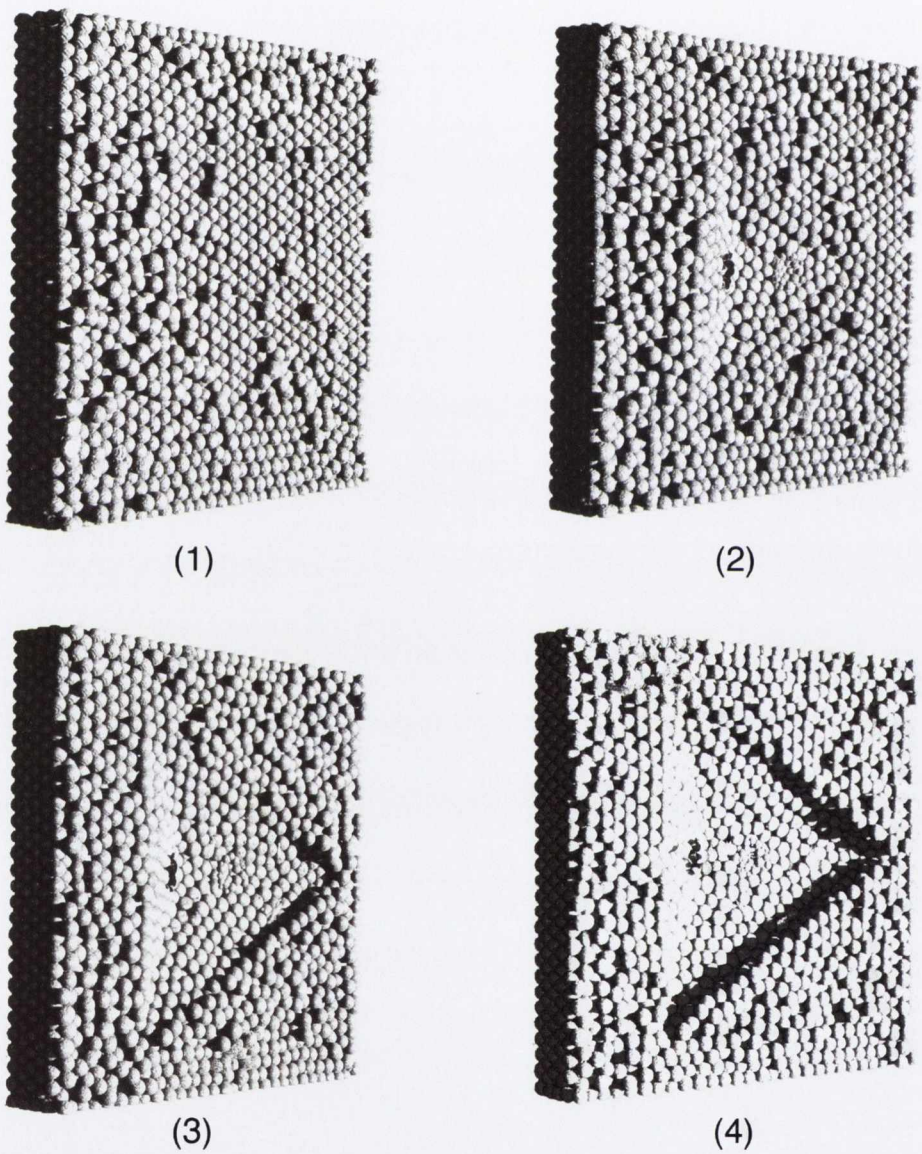

Figure 7.2: Reconstruction of a foam sample composed of bubbles of average diameter $800\mu m$ indented by a Berkovich tip. (1) shows the initial configuration of the bubble pile. (2),(3) and (4) show the same pile as the indenter tip progresses 0.5, 1 and 1.5 mm into the bubble pile.

Appendix A
Contact angle of surfactant solution on container wall

During our experiments, we wished to characterise the interaction of our surfactant solution with the surface of the polymer container used. To do this, we measures the contact angle of our surfactant solution (5% volume fraction detergent *Fairy Liquid* in water) on the surface of our container walls made from *Object verroclear*. The surface of our containers, however, is not completely smooth due to the nature of its production. This process involves the deposition of subsequent parallel layers of liquid polymer upon each other, each layer being cured through the use of a UV light source. This process allows for the creation of complex geometries, limited to a 20 μm vertical resolution. The resulting pieces have associated with them a surface roughness in all directions perpendicular to the plane of deposited polymer. The use of such surfaces would lead to large errors in any contact angle measurement.

To combat this problem, we printed a flat surface parallel to the deposition direction, leading to smooth surface. We then characterised the surface by measuring the contact angle of our surfactant solution on the polymer used to construct our containers. The contact angle was measured using the sessile drop technique. A single drop of surfactant solution was formed on the

surface of our container. The drop was photographed in profile, the resulting drop shape analysed using a sessile drop analyser plug-in for *ImageJ*[116]. An example of the experimental analysis is shown in Fig. A.1.

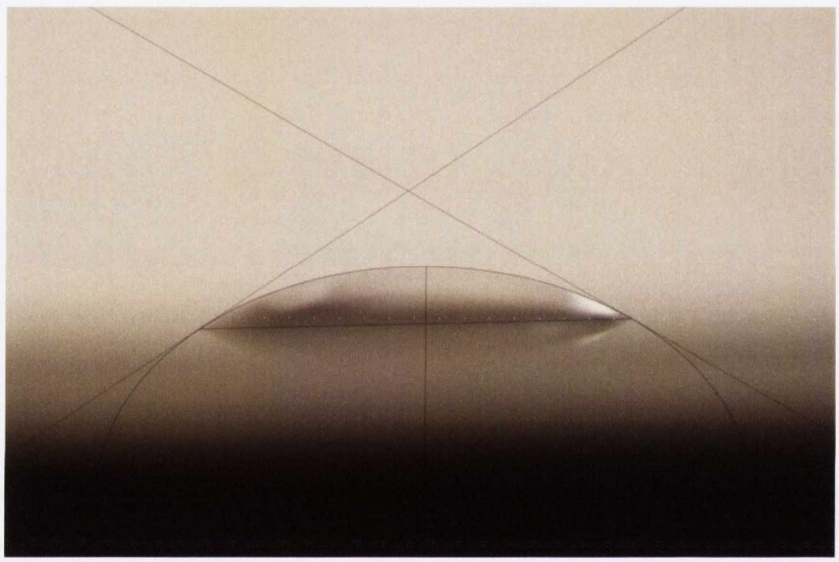

Figure A.1: Experimental images showing the formation of a drop on the flat surface of a typical experimental container. The drop profile was fitted using *ImageJ*. The resulting contact angle was approximately 33°.

Our measurements showed that the contact angle for the surfactant solution on the Object Veroclear polymer was 33° ± 5°. This contact angle is in keeping with previous measurements of contact angle for the surfactant solution on glass. However, it is noted that similar ordering experiments have been conducted using a variety of different plastics and glasses. It was seen that this did not effect the ordering behaviour of the bubbles [16].

Appendix B
Schematics

The following schematics were produced using the commercially available software *Solidworks* [79]. Once the schematics were produced, the structures were printed using an Objet Eden 250 3D rapid-prototype machine capable of accurately producing object features between 20-80 μm in size.

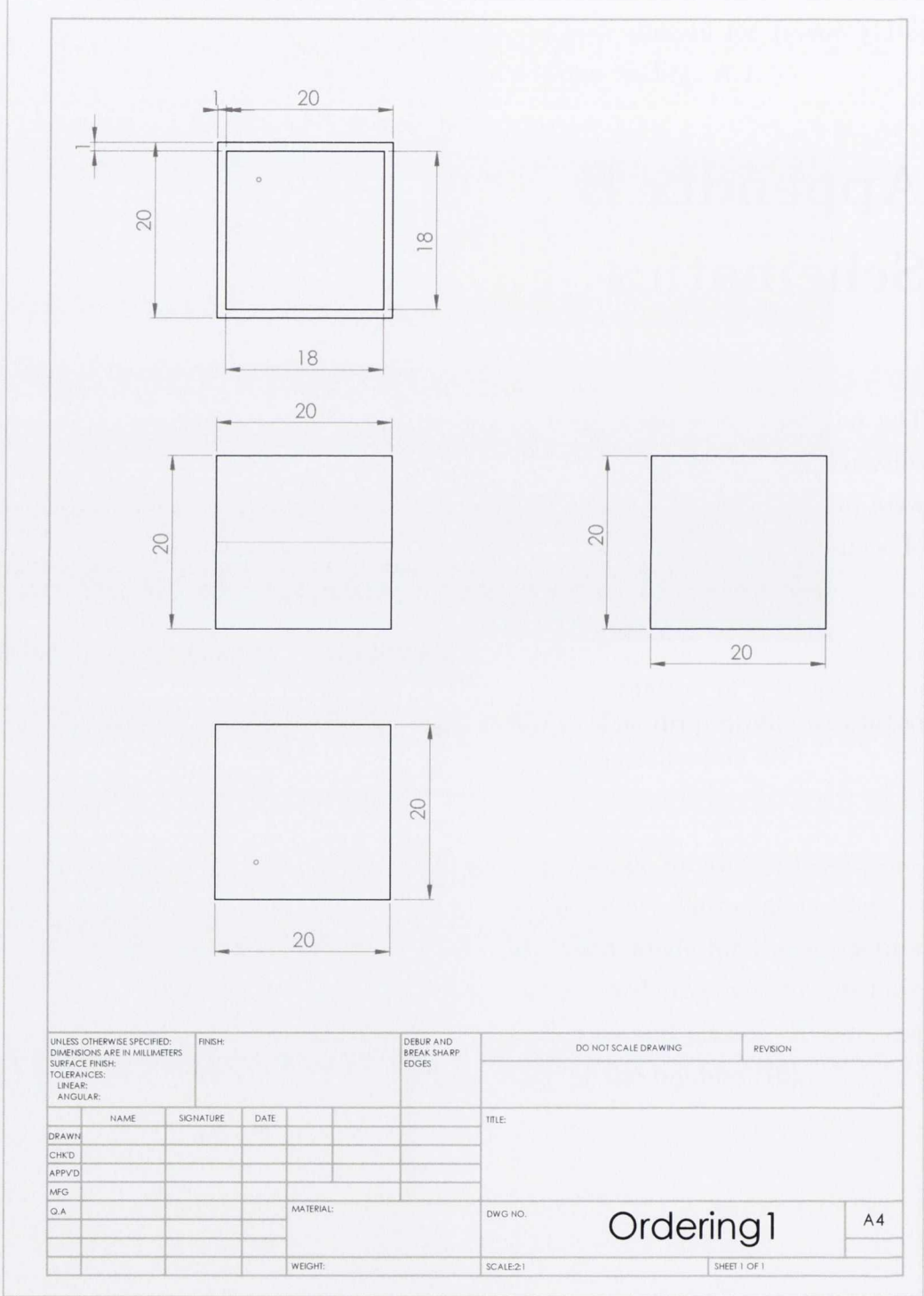

Figure B.1: Schematic for the simple rectangular container

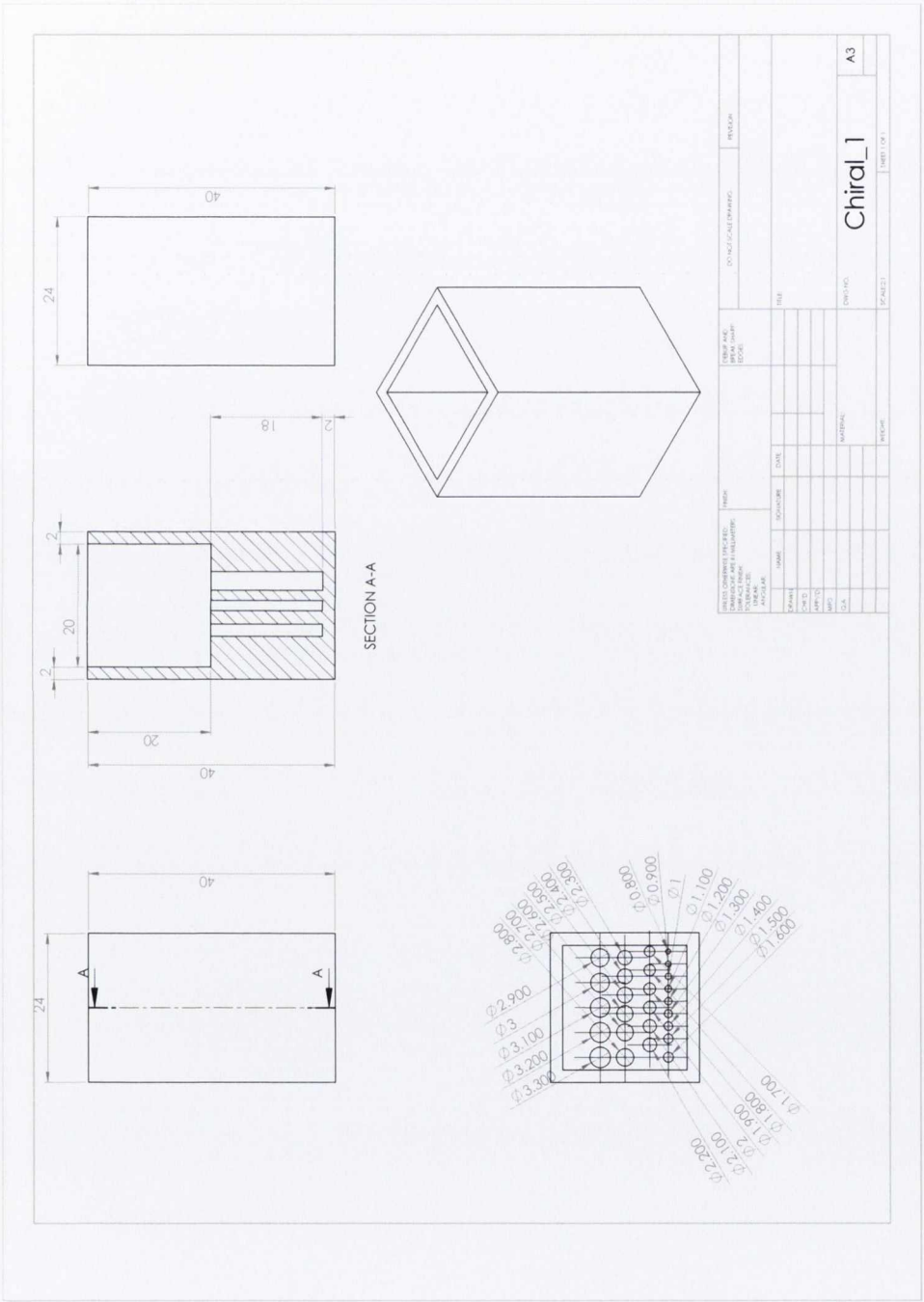

Figure B.2: Schematic of the template used for the generation of cylindrical foam structures imaged with X-ray tomography. The device is composed of 26 number of cylinders of diameter ranging from 0.8 to 3.3 mm in 0.1 mm intervals.

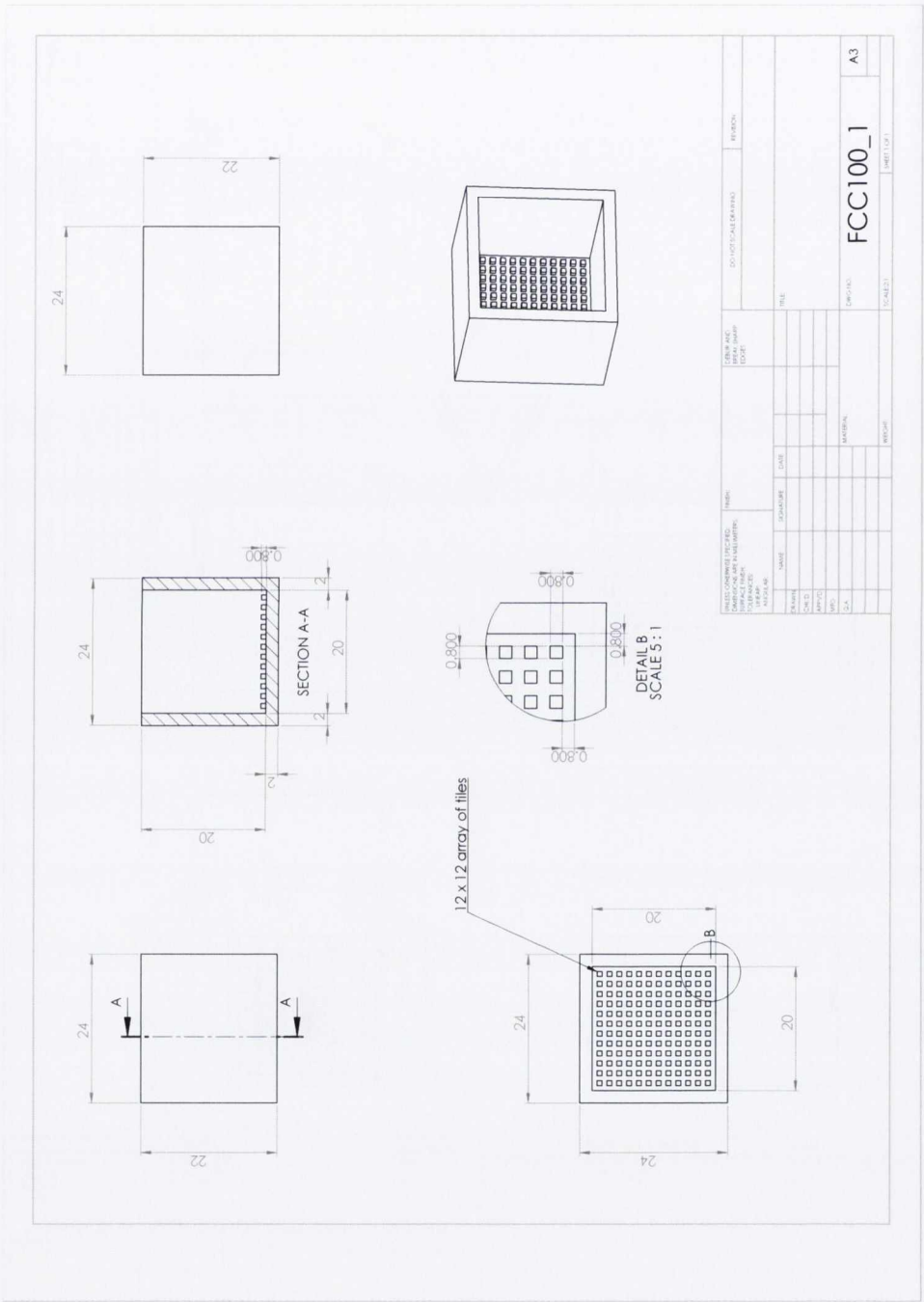

Figure B.3: First template for generating fcc ⟨100⟩ orientated crystals.

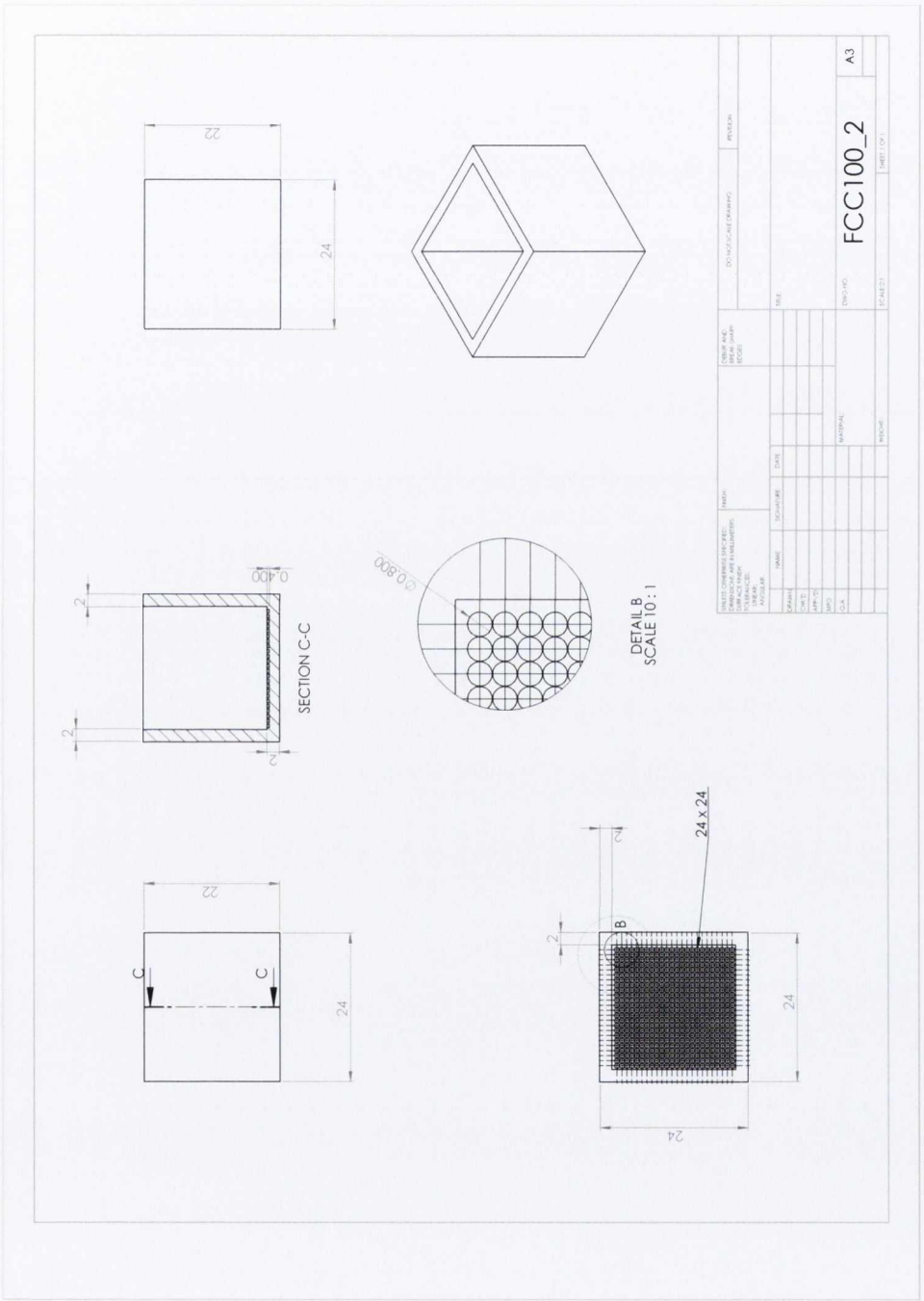

Figure B.4: Second template for generating fcc ⟨100⟩ orientated crystals.

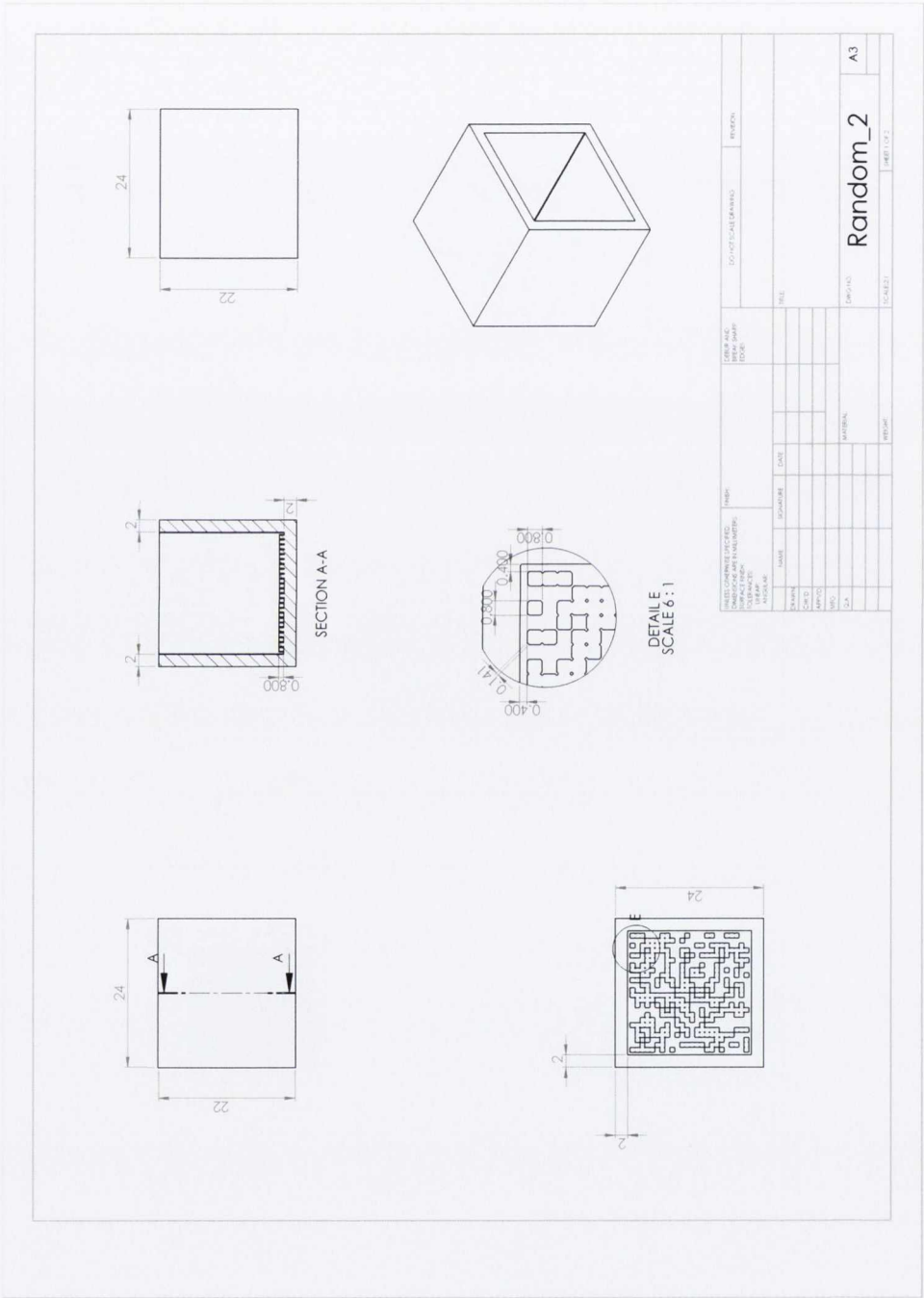

Figure B.5: Template used to examine the effect of roughness on sample crystallisation

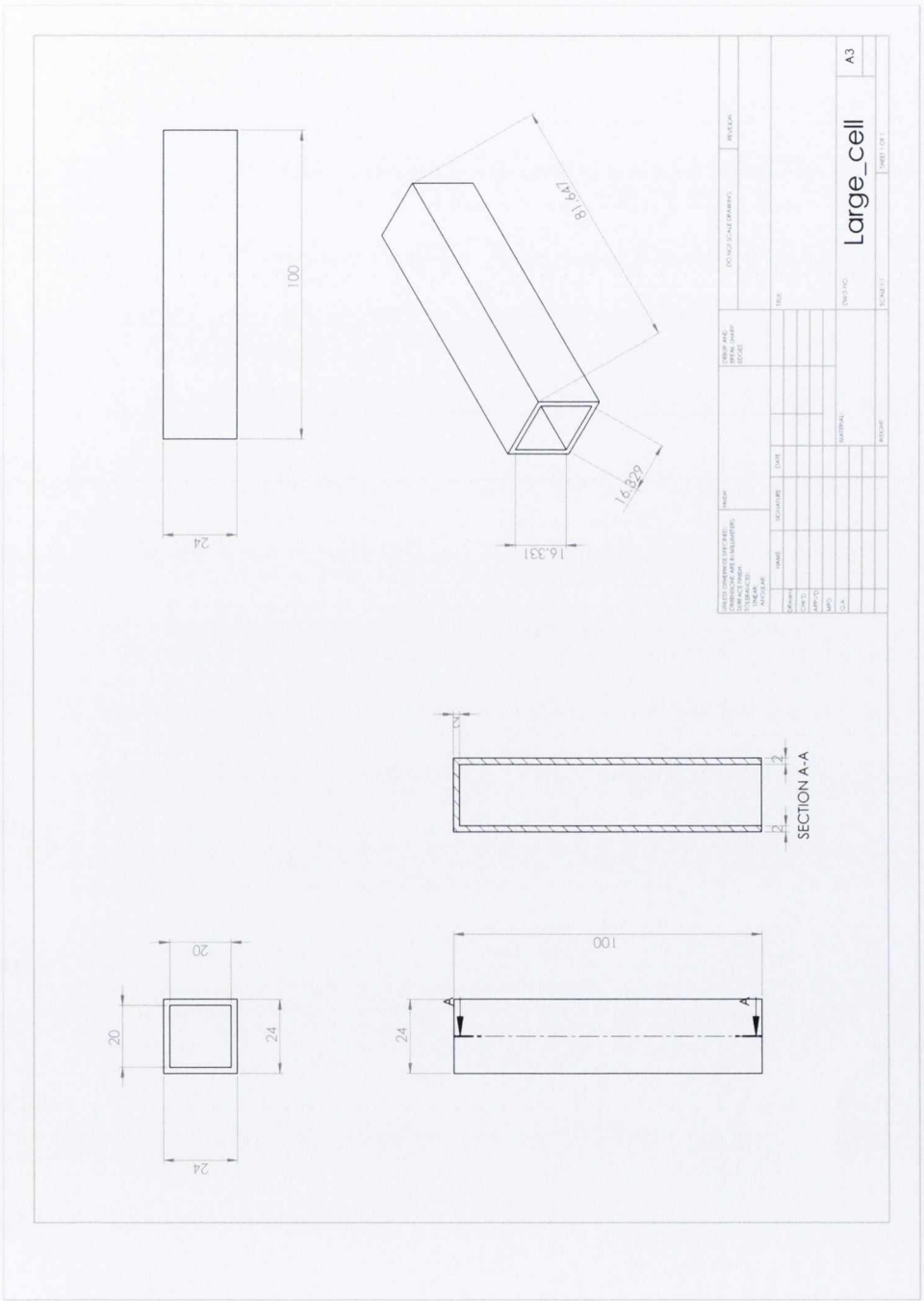

Figure B.6: Template used for examining fcc to bcc transformation.

Glossary

CT Computer Tomography.

Dodecahedron A polyheadron with twelve flat faces.

Grain boundary The interface between two distinct regions of crystallisation .

Hele-Shaw cell A sample container composed of two parallel pieces of flat glass, separated by a small distance in the order of millimeters .

Interstices A crystalline defect formed from the occurrence of an object at a previously unoccupied lattice site.

Lennard-Jones potential A simple mathematical model for the description of atomic interactions .

Packing fraction The ratio of the volume of the packing substance, to the entire volume of the packing structure.

Plateau border The meeting point of three foam surfaces.

Vacancies A crystalline defect formed from the absence of an object at a lattice site.

Vertex The meeting point of Plateau borders - central nodes of high liquid content within the foam.

Voronoi tesselation A Voronoi tesselation is a division of space based upon a distribution of points. Typically, such a division associates those regions of space which are closer to a particular point, as determined by a distance metric.

Bibliography

[1] D. Weaire and S. Hutzler. *The Physics of Foams.* Oxford University Press, Oxford, 1999.

[2] LJ Gibson. Mechanical behavior of metallic foams. *Annual review of materials science*, 30:191–227, 2000.

[3] S. Blacher, V. Maquet, R. Jérôme, J.-P. Pirard, and A.R. Boccaccini. Study of the connectivity properties of bioglass-filled polylactide foam scaffolds by image analysis and impedance spectroscopy. *Acta Biomaterialia*, 1(5):565 – 574, 2005.

[4] Sadoc J.F. and Rivier N. (eds.). *Foams and Emulsions,* Proceedings of the NATO Advanced Study Institute on Foams and Emulsions, Emulsions and Cellular Materials, Cargèse, Corsica, 12-24 May, 1997 . Kluwer Academic Puplishers, Dordrecht,Boston,London, 1999.

[5] R. Höhler, Y. Y. C. Sang, E. Lorenceau, and S. Cohen-Addad. Osmotic pressure and structures of monodisperse ordered foam. *Langmuir*, 24:418–425, 2008.

[6] P. Stevenson. *Foam Engineering: Fundamentals and Applications.* John Wiley & Sons, 2012.

[7] D. Weaire, N. Pittet, S. Hutzler, and D. Pardal. Steady-state drainage of an aqueous foam. *Phys. Rev. Lett.*, 71:2670, 1993.

[8] N Vandewalle, H Caps, G Delon, A Saint-Jalmes, E Rio, L Saulnier, M Adler, A L Biance, O Pitois, S Cohen Addad, R Hohler, D Weaire, S Hutzler, and D Langevin. Foam stability in microgravity. *Journal of Physics: Conference Series*, 327(1):012024, 2011.

[9] D. Barrett, E.J. Daly, M Dolan, S. Kelly S, W. Drenckhan, D. Weaire, and S. Hutzler. Taking Plateau into micro-gravity: the formation of an eight-fold vertex in a system of soap films. *Microgravity - Science and Technology*, 2008.

[10] J.A.F. Plateau. *Statique expérimentale et théorique des liquides soumis aux seules forces moléculaires.* Number v. 1 in Statique expérimentale et théorique des liquides soumis aux seules forces moléculaires. Gauthier-Villars, 1873.

[11] E.B. Matzke. The three-dimensional shape of bubbles in foam - an anlaysis of the role of surface forces in three-dimensional cell shape determination. *Am. J. Botany*, 33:58–80, 1945.

[12] A. M. Kraynik, D. A. Reinelt, and F. van Swol. Structure of random monodisperse foam. *Phys. Rev. E*, 67(3):031403, 2003.

[13] T. Aste and D. Weaire. *The pursuit of perfect packing.* Institute of Physics Publishing, 2000.

[14] D. Weaire and R. Phelan. A Counterexample to the Kelvin Conjecture on Minimal-Surfaces. *Philosophical Magazine Letters*, 69(2):107–110, 1994.

[15] O.Delgado-Friedrichs. The gavrog project. `http://gavrog.sourceforge.net`.

[16] A. van der Net, G. W. Delaney, W. Drenckhan, D. Weaire, and S. Hutzler. Crystalline arrangements of microbubbles in monodisperse foams.

Colloids and Surfaces A: Physicochemical and Engineering Aspects, 309:117–124, 2007.

[17] D. Weaire R. Phelan and K. Brakke. Computation of equilibrium foam structures using the surface evolver. *Exp. Math.*, 1995.

[18] Shailendra P. Joshi and K.T. Ramesh. Grain size dependent shear instabilities in body-centered and face-centered cubic materials. *Materials Science and Engineering: A*, 493(1–2):65 – 70, 2008.

[19] J. Kepler, J. Bromberg, and G. Bleichmar. *The Six-Cornered Snowflake*. Paul Dry Books, 2009.

[20] Thomas C. Hales. Historical overview of the kepler conjecture. *Discrete and computational geometry*, 36(1):5–20, 2006.

[21] L. Bragg and J. F. Nye. A dynamical model of a crystal structure. *Proc. Royal Soc. London Series A*, 190:474–481, 1947.

[22] L. Bragg and A. M. Lomer. A dynamical model of a crystal structure. ii. *Proc. Royal Soc. London Series A*, 196:171–181, 1949.

[23] W.M. Lomer. A dynamical model of a crystal structure. iii. *Proc. Royal Soc. London Series A*, 196:182–194, 1949.

[24] E. Fukushima and A. Ookawa. Observation of the grain boundary in soap bubble raft: 1. static feature of the grain boundary. *Journal of the Physical Society of Japan*, 8(5):609–614, 1953.

[25] M. M. Nicolson. The interaction between floating particles. *Proceedings of the Cambridge Philosophical Society*, 45(2):288–295, 1949.

[26] Andrew Gouldstone, Krystyn J Van Vliet, and Subra Suresh. Nanoindentation: Simulation of defect nucleation in a crystal. *Nature*, 411(6838), 2001.

[27] J. M. Georges, G. Meille, J. L. Loubetand, and A. M. Tolen. Bubble raft model for indentation with adhesion. *Nature*, 320(6060):343–344, 1986.

[28] A. van der Net, L. Blondel, A. Saugey, and W. Drenckhan. Simulating and interpretating images of foams with computational ray-tracing techniques. *Colloids and Surfaces A-Physicochemical and Engineering Aspects*, 309:159–176, 2007.

[29] A. van der Net, W. Drenckhan, D. Weaire, and S. Hutzler. The crystal structure of bubbles in the wet foam limit. *Soft Matter*, 2(2):129–134, 2006.

[30] G. D. Scott. Packing of equal spheres. *Nature*, 188(4754):908–909, 1960.

[31] Yang Jiao, Frank H. Stillinger, and Salvatore Torquato. Nonuniversality of density and disorder in jammed sphere packings. *Journal of Applied Physics*, 109(1):013508, 2011.

[32] J. D. Bernal. Geometry of the structure of monatomic liquids. *Nature*, 1960.

[33] J. L. Finney. Random packings and structure of simple liquids 1: Geometry of random close packing. *Proc R Soc Lon Ser-A*, 319(1539):479–&, Jan 1970.

[34] D. J. Durian, D. A. Weitz, and D. J. Pine. Multiple light-scattering probes of foam structure and dynamics. *Science*, 252(5006):686–688, 1991.

[35] C.P. Gonatas, J.S. Leigh, A.G. Yodh, J.A. Glazier, and B. Prause. Magnetic-resonance images of coarsening inside a foam. *Physical Review Letters*, 75(3):573–576, 1995.

[36] M. R. Fetterman, E. Tan, L. Ying, R. A. Stack, D. L. Marks, S. Feller, E. Cull, J. M. Sullivan, D. C. Munson Jr., S. T. Thoroddsen, and D. J. Brady. Tomographic imaging of foam. *Optics Express*, 7:186 – 197, 2000.

[37] Mavi - modular algorithms for volume images. `http://www.itwm.fraunhofer.de/en/departments/image-processing`.

[38] Wyart, M. On the rigidity of amorphous solids. *Ann. Phys. Fr.*, 30(3):1–96, 2005.

[39] J. Olafsen. *Experimental and Computational Techniques in Soft Condensed Matter Physics*. Experimental and Computational Techniques in Soft Condensed Matter Physics. Cambridge University Press, 2010.

[40] T. Egami and S.J.L. Billinge. *Underneath the Bragg Peaks: Structural Analysis of Complex Materials*. Pergamon Materials Series. Elsevier Science, 2003.

[41] J. Banhart. *Advanced Tomographic Methods in Materials Research and Engineering*. Monographs on the Physics and Chemistry of Materials. OUP Oxford, 2008.

[42] J. Ambrose and G. Hounsfield. Computerized transverse axial tomography. *Br. J. Radiol.*, 46(542):148–9, 1973.

[43] M. Tsukahara, S. Mitrovic, V. Gajdosik, G. Margaritondo, L. Pournin, M. Ramaioli, D. Sage, Y. Hwu, M. Unser, and Th. M. Liebling. Coupled tomography and distinct-element-method approach to exploring the granular media microstructure in a jamming hourglass. *Phys. Rev. E*, 77:061306, Jun 2008.

[44] Romeu A. Pieritz, Jörg Reimann, and Claudio Ferrero. 3d tomography analysis of the inner structure of pebbles and pebble beds. *Advanced Engineering Materials*, 13(3):145–155, 2011.

[45] T. Aste, M. Saadatfar, and T. J. Senden. Geometrical structure of disordered sphere packings. *Phys. Rev. E*, 71(6):061302, 2005.

[46] J. Lambert, I.Cantat, R. Delannay, A. Renault, F. Graner, J. A. Glazier, I. Veretennikov, and P. Cloetens. Extraction of relevant physical parameters from 3D images of foam obtained by X-ray tomography. *Coloids and Surfaces A: Physicochem. Eng. Aspects*, pages 295–302, 2005.

[47] J. Lambert, I. Cantat, R. Delannay, R. Mokso, P. Cloetens, J. Glazier, and F. Graner. Experimental growth law for bubbles in a moderately "wet" 3d liquid foam. *Phys. Rev. Lett.*, 99(5):058304, 2007.

[48] James A. Glazier. Grain growth in three dimensions depends on grain topology. *Phys. Rev. Lett.*, 70:2170–2173, Apr 1993.

[49] D. Weaire and V. Pageron. Frustrated froth: Evolution of foam inhibited by an insoluble gaseous component. *Philos. Mag. Lett.*, 62:417 – 421, 1990.

[50] J.C. Russ. *The Image Processing Handbook*. Image Processing Handbook. Crc Press, 2002.

[51] A. M. Ganan-Calvo. Perfectly monodisperse microbubbling by capillary flow focusing: An alternate physical description and universal scaling. *Physical Review E*, 69(2), 2004. Part 2 027301.

[52] P.B. Umbanhowar, V. Prasad, and D.A. Weitz. Monodisperse emulsion generation via drop break off in coflowing stream. *Langmuir*, 2000(16):347–351, 1999.

[53] M Dierick, B Masschaele, and L Van Hoorebeke. Octopus, a fast and user-friendly tomographic reconstruction package developed in labview. *Measurement Science and Technology*, 15(7):1366, 2004.

[54] A. Stocco, F. Garcia-Moreno, I. Manke, J. Banhart, and D. Langevin. Particle-stabilised foams: structure and aging. *Soft Matter*, 7:631–637, 2011.

[55] Autodesk. 3d studio max, www.autodesk.com/3dsmax, 2006.

[56] P. Soille. *Morphological Image Analysis: Principles and Applications*. Springer, 2010.

[57] Scipy. `http://scipy.org/`.

[58] Numpy. `http://numpy.org/`.

[59] S. T. Tobin, A. J. Meagher, B. Bulfin, M. Möbius, and S. Hutzler. A public study of the lifetime distribution of soap films. *American Journal of Physics*, 79:819, 2011.

[60] N.W. Ashcroft and N.D. Mermin. *Solid state physics*. Science: Physics. Saunders College, 1976.

[61] Paul J. Steinhardt, David R. Nelson, and Marco Ronchetti. Bond-orientational order in liquids and glasses. *Phys. Rev. B*, 28:784–805, Jul 1983.

[62] Wolfgang Lechner and Christoph Dellago. Accurate determination of crystal structures based on averaged local bond order parameters. *The Journal of Chemical Physics*, 129(11):114707, 2008.

[63] G. E. Schröder-Turk, W. Mickel, S. C. Kapfer, M. A. Klatt, F. M. Schaller, M. J. F. Hoffmann, N. Kleppmann, P. Armstrong, A. Inayat, D. Hug, M. Reichelsdorfer, W. Peukert, W. Schwieger, and K. Mecke. Minkowski tensor shape analysis of cellular, granular and porous structures. *Advanced Materials*, 23(22-23):2535–2553, 2011.

[64] C O'Donvan, E. Corwin, and M. Mobius. The structure of disordered packings. Unpublished.

[65] Haobin Wang and Jiushu Shao. Dynamics of a two-level system coupled to a bath of spins. *The Journal of Chemical Physics*, 137(22):22A504, 2012.

[66] S. Heitkam, W. Drenckhan, and J. Fröhlich. Packing spheres tightly: Influence of mechanical stability on close-packed sphere structures. *Phys. Rev. Lett.*, 108:148302, Apr 2012.

[67] A. Okabe, B. Boots, K. Sugihara, and D.S.N. Chiu. *Spatial Tessellations: Concepts and Applications of Voronoi Diagrams*. Wiley Series in Probability and Statistics. John Wiley & Sons, 2009.

[68] Maxime Clusel, Eric I. Corwin, Alexander O. N. Siemens, and Jasna Brujić. A 'granocentric' model for random packing of jammed emulsions. *Nature*, 460:611–615, 2009.

[69] C. H. Rycroft. Voro++: A three-dimensional voronoi cell library in c++. *Chaos*, 2009.

[70] Povray - the persistance of vision raytracer. `http://povray.org`.

[71] V. Lucarini. Three-dimensional random voronoi tessellations: From cubic crystal lattices to poisson point processes. *Journal of Statistical Physics*, 2009.

[72] A. J. Meagher, M. Mukherjee, D. Weaire, S. Hutzler, J. Banhart, and F. Garcia-Moreno. Analysis of the internal structure of monodisperse liquid foams by x-ray tomography. *Soft Matter*, 7:9881–9885, 2011.

[73] D. Weaire and S. Hutzler. *The physics of foams*. Clarendon press, Oxford, 1999.

[74] W. Thomson. On the division of space with minimum partitional area. *Philosophical Magazine*, 1887.

[75] A.M. Kraynik and D.A. Reinelt. Linear elastic behavior of dry soap foams. *J. Colloid Interface Sci.*, 181:511, 1996.

[76] E.B. Matzke. Volume-shape relationships in variant foams. a further study of the role of surface forces in three-dimensional cell shape determination. *Am. J. Botany*, 33:58, 1946.

[77] M. E. Rosa, M. A. Fortes, and M. F. Vaz. Deformation of three-dimensional monodisperse liquid foams. *European Physical Journal E*, 7(2):129–140, 2002.

[78] D. Weaire and R. Phelan. Optimal design of honeycombs. *Nature*, 367:123, 1994.

[79] Solidworkds. `http://www.solidworks.com/`.

[80] K. A. Brakke. The surface evolver. *Experimental Mathematics*, 1:141–165, 1992.

[81] D. Weaire R. Phelan and K. Brakke. On the division of space with minimum partitional area. *Exp. Math.*, 1995.

[82] Alfons van Blaaderen, Rene Ruel, and Pierre Wiltzius. Template-directed colloidal crystallization. *Nature*, 385:321–324, 1997.

[83] R. Gabbrielli. A new counter-example to Kelvin's conjecture on minimal surfaces. *Philos. Mag. Lett.*, 89:483., 2009.

[84] F.C. Frank and J.S. Kasper. *Acta Cryst.*, 11:184, 1958.

[85] F.C. Frank and J.S. Kasper. *Acta Cryst.*, 12:483, 1959.

[86] A. van der Net, A. Gryson, M. Ranft, F. Elias, C. Stubenrauch, and W. Drenckhan. Highly structured porous solids from liquid foam templates. *Colloids and Surfaces A: Physicochemical and Engineering Aspects*, 346(1-3):5–10, 2009.

[87] O. Carvente and J. C. Ruiz-Suarez. Crystallization of confined non-brownian spheres by vibrational annealing. *Physical Review Letters*, 95(1), 2005. 018001.

[88] R. Gabbrielli, A. J. Meagher, D Weaire, K. A. Brakke, and S Hutzler. An experimental realization of the Weaire–Phelan structure in monodisperse liquid foam. *Philosophical Magazine Letters*, 92(1):1–6, 2012.

[89] C. Zener. Contributions to the theory of beta-phase alloys. *Phys. Rev.*, 71:846–851, 1947.

[90] K. Momma. Vesta - visualisation for electronic and structural analysis. `http://jp-minerals.org/vesta/en/`, 2012.

[91] G. Rämme. *Soap Bubbles in Art and Education.* Science culture technology, 1998.

[92] R.J.D. Tilley. *Crystals and Crystal Structures.* John Wiley & Sons, 2006.

[93] Thomas C. Hales, John Harrison, Sean McLaughlin, Tobias Nipkow, Steven Obua, and Roland Zumkeller. A revision of the proof of the Kepler conjecture. *Discrete and Computational Geometry*, 44:1–34, 2010.

[94] Savka I. Stoeva, B. L. V. Prasad, Sitharaman Uma, Peter K. Stoimenov, Vladimir Zaikovski, Christopher M. Sorensen, and Kenneth J. Klabunde. Face-centered cubic and hexagonal closed-packed nanocrystal superlattices of gold nanoparticles prepared by different methods. *The Journal of Physical Chemistry B*, 107(30):7441–7448, 2003.

[95] Pawel Pieranski. Colloidal crystals. *Contemporary Physics*, 24(1):25–73, 1983.

[96] Galen T. Pickett, Mark Gross, and Hiroko Okuyama. Spontaneous chirality in simple systems. *Phys. Rev. Lett.*, 85:3652–3655, Oct 2000.

[97] A. Mughal, H. K. Chan, D. Weaire, and S. Hutzler. Dense packings of spheres in cylinders: Simulations. *Phys. Rev. E*, 85:051305, May 2012.

[98] A. Mughal, H. K. Chan, and D. Weaire. Phyllotactic description of hard sphere packing in cylindrical channels. *Phys. Rev. Lett.*, 106:115704, Mar 2011.

[99] A. Mughal, H. K. Chan, D. Weaire, and S. Hutzler. Dense packings of spheres in cylinders: Simulations. *Phys. Rev. E*, 85:051305, May 2012.

[100] M. Hodak and L.A. Girifalco. Systems of c60 molecules inside (10,10) and (15,15) nanotube: A monte carlo study. *Physical Review B - Condensed Matter and Materials Physics*, 68(8):854051–854057, 2003.

[101] Michael Tymczenko, Lluis F. Marsal, Trifon Trifonov, Isabelle Rodriguez, Fernando Ramiro-Manzano, Josep Pallares, Angel Rodriguez, Ramon Alcubilla, and Francisco Meseguer. Inside front cover: Colloidal crystal wires (adv. mater. 12/2008). *Advanced Materials*, 20(12), 2008.

[102] D. Weaire, S. Hutzler, and N. Pittet. Cylindrical packings of foam cells. *Forma*, 7(3):259–263, 1992.

[103] M. Saadatfar, J. Barry, D. Weaire, and S. Hutzler. Ordered cylindrical foam structures with internal bubbles. *Philosophical Magazine Letters,*, 88:661 – 668, 2008.

[104] S. T. Tobin, J. D. Barry, A. J. Meagher, B. Bulfin, C. E. O'Rathaille, and S. Hutzler. Ordered polyhedral foams in tubes with circular, triangular and square cross-section. *Colloids and Surfaces A: Physicochemical and Engineering Aspects*, 382(1-3):24–31, 2011. A collection of

papers from the 8th EUFOAM Conference and the Meetings of COST Actions D43 and P21.

[105] O. Carvente and J. C. Ruiz-Suárez. Crystallization of confined non-brownian spheres by vibrational annealing. *Phys. Rev. Lett.*, 95:018001, 2005.

[106] A. Mughal. Unpublished. 2012.

[107] A. Mughal, H. K. Chan, and D. Weaire. Phyllotactic description of hard sphere packing in cylindrical channels. *Phys. Rev. Lett.*, 106:115704, 2011.

[108] A.C. Fischer-Cripps. *Nanoindentation.* Mechanical Engineering Series. Springer, 2011.

[109] K. J. van Vliet and S. Suresh. Simulations of cyclic normal indentation of crystal surfaces using the bubble-raft model. *Philosophical Magazine A*, 82(10):1993–2001, 2002.

[110] E. Janiaud and F. Graner. Foam in a two-dimensional couette shear: a local measurement of bubble deformation. *Journal of Fluid Mechanics*, pages 243–267, 2005.

[111] R. Fitzgerald. Phase-sensitive x-ray imaging. *Physics Today*, 53(7):23–26, 2000.

[112] R. Höhler and S. Cohen-Addad. Rheology of liquid foam. *J. Phys.: Condens. Matter*, 17:1041–1069, 2005.

[113] D. B. Miracle. A structural model for metallic glasses. *Nat Mater*, 2004.

[114] G. Katgert, B. P. Tighe, M. E. Möbius, and M. van Hecke. Couette flow of two-dimensional foams. *EPL (Europhysics Letters)*, 90(5):54002, 2010.

[115] J.R. Seth, L. Mohan, C. Locatelli-Champagne, M. Cloitre, and R.T. Bonnecaze. A micromechanical model to predict the flow of soft particle glasses. *Nat Mater*, 10(11):838–43, 2011.

[116] A.F. Stalder, T. Melchior, M. Müller, D. Sage, T. Blu, and M. Unser. Low-bond axisymmetric drop shape analysis for surface tension and contact angle measurements of sessile drops. *Colloids and Surfaces A: Physicochemical and Engineering Aspects*, 364(1-3):72–81, 2010.